Photocatalysis
https://www.sciltp.com/journals/photocatalysis

Review

Two-Dimensional Layered Materials in Photoelectrocatalysis: A Review on Energy Conversion and Environmental Remediation

Penghui Xu [1,2,†], Hao Niu [2,†], Yuanping He [2], Yongfang Sun [1,2], Qiuhong Sun [2], Yang Li [1], Xiao-Jue Bai [1,2], Yung-Kang Peng [3], Tongjun Bao [4], Yanli Liang [5], Deqiang Feng [5], Ce Zhang [5,*] and Yufei Zhao [1,2,*]

[1] Quzhou Institute for Innovation in Resource Chemical Engineering, Quzhou 324000, China
[2] State Key Laboratory of Chemical Resource Engineering, Beijing University of Chemical Technology, Beijing 100029, China
[3] Department of Chemistry, City University of Hong Kong, Kowloon, Hong Kong SAR 999077, China
[4] Jiuyou Environmental Technology (Jiangsu) Co., Ltd., Yancheng 224400, China
[5] Qian Xuesen Laboratory of Space Technology, China Academy of Space Technology (CAST), Beijing 100094, China
* Correspondence: zhangce-qxslab@outlook.com (C.Z.); zhaoyufei@mail.buct.edu.cn (Y.Z.); Tel.: +86-010-64425385 (Y.Z.)
† These authors contributed equally to this work.

How To Cite: Xu, P.; Niu, H.; He, Y.; et al. Two-Dimensional Layered Materials in Photoelectrocatalysis: A Review on Energy Conversion and Environmental Remediation. *Photocatalysis* **2026**, *2*(1), 3. https://doi.org/10.53941/photocatalysis.2026.100003

Received: 29 January 2026
Revised: 27 February 2026
Accepted: 9 March 2026
Published: 31 March 2026

Abstract: Photoelectrochemical (PEC) technology serves as a pivotal pathway for converting solar energy into chemical fuels, demonstrating significant potential in addressing global energy crises and environmental challenges. Two-dimensional (2D) layered materials have garnered extensive attention in PEC research due to their unique structural characteristics, such as high specific surface area, efficient charge transport capabilities, and tunable electronic properties. This review systematically summarizes recent advances in the application of 2D materials in PEC systems, including metal oxyhalides, MXenes, graphitic carbon nitride (g-C_3N_4), and layered double hydroxides (LDHs), with a focus on their design, performance optimization, and implementation in energy conversion and environmental remediation. The article highlights key modification strategies for enhancing the PEC performance of 2D materials, such as photosensitizer decoration, elemental doping, and heterojunction engineering, which collectively contribute to improved light absorption, facilitated charge separation and transport, and accelerated surface reaction kinetics. Furthermore, diverse applications of 2D materials in PEC water splitting, CO_2 reduction, nitrogen reduction, organic pollutant degradation, and biosensing are summarized. Despite remarkable progress, the practical application of 2D materials in PEC systems still faces challenges related to conversion efficiency, operational stability, and cost-effectiveness. Future efforts should prioritize the development of novel robust materials, the integration of advanced in situ characterization and theoretical simulations to elucidate underlying mechanisms, and the fabrication of PEC devices resistant to electrochemical corrosion. Through interdisciplinary collaboration and technological innovation, 2D materials are poised to play a crucial role in advancing green energy conversion and sustainable chemical production.

Keywords: two-dimensional layered materials; photoelectrocatalysis; modification strategies; PEC electrolyzers and applications

1. Introduction

The rapid development of modern socioeconomics is built upon massive energy consumption. According to the *World Energy Outlook 2024* released by the International Energy Agency (IEA), fossil fuels still account for 80% of global primary energy consumption, with annual CO_2 emissions exceeding 36 billion tons. The overexploitation of fossil fuels has triggered severe resource depletion and environmental pollution. In this context, developing clean and sustainable energy technologies has become an urgent task for the global scientific and industrial communities [1–4]. China's dual-carbon goals also represent a proactive response to this global challenge, underscoring the strategic importance of low-carbon energy technologies. Solar energy conversion is especially promising due to abundant resources, wide distribution, and pollution-free nature. Natural photosynthesis—converting solar to chemical energy, forming the foundation of material and energy metabolism for nearly all life on Earth.

Photocatalysis utilizes semiconductor materials to generate electron-hole pairs for driving redox reactions, but often suffers from low quantum efficiency due to rapid charge carrier recombination, typically with EQE (External Quantum Efficiency) < 10%) [5]. PEC utilizes semiconductor materials to absorb light energy and generate electron-hole pairs. Under an electric field, the separation and migration of these photogenerated charge carriers are promoted, thereby driving redox reactions on the electrode surface. Its core principle lies in converting light energy into chemical or electrical energy, significantly enhancing reaction efficiency by regulating the synergistic effect between photoexcitation and electrochemical processes. As PEC integrates the advantages of both photocatalysis and electrocatalysis, which utilizes solar energy while applying an external bias to precisely modulate reaction barriers, thereby significantly enhancing carrier utilization efficiency, with hole injection efficiency exceeding 50% (Figure 1) [6–8]. Amidst growing energy and environmental challenges, catalytic technologies such as electrocatalysis and photoelectrocatalysis (PEC) are recognized as key solutions for the energy conversion. While electrocatalysis has shown broad utility, PEC offers distinct advantages, particularly in selectivity. By operating under milder conditions, PEC can selectively activate special bond (i.e., C=O, C-H, C-N bond), and oxidize reactants to a desired intermediate, minimizing over-oxidation. For instance, in glycerol oxidation to dihydroxyacetone (DHA), electrocatalysis often cleaves C-C bonds, yielding low-value C_1/C_2 products [9], whereas PEC maintains high activity with high DHA selectivity [10]. Similarly, electrocatalytic oxidation of HMF typically produces fully oxidized FDCA, while optimized PEC systems can selectively yield semi-oxidized products like 2,5-diformylfuran (DFF), 5-hydroxymethyl-2-furancarboxylic acid (HMFCA), or 5-formyl-2-furancarboxylic acid (FFCA) [11]. However, it is also well known that the large-scale application of photoelectrocatalytic (PEC) technology faces several critical bottlenecks. These include the limited light absorption range of semiconductors (e.g., TiO_2), which is often confined to UV light, and difficulties in achieving full-spectrum utilization. Rapid recombination and inefficient separation of photogenerated carriers also restrict quantum efficiency, while scaled-up systems suffer from charge loss over distance. A key trade-off exists between catalyst stability (resistance to photocorrosion) and high catalytic activity. Furthermore, reliance on precious metals or rare materials, combined with complex fabrication, hinders cost-effective production. Finally, insufficient understanding of interfacial reaction mechanisms limits the rational design of efficient, scalable systems, that needs to be solved efficiently.

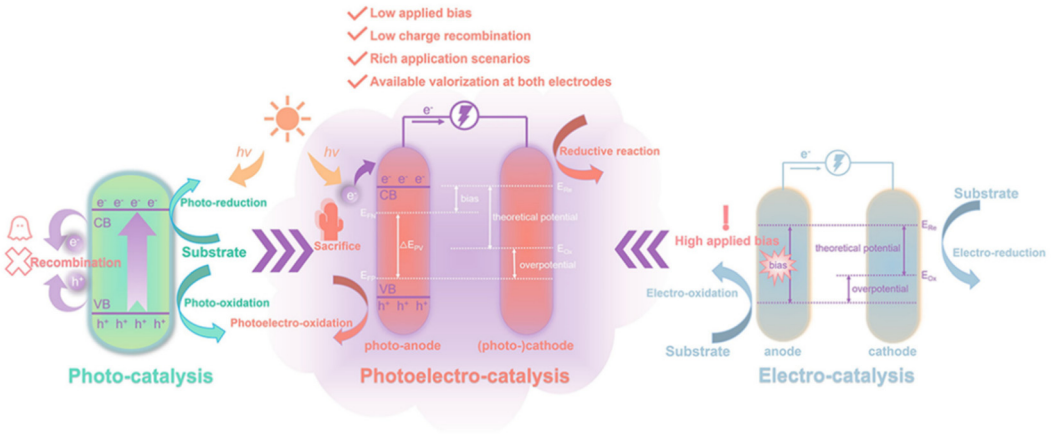

Figure 1. Comparison of photo-, electro-, and photoelectro-catalysis. E_{FP} and E_{FN} are the quasi Fermi levels of holes and electrons, respectively; E_{Ox} nd E_{Re} are the oxidative and reductive potentials of the substrate, respectively. Reprinted with permission from Ref. [12]. Copyright 2023, Royal Society of Chemistry.

In recent years, the application of multi-dimensional nanomaterials in (photo)electrocatalysis has been continuously expanding. While 1D nanomaterials materials possess fast channels for carrier separation, they are limited by their relatively small specific surface area. 3D nanomaterials materials suffer from tortuous and lengthy charge transport pathways with high electron-hole recombination probability; particularly, bulk materials feature long carrier migration distances within the interior, leading to significant losses before reaching the surface and substantial mass transfer resistance. By contrast, 2D layered materials exhibit excellent application prospects. Due to their ultra-thin 2D layered structure, they possess distinctive characteristics such as outstanding electronic conductivity, rapid carrier transport capability, large specific surface area, and high chemical stability—all of which are crucial for enhancing (photo)electrocatalytic performance. 2D layered materials are composed of layers stacked through weak interlayer interactions (i.e., van der Waals force) and can thus be readily exfoliated into atomic thickness 2D nanosheets via top-down approaches. Graphitic carbon nitride (g-C_3N_4), transition metal dichalcogenides (TMDs), certain transition metal (oxy)halides, transition metal carbides/nitrides (MXenes) materials, and layered double hydroxides (LDHs) all belong to this category [13–15]. Besides, other layered inorganic materials such as hexagonal boron nitride (hBN), SnS_2, MoS_2, GaS, WS_2, black phosphorus, and phosphorene have been reported to be readily exfoliated into nanosheet morphology. Among these, the transforming bulk WS_2 into a nanosheet structure promotes an indirect-to-direct bandgap transition and enhances light-harvesting efficiency, rendering it a highly effective photosensitizer [16]. In all, the term "2D photocatalyst" herein refers to 2D materials that exhibit photocatalytic activity or can be employed as cocatalysts in light-related reactions. In general, the roles of 2D materials in PEC can be categorized into three types: (I) as the primary catalyst, (II) as a catalytic transport medium, or (III) as a supporting matrix. Typically, 2D materials in PEC exhibit synergistic performance rather than a single monolithic function.

This review begins with an overview of the macro background of energy demands and environmental challenges, followed by a systematic summary of the current research status and applications of 2D layered materials in the field of (photo)electrocatalysis. We will introduce multiple 2D structures and their related configurations, including layered structures such as LDHs, layered halogen oxides, metal-containing/metal-free carbon/nitrogen-based structures. It will also cover composite structures derived from these 2D materials, such as support structures, charge transport media, and active coating layers—and explain common modification methods for materials with 2D morphologies. Finally, a systematic discussion will be conducted on their applications in water splitting, hydrogen peroxide production, carbon dioxide conversion, pollutant degradation, photodetector fabrication, and biomass molecule upgrading (Figure 2), along with an introduction and outlook on the design and applications of common PEC electrolyzers, aiming to provide insights and references for related research fields.

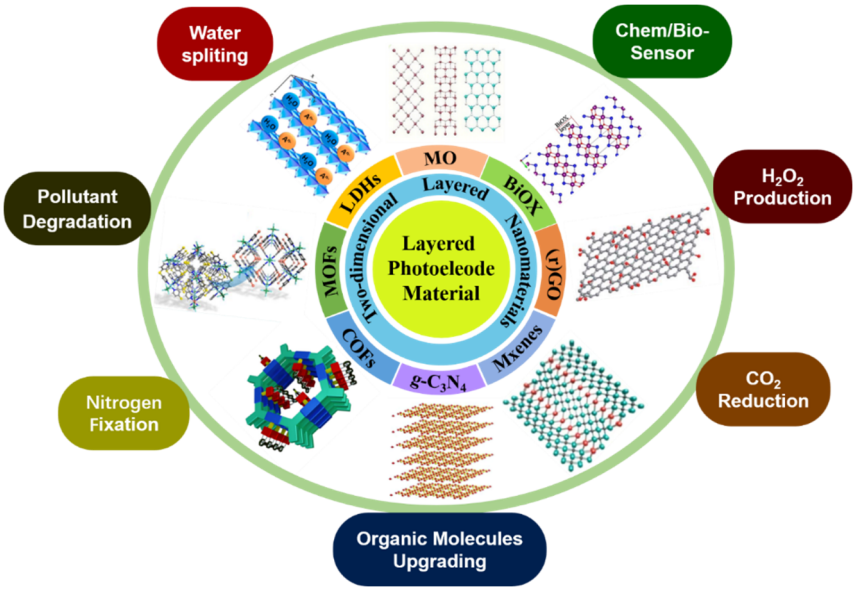

Figure 2. Models of different types of typical 2D layered nanomaterials in PEC reactions [16–23]. Reprinted with permission from Ref. [16]. Copyright 2018, Royal Society of Chemistry. Reprinted with permission from Ref. [17]. Copyright 2025, Elsevier. Reprinted with permission from Ref. [18]. Copyright 2025, Elsevier. Reprinted with permission from Ref. [19]. Copyright 2023, Elsevier. Reprinted with permission from Ref. [20]. Copyright 2022, Springer Nature. Reprinted with permission from Ref. [21]. Copyright 2016, Elsevier. Reprinted with permission from Ref. [22]. Copyright 2024, American Chemical Society. Reprinted with permission from Ref. [23]. Copyright 2023, American Chemical Society.

2. Modification Strategies for 2D Materials

Despite their unique atomic-level thickness, ultra-large specific surface area, and tunable electronic structure, 2D photocatalysts demonstrate significant potential in the field of PEC. However, limitations in their intrinsic performance still create a notable gap toward practical large-scale application. From the perspectives of photophysical and photochemical mechanisms, most 2D photoelectrodes face core challenges such as a narrow light absorption spectrum (e.g., wide-bandgap materials only respond to ultraviolet or partial visible light), rapid recombination of photogenerated electron-hole pairs, sluggish surface reaction kinetics, and insufficient catalytic stability. These drawbacks severely constrain their solar energy conversion efficiency and long-term operational capability. Meanwhile, the unsaturated coordination of surface atoms in 2D materials, while providing abundant active sites for catalytic reactions, also makes them prone to agglomeration, oxidation, or structural reconstruction in electrolytes, further degrading catalytic performance. Drawing on principles from surface science and coordination chemistry, strategies such as interface engineering and electronic state optimization developed in non-2D material systems have provided effective pathways to address the above issues. To overcome the performance bottlenecks of 2D photocatalysts, it is essential to develop precise modification strategies that systematically regulate their light-harvesting capability, electronic structure, charge transport pathways, and surface reaction activity. The goal is to achieve synergistic optimization across the entire reaction sequence of "light absorption-charge separation-surface catalysis." In this context, the following four common modification methods have been identified as key approaches to enhance the overall performance of 2D photoelectrocatalysts. Their design principles are centered on addressing the core challenges mentioned above, aiming to maximize the unique advantages of 2D materials in PEC reactions through precise structural control.

2.1. Photosensitizer Modification

Light harvesting is the primary step in PEC reactions. To extend the light absorption capability of wide-bandgap semiconductors, the most direct and effective strategy is to modify the photoanode surface with photosensitizers, including organic dyes, quantum dots (QDs), and noble metal nanoparticles. Different types of photosensitizers require different modification methods. Organic dyes are typically immobilized on the semiconductor surface via chemical adsorption or covalent bonding. These dye molecules can convert longer-wavelength solar light into molecular energy, subsequently allowing electron transfer to the substrate [24]; Quantum dots can be grown on the photoanode using methods such as chemical bath deposition (CBD), successive ionic layer adsorption and reaction (SILAR), or electrodeposition [25]; Noble metal nanoparticles are often loaded onto the surface via photoreduction, chemical reduction, impregnation or sputtering deposition [26]. These photosensitizers generally absorb light from the visible to the infrared spectrum. Upon photoexcitation, they generate charge carriers and inject the resulting charges into the photoelectrode to participate in subsequent transport and surface reactions. The sensitization mechanisms, advantages, limitations, and applications of these sensitizers are discussed and compared in detail through several representative examples summarized in Table 1.

Table 1. Comparison of the optical performance optimization of different photosensitizers on supporting materials.

	Sensitizers Categories	Support Material	Reaction System	Electrolyte Composition	Applied Potential	Carrier Utilization Efficiency	Ref.
Dye Sensitization	Y123 dye	TiO_2	PEC water splitting	1 M NaOH (PH = 13.6)	0.72 V_{RHE}	Charge collection efficiency: 99%	[27]
	RuP dye	TiO_2	Alkene epoxidation	0.1 M LiBr/CH_3CN/H_2O (v/v = 4/1)	0.6 V_{NHE}	Electron injection efficiency: 95%	[28]
	N719 dye	TiO_2	PEC sensing	0.1 M Na_2SO_4/organic polyiodide (I^-/I_3^-)	/	/	[29]
	P1 dye	NiO	PEC CO_2 reduction	0.2 M MES buffer (pH = 6.0)	−0.27 V_{SHE}	/	[30]
	BH4 dye	NiO	PEC water splitting	1 M HCl (pH = 0)	0 V_{NHE}	/	[31]
	N719 dye	SnO_2/TiO_2	PEC water splitting	Alkaline pH = 9	0 V	STH efficiency: 0.06%	[32]
QDs Sensitization	$Cd_{0.8}Zn_{0.2}S$ QDs	TiO_2	PEC organic pollutants degradation	NaCl	0.8 $V_{Ag/AgCl}$	/	[33]
	CdTe QDs	LDH@$BiVO_4$	PEC water splitting	0.1 M phosphate buffer (pH = 7)	/	Charge separation efficiency: 50%	[34]
	Zn-Cu-In-S-Se QDs	TiO_2	Fiber QDs-Sensitized solar cell	2.0 M Na_2S, 0.2 M KCl	−1.1 to −1.3 V_{SCE}	Charge collection efficiency: 97.41%	[35]
	CdS QDs	$BiVO_4$	PEC desalination	0.1 M $LiClO_4$/acetonitrile	1.0 mA	/	[36]
	Bi_2Se_3 or Bi_2Te_3 QDs	TiO_2	PEC dye degradation	0.1 M Na_2SO_4	1.0 V_{RHE}	/	[37]
	C QDs	Bi_2O_3	PEC water splitting	1 M Na_2SO_4	0 V_{RHE}	/	[38]
Precious Metal Sensitization	Au/Pt/Pd/Ir	$BiV_{1-x}O_y$	PEC Glycerol oxidation	0.5 M Na_2SO_4 (pH = 2)	1.23 V_{RHE}	/	[39]
	Ag_3PO_4 NPs	TiO_2	PEC removal of organic dyes and Cr(VI) ions	0.1 M Na_2SO_4	/	/	[40]
	Au	$Co(OH)_x/BiVO_4$	PEC water splitting	0.5 M borate buffer solution (pH = 9.5)	1.23 V_{RHE}	Charge separation efficiency: 95.4%	[41]
	Au NPs	Ta_3N_5	PEC water splitting	1 M KOH	1.0 V_{RHE}	Charge separation efficiency: 98%	[42]
	Cu/Au/Ag/Pd/Pt ED	Cu_2O	PEC water splitting	0.5 M Na_2SO_4	0 V_{RHE}	/	[43]
	CuPt NPs	COF	PEC ethane synthesis from CO_2	0.5 M $KHCO_3$	−0.25 V_{RHE}	/	[44]

2.1.1. Organic Dyes Sensitization

Organic sensitizers are widely used for the surface modification of semiconductors. When the excited-state potential of the organic dye molecule is more negative than the conduction band potential of the semiconductor, the dye molecule can inject photogenerated electrons into the semiconductor's conduction band. These electrons are subsequently transferred to acceptors adsorbed on the catalyst surface. Consequently, dye sensitization can effectively extend the visible-light response range of semiconductor photocatalysts. Dye-sensitized semiconductors find broad applications in various fields, including dye-sensitized solar cells (DSSCs) [45], photocatalytic water splitting for hydrogen production, and the photocatalytic degradation of organic pollutants [46–48]. In recent years, researchers have conducted extensive innovative studies on the application of organic sensitizers across various semiconductor systems. Through precise control of molecular design and interface engineering, a series of high-performance photoelectrocatalytic systems have been successfully developed. This progress provides important theoretical foundations and technical references for the practical application of organic sensitization strategies.

Lee et al. demonstrated the systematic integration of a fractal network design with a hemispherical photodetector array utilizing organic dye-sensitized graphene. This system exhibits advanced optoelectronic functionality capable of detecting both the direction and intensity of incident light, while maintaining structural robustness with a high threshold strain to prevent damage during integration on various hemispherical surfaces. Pyronin B (PyB)-incorporated graphene presents a viable alternative to silicon, serving as a flexible and efficient photoactive component with enhanced photoresponsivity (>1000 A W^{-1}, Figure 3a) [49]. The design separates the functions of light absorption and charge transport, overcoming the performance limitations of single-component materials, but the spectral selectivity advantage of dye sensitization is not fully realized. In another study, Zhu et al. constructed a $TiO_2/CdIn_2S_4$ (TCIS) heterojunction sensitized with Rhodamine B (RhB) for efficient hydrogen peroxide production (Figure 3b). The optimized TCIS system achieved a maximum H_2O_2 generation rate of 2848 μmol g^{-1} h^{-1} under visible light irradiation, with an apparent quantum yield of 4.63% at 420 nm monochromatic light [50]. The visible light absorption of RhB extends the catalyst's response range from the UV region into the visible region, significantly enhancing its light-harvesting capability. Similarly, Wang et al. developed an eosin-Y (EY)-sensitized g-C_3N_4/PtNi/GO photocatalytic system (Figure 3c) that demonstrated outstanding hydrogen evolution activity (HEA) of 5.89 mmol g^{-1} h^{-1}, which is 1.54 times higher than that of the g-C_3N_4/Pt/GO composite (3.82 mmol g^{-1} h^{-1}). Photoluminescence quenching spectra and transient photocurrent response studies revealed that the enhanced HEA of the g-C_3N_4/PtNi/GO composite is attributed to its improved charge separation efficiency, as an organic dye, Eosin Y possesses a visible-light absorption edge extending to ~550 nm, significantly broadening the response range of g-C_3N_4 (~450 nm) and theoretically enabling the capture of more solar photons [51]. Furthermore, a photocatalyst based on the g-C_3N_4/Pt composite modified with N-annulated perylene-based (PY) organic dye molecules has been reported to form a hybrid catalyst (g-C_3N_4/Pt/PY, Figure 3d). The presence of amide bonds between the amine groups in g-C_3N_4 and carboxyl groups of the dye molecules enables higher hydrogen evolution efficiency. This enhancement results from the covalent electron transfer channels formed at the dye/g-C_3N_4 interface and the increased migration and separation of photoinduced electrons mediated by g-C_3N_4, the amide bonds act as molecular-level "wires," providing a delocalized π-electron pathway that significantly enhances the transfer efficiency of excited-state electron injection from the dye into g-C_3N_4, as opposed to relying on random molecular collisions. However, the high apparent quantum yield (AQY) was achieved only under monochromatic light at 550 nm, while the overall efficiency under broad-spectrum (simulated sunlight) conditions has not been explicitly studied [52].

Organic dye molecules serve as efficient light-harvesting sensitizers, and they are firmly anchored to the substrate surface via π-π stacking or chemical bonding. The coverage density, orientation, and coupling strength of the dye molecules directly influence the energy/charge transfer efficiency. Achieving optimal, uniform, and stable monolayer coverage remains a finely tuned scientific challenge.

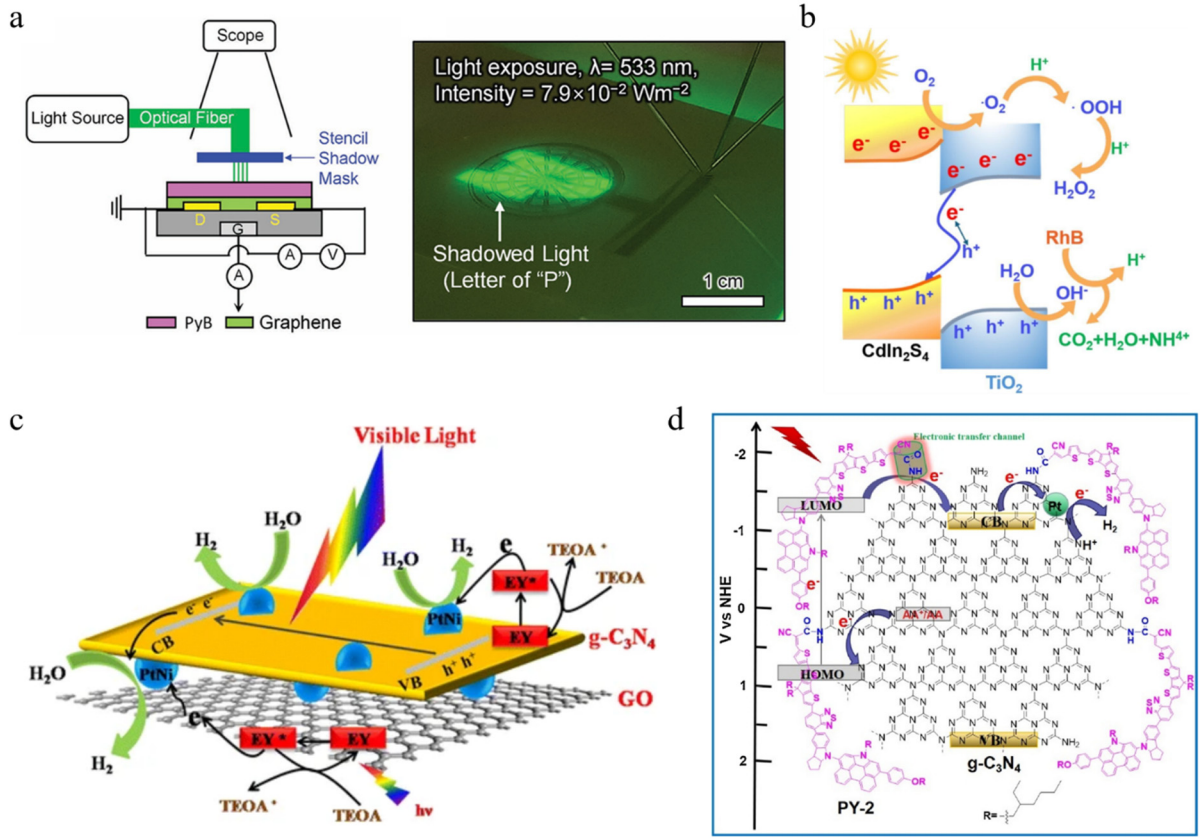

Figure 3. 2D semiconductor materials were sensitized with (**a**) PyB. Reprinted with permission from Ref. [49]. Copyright 2020, John Wiley and Sons. (**b**) RhB. Reprinted with permission from Ref. [50]. Copyright 2025, Elsevier. (**c**) EY [51]. (**d**) PY. Reprinted with permission from Ref. [52]. Copyright 2018, Elsevier.

2.1.2. Quantum Dots (QDs) Sensitization

Quantum dots (QDs) are a unique form of semiconductor nanocrystals whose diameter is less than or comparable to the exciton Bohr radius (EBR) of their corresponding bulk semiconductor. The quantum confinement effect dictates their optical and electronic properties. Several characteristics of QDs have positive impacts, which are specifically manifested as: (I) Size-tunable bandgap, enabling the alignment of the material's absorption spectrum with the solar spectrum for efficient solar energy harvesting [53]. This may also provide band edge alignment favorable for charge carrier transport. (II) Large extinction coefficients due to the quantum confinement effect, resulting in enhanced light absorption. (III) Substantial intrinsic dipole moments, which can lead to rapid separation of photogenerated charge carriers [54,55]. (IV) Increased charge carrier density owing to the multiple exciton generation effect [56]. Consequently, the sensitization of semiconductors with quantum dots facilitates the generation, separation, and transport of charge carriers throughout the process, thereby enhancing the overall PEC response.

QDs-sensitized photoelectrochemical cells enable efficient degradation of organic pollutants with advantages of no secondary pollution and energy savings. A study designed a ternary $TiO_2/Cd_{0.8}Zn_{0.2}S/ZnS$ heterojunction photoanode (Figure 4a,b), tuning the particle size of quantum dots (2–10 nm) through size engineering enables continuous adjustment of their absorption edge (400–600 nm), achieving broad-spectrum matching with solar radiation [33]. However, the absorption bandwidth of single-sized quantum dots is limited to 50–100 nm. Although multi-size blending can broaden this range, energy transfer competition between different sizes occurs, resulting in limited overall enhancement. Accordingly, Peng et al. designed a hybrid photoelectrode by integrating a TiO_2 nanoparticle film into aligned TiO_2 nanotube array on a titanium wire, and wrapping a carbon nanotube sheet coated with Cu_2S nanosheets around another titanium wire. The resulting fiber-shaped c quinary alloy QDs-sensitized solar cell (FQDSC) can receive incident light from all directions, which synergistically enhanced ambient diffuse light absorbing and charge collection efficiency of quantum dots through the design of a fibrous hybrid electrode, thereby achieving a record-breaking efficiency of 11.05% for the fiber-based quantum dot-sensitized solar cell (Figure 4c,d). However, at high loading densities, quantum dots may come into direct surface

contact, which can promote exciton energy transfer instead of charge separation, thereby reducing photon utilization efficiency [57].

Quantum dot sensitization can significantly broaden and enhance the light-harvesting range and charge generation efficiency of photoelectrocatalysts due to its size-tunable spectral absorption and efficient multiple exciton generation capability. However, its application is constrained by key challenges such as charge recombination induced by surface defects, insufficient long-term photochemical stability, and the need for interfacial energy level alignment with the host material, and also the green synthesis process and scale up ability. The future direction focuses on developing more robust surface passivation strategies and interface engineering to simultaneously improve both activity and durability. Given the trade-off dilemma between stability and efficiency in quantum dot sensitization, researchers have turned their attention to noble metal loading strategies, opening a new era for light absorption enhancement through plasmon resonance effects and chemical interface modulation.

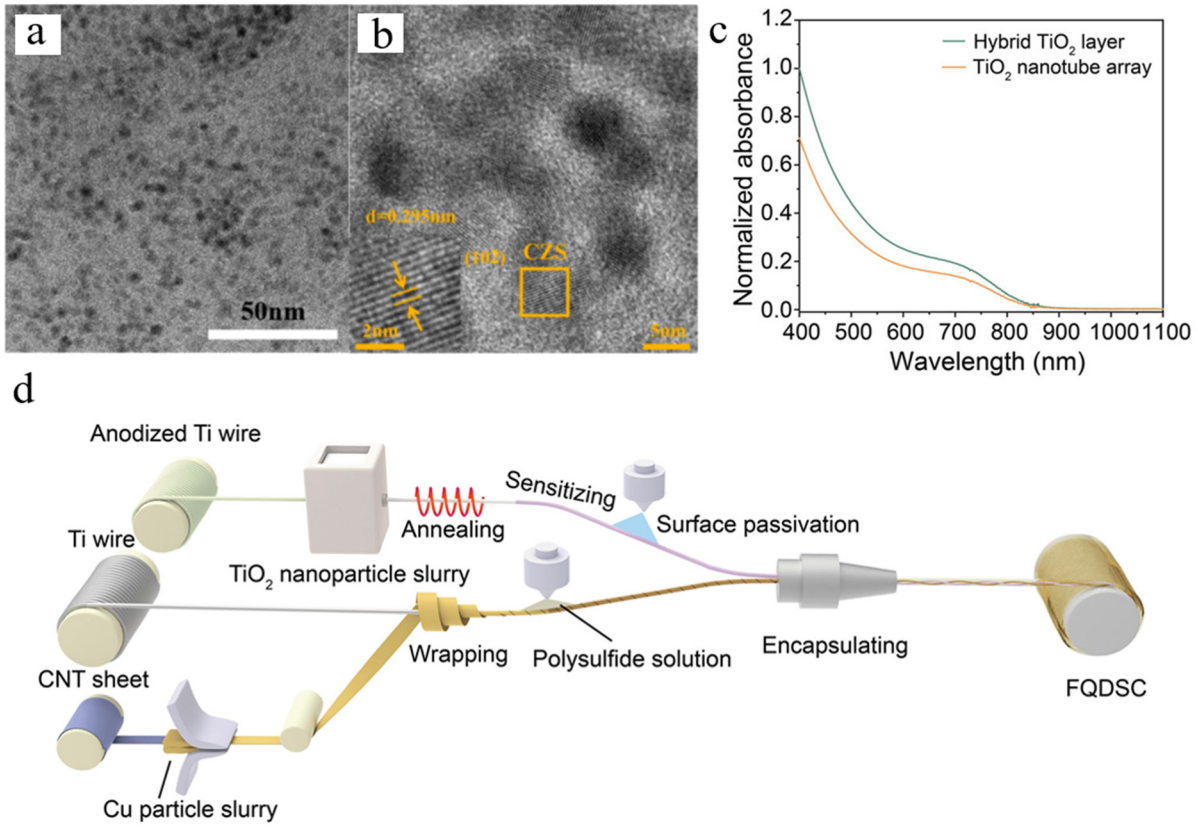

Figure 4. 2D semiconductor materials were sensitized with (**a**,**b**) ZnS. Reprinted with permission from Ref. [33]. Copyright 2025, Elsevier. (**c**,**d**) TiO_2 QDs. Reprinted with permission from Ref. [57]. Copyright 2025, John Wiley and Sons.

2.1.3. Noble Metal Nanoparticles Sensitization

Depositing noble metal nanoparticles on 2D materials to inject hot electrons into photoelectrodes via localized surface plasmon resonance (LSPR) is an effective strategy for enhancing PEC efficiency [26,43,58]. Current research has evolved from using single metals to designing multicomponent composite structures, demonstrating significant potential in energy conversion and environmental remediation. Chen et al. developed a NIR-PEC biosensor based on an alloyed h-BN/Au_5Pt_9 nano-frame for ultrasensitive glucose monitoring in human tears. The h-BN/Au_5Pt_9 nano-frame exhibit significantly enhanced electrocatalytic performance, attributed to the synergistic coupling of three key mechanisms: the intrinsic metal–metal synergistic effect, efficient charge transport facilitated by the nanoframe architecture, and the stabilizing and synergistic coupling effect of h-BN (Figure 5a). Interestingly, compared to visible light or other NIR wavelengths, excitation at 808 nm resulted in higher PEC accuracy and sensitivity for ultralow glucose monitoring from human tears (Figure 5b), which primarily attributed to the intrinsic catalytic properties of the AuPt alloy, which exhibits higher catalytic efficiency for glucose oxidation at specific potentials while showing weak responses to other coexisting substances, thereby enabling the selective detection of glucose. However, the van der Waals contact between h-BN and the AuPt framework may detach under mechanical deformation or liquid flow, leading to a reduction in optically active

sites and consequently affecting the durability of the monitoring system [59]. For multi-species detection and multiplexed applications, Maji et al. reported the design of a nanocomposite based on AuNBP@MoS_2, which integrates surface plasmon resonance-driven hot electron generation with the charge transport properties of a 2D semiconductor for high-performance PEC applications (Figure 5c). The injection of hot electrons generated by AuNBP into the conduction band of MoS_2 not only enhances the interfacial charge separation efficiency and amplifies the photocurrent signal, but also optimizes the catalytic selectivity of the electrode surface toward the target molecule. This is because the injection of hot carriers can modulate the reaction pathway, making it more favorable for the oxidation reaction of the target molecule. The fabricated sensor device not only exhibits ultra-sensitive detection capabilities for hydrogen peroxide and glucose from Human serum (Figure 5d) but can also detect specific HeLa cancer cells through biomarker-triggered hydrogen peroxide release. Furthermore, in HER researches, this composite electrode demonstrated outstanding performance. These enhancements originate from synergistic hot electron injection, photothermal activation, and MoS_2-mediated catalytic effects. A direct comparison of analytical methods reveals that conventional techniques are far more tedious and time-intensive relative to PEC sensors, which function within seconds-minutes. As reported by Zeng et al., RP-HPLC-based glucose analysis necessitates a 30–40 min retention time, excluding the laborious mobile phase preparation, and achieves a detection limit of only 3390 nM [60], markedly less sensitive than PEC sensors~0.17 nM [61].

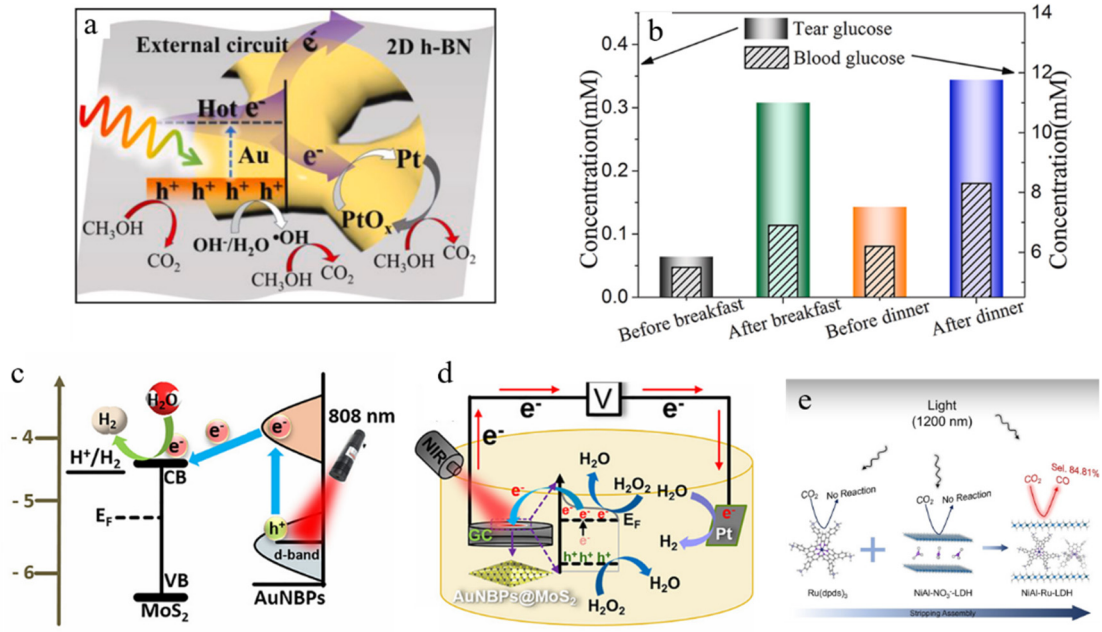

Figure 5. Sensitization of 2D semiconductor materials was performed using noble metal elements such as (**a**,**b**) Au_5Pt_9. Reprinted with permission from Ref. [59]. Copyright 2021, Elsevier. (**c**,**d**) AuNBP. Reprinted with permission from Ref. [62]. Copyright 2016, Royal Society of Chemistry. (**e**) $[Ru(dpds)_3]^{4-}$. Reprinted with permission from Ref. [63]. Copyright 2024, John Wiley and Sons.

However, the enhancement of light capture primarily relies on the near-field enhancement from noble metal LSPR rather than the optimization of intrinsic material absorption [62]. To address this issue, our group achieved a record-low optical bandgap of 0.89 eV by intercalating the anionic Ru complex $[Ru(dpds)_3]^{4-}$ into the interlayers of NiAl-LDH. This process induced secondary charge rearrangement within the LDH lattice, increasing the electronic density of states near the Fermi level and shifting the band edge levels. Consequently, the LDH material gained the unprecedented ability to absorb NIR-II photons at 1200 nm (Figure 5e), give the CO and H_2 evolution from CO_2 photoreduction. This represents one of the longest response wavelengths reported in the field of photocatalysis, effectively breaking the conventional semiconductor bandgap limitation [63].

Noble metal sensitization significantly enhances light absorption and carrier separation efficiency through the surface plasmon resonance effect and co-catalytic functions. However, it faces bottlenecks such as high cost, poor durability, and low recovery rates. Moving forward, it is necessary to develop low-cost alternative materials such as copper-based compounds, utilize machine learning for optimized design, and conduct in-depth research on the synergistic effects between photothermal processes and catalytic mechanisms. Additionally, challenges related to long-term stability and the economic feasibility of large-scale applications must be addressed.

2.2. Elemental Doping

Elemental doping is a versatile strategy for modulating semiconductor properties. Introducing heteroatoms into the semiconductor lattice can alter its energy band structure and regulate the electronic structure and charge carrier behavior of photoelectrodes, thereby systematically optimizing the light absorption, charge separation, and surface reactions of 2D materials [64]. Herein, the advantages, limitations, and applications of these doping strategies are discussed and compared in detail through several representative examples summarized in Table 2. Seo et al. reported Zr-doped 2D porous $SrNbO_2N$ nanosheets. During the flux-assisted calcination process using potassium chloride, zirconium ions were incorporated into $Sr_5Nb_4O_{15}$. Subsequent nitridation and spin-coating steps completely transformed the $Sr_5Nb_4O_{15}$:Zr into 2D single-crystal $SrNbO_2N$:Zr plate photoanodes with a large surface area. Electrochemical analysis revealed that the 2D structure of $SrNbO_2N$:Zr enhances charge separation and accelerates charge transfer during water splitting, thereby promoting the reaction (Figure 6a). However, the synergistic mechanism between Zr doping and the 2D structure still requires more in-depth theoretical and experimental analysis. To verify the mechanistic explanation for the activity enhancement induced by doping. Leveraging the excellent photoelectric properties of CdS, a novel 2D cadmium organic framework (Cd-MOF) was obtained via a solvothermal method as a precursor template, C and N co-doped CdS-T, CdS-800 demonstrated excellent photocatalytic degradation efficiency for five organic dyes. Free radical trapping experiments indicated that $\cdot O^{2-}$ plays a dominant role in the photocatalytic process (Figure 6b). Furthermore, combined experimental and DFT calculations revealed that C doping substituting S sites forms shallow donor levels, while N doping substituting Cd sites forms shallow acceptor levels. The synergistic effect of these dopants optimizes the bandgap to 2.25 eV (compared to 2.42 eV for pure CdS), resulting in a red-shift of the absorption edge to approximately 550 nm. However, CdS itself is prone to photoinduced hole oxidation ($S^{2-} \rightarrow S^0$), whether C/N doping exacerbates this process has not been investigated [63]. Furthermore, Kim et al. presents an innovative method for the room-temperature electroless electrochemical deposition of $(Fe_{1-x}Mn_x)OOH$ nanosheets and systematically elucidates the mechanism by which Mn incorporation enhances catalytic activity. The incorporation of Mn not only modifies the morphology and electronic structure of the nanosheets but, more critically, optimizes the material's adsorption kinetics for oxygen evolution reaction intermediates, thereby significantly reducing the reaction overpotential and boosting its intrinsic activity. This doping strategy also endowed the material with excellent stability, allowing it to operate continuously for 40 h under harsh oxygen evolution conditions, which fully demonstrates its potential for practical applications (Figure 6c) [65].

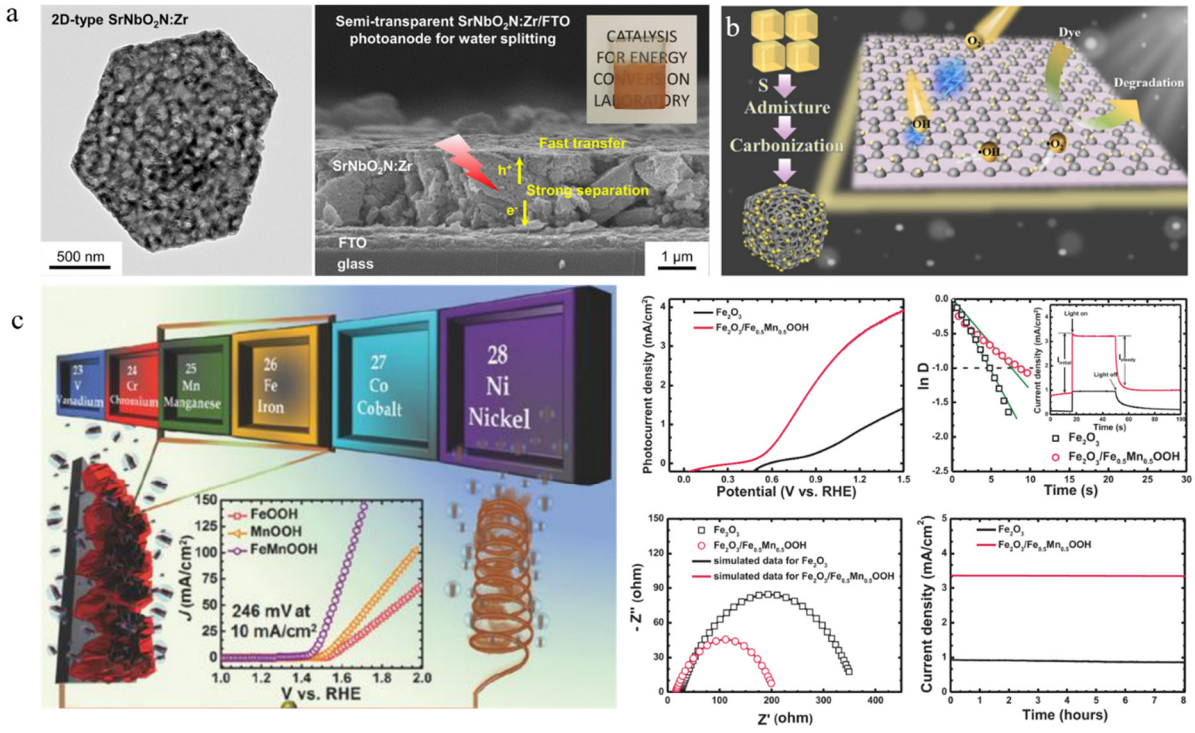

Figure 6. 2D semiconductor materials were doped with elements such as (**a**) Zr, reprinted with permission from Ref. [66]. Copyright 2023, Elsevier. (**b**) C/N, reprinted with permission from Ref. [67]. Copyright 2024, Elsevier. (**c**) Mn, reprinted with permission from Ref. [65]. Copyright 2018, John Wiley and Sons.

Table 2. Comparison of performance optimization of semiconductor materials by different element doping.

	Dopants	Support Material	Reaction System	Electrolyte Composition	Applied Potential	Carrier Utilization Efficiency	Ref.
Elemental Doping	Zr doping	$SrNbO_2N$	PEC water splitting	0.5 M K_3BO_3 (KBi, pH 13)	1.23 V_{RHE}	Charge separation efficiency:72%	[66]
	Mn doping	FeOOH	PEC water splitting	0.1 M Na_2SO_4 (pH = 6.8)	1.23 V_{RHE}	photoconversion efficiency: 0.82%	[65]
	In doping	GaN	PEC CO_2 reduction	0.5 M $KHCO_3$ (pH = 7.5)	−0.75 V_{RHE}	/	[68]
	N, P co-doping	TiO_2	PEC activation of sulfate	0.2 M Na_2SO_4 + 5 mg/L SMX	2.0 V_{RHE}	photoconversion efficiency: 0.86%	[69]
	Ti,Ge co-doping	Fe_2O_3	PEC water splitting	1 M KOH	1.043–1.093 V_{RHE}	ABPE: 0.162%	[70]
	Co doping	GaN	PEC water splitting	0.5 M H_2SO_4 (pH = 0)	1.23 V_{RHE}	Charge transfer efficiency: 80.73%	[71]

Doping effectively modulates the semiconductor band structure by introducing impurity energy levels, which broadens the light response range, promotes charge separation, and induces the formation of new active sites. However, its core limitation lies in the significant challenge of precisely controlling doping elements, concentrations, and locations (such as surface or subsurface), which directly affects the stable enhancement of performance and the clear elucidation of underlying mechanisms.

2.3. Heterojunction Engineering

The construction of heterojunctions is an effective approach for promoting charge carrier separation by advantage different type of materials. By rationally combining semiconductors with different band structures, the built-in electric field generated by the energy level difference drives the directional migration of photogenerated electrons and holes. This enables the spatial separation of electron-hole pairs, suppresses charge carrier recombination, and improves the utilization efficiency of photogenerated carriers [71–73]. Based on their composition, heterojunctions are primarily categorized into Schottky junctions, formed between metals and semiconductors, and semiconductor-semiconductor heterojunctions. Among the latter (Figure 7a–c), Type-II heterojunctions are the most representative due to their staggered band alignment. During the investigation of heterojunction materials, it was discovered that Type-II heterojunctions exhibit different charge transfer pathways in photocatalytic reactions. Consequently, based on this observation, Type-II heterojunctions are further classified into O-scheme, Z-scheme, and S-scheme heterojunctions, the most significant manifestation of heterojunction engineering is the enhancement of charge carrier separation efficiency, which can be improved by 30% to over 20 times [72,74,75].

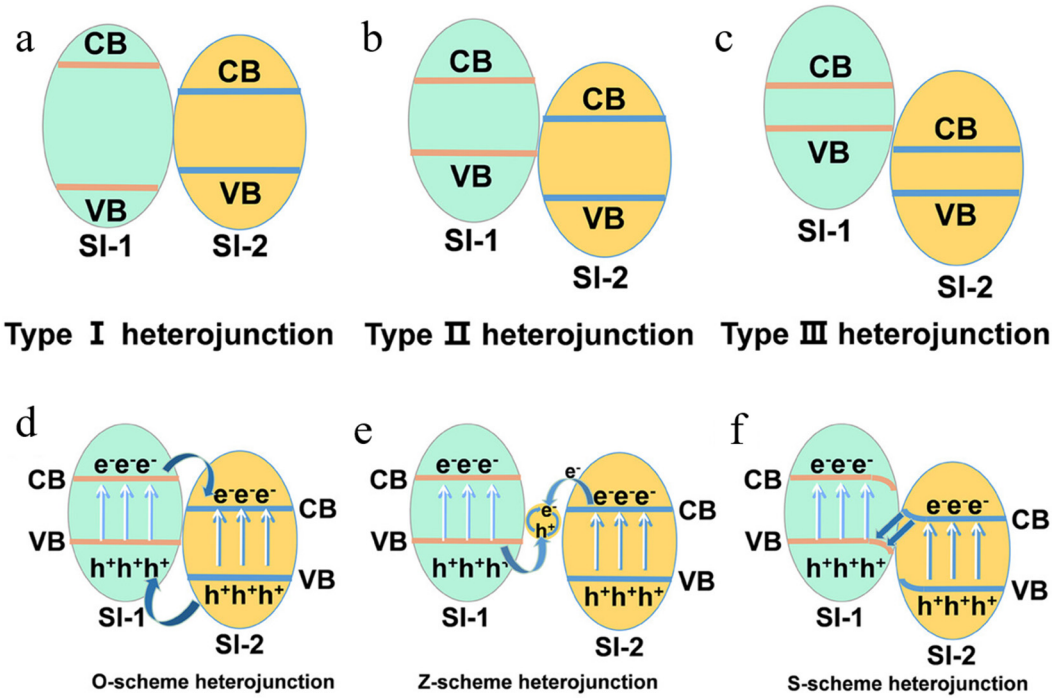

Figure 7. The band alignment configurations vary across different types of heterojunctions [76]: (**a**) Type-I, (**b**) Type-II, (**c**) Type-III heterojunction and (**d**) O-type, (**e**) Z-scheme, (**f**) S-scheme heterojunction.

The charge transfer in three Type-II heterojunction types is summarized as follows. O-scheme (Figure 7d): Photogenerated electrons transfer from the CB of SI-1 to the CB of SI-2, while holes migrate from the VB of SI-2 to the VB of SI-1. This spatial separation enhances carrier separation efficiency but results in accumulated carriers with lower redox potentials than the individual components. Z-scheme (Figure 7e): Electrons in the CB of SI-2 recombine with holes from the VB of SI-1 via a mediator (e.g., metal or redox couple). This preserves the strongest reducers (CB of SI-1) and oxidizers (VB of SI-2), enhancing overall redox capability, though often requiring higher-energy photons. S-scheme (Figure 7f): Similar to the Z-scheme but without a mediator. An internal electric field drives direct interfacial recombination of weaker carriers, retaining the most powerful electrons and holes in separate components, thereby improving both redox ability and separation efficiency. Yu et al. provided the first spatial verification of the S-scheme "back-to-back" band alignment using Kelvin probe force microscopy, showing electron accumulation on CdS and hole accumulation on BiOBr [77]. The composition, advantages, limitations, and applications of different heterojunctions are compared in Table 3.

Conventional industrial ammonia synthesis typically employs the Haber-Bosch process, which requires harsh high-temperature and high-pressure conditions and is highly energy-intensive [78]. In this context, the PEC method is considered a promising alternative for the nitrogen reduction reaction (NRR), but it suffers from low efficiency and yield [79]. Therefore, exploring active catalysts remains essential. In this work, a $BiVO_4$@MXene composite was facilely synthesized via a hydrothermal method. The in-situ grown heterojunction on 2D MXene significantly enhanced NRR efficiency: under PEC conditions, the optimized NH_3 production rate reached 27.25 μg h^{-1} cm^{-2} with a Faradaic efficiency of 17.54% at −0.8 V_{RHE}, outperforming most state-of-the-art NRR (photo)electrocatalysts. Mechanistic studies revealed that the expanded light absorption range and heterojunction formation greatly promoted the separation and transfer efficiency of photogenerated charge carriers (Figure 8a), thereby enhancing the PEC catalytic capability [48]. Yan et al. ingeniously optimized the carrier separation efficiency in the signal-off PEC sensor by constructing a 2D Z-scheme $ZnIn_2S_4$/g-C_3N_4 heterojunction. The intimate "face-to-face" contact interface formed between the 2D nanosheets provides abundant charge transfer channels, greatly facilitating the rapid migration of photogenerated electron-hole pairs. Based on this efficient carrier separation strategy, the fabricated immunosensor demonstrates exceptional sensitivity for the detection of carcinoembryonic antigen (CEA), the core recognition mechanism relies on the specific immunoaffinity reaction between the capture antibody (Ab_1) and CEA. the 2D $ZnIn_2S_4$/g-C_3N_4 structure provides abundant active sites for immobilizing the capture antibody Ab_1. When Ab_1 binds to CEA, it subsequently forms a sandwich structure with the signal antibody (Ab_2) labeled with $BiVO_4$. This antibody-antigen interaction exhibits extremely high specificity, analogous to a "lock-key" model", with a detection limit as low as 0.03 pg mL^{-1}. This fully validates the effectiveness of the heterojunction engineering in enhancing photoelectrochemical conversion performance (Figure 8b) [80]. However, the performance of such heterojunctions largely depends on random, macroscopic interfacial contacts between the two materials. To achieve precise control over the electronic structure and charge behavior at the heterojunction interface, Chen et al. utilized atomic layer deposition to precisely engineer the interface, constructing 2D $PtSe_2$/p-Si heterojunction photocathode with highly optimized band alignment. The emerging S-scheme heterojunction theory in recent years has provided a new design paradigm for the efficient spatial separation of charges. By constructing a 1D/2D $Sb_2(S,Se)_3/In_2S_3$ S-scheme heterojunction photoanode, utilized its unique "stepwise" charge transfer mechanism, achieving a current density of 6.05 mA cm^{-2} at 1.23 V_{RHE}. This approach not only achieves highly efficient carrier separation but also maximally retains strong redox capabilities, thereby significantly enhancing the efficiency of photoelectrochemical water splitting. This reflects an expansion of the research approach from microscopic interface engineering to macroscopic band structure engineering (Figure 8c,d) [81,82]. Meanwhile, a heterojunction photoanode composed of 2D MoS_2 nanosheet-decorated 1D TiO_2 nanorods/0D CdS nanocrystals (TiO_2/CdS/MoS_2) was prepared via an all-solution process for PEC water splitting. This heterojunction photoanode exhibited a high photocurrent density of 3.25 mA cm^{-2} at 0.9 V_{RHE}. The study demonstrated that MoS_2 nanosheets extract holes from CdS and promote further charge separation in TiO_2/CdS (Figure 8e) [83]. Time-resolved photoluminescence measurements indicated an increased photoluminescence lifetime in TiO_2/CdS/MoS_2 due to the presence of MoS_2 nanosheets, thereby enhancing the PEC activity.

Heterojunction engineering, by constructing built-in electric fields and space-charge regions, has become a core strategy in photoelectrocatalysis for enhancing carrier separation and suppressing recombination. However, it still faces bottlenecks such as interface defect passivation, precise energy-level matching, and long-term photochemical stability. To address these issues, future efforts should focus on developing multi-junction coupling and dynamic adaptive interfaces to achieve breakthroughs in quantum efficiency under full-spectrum response.

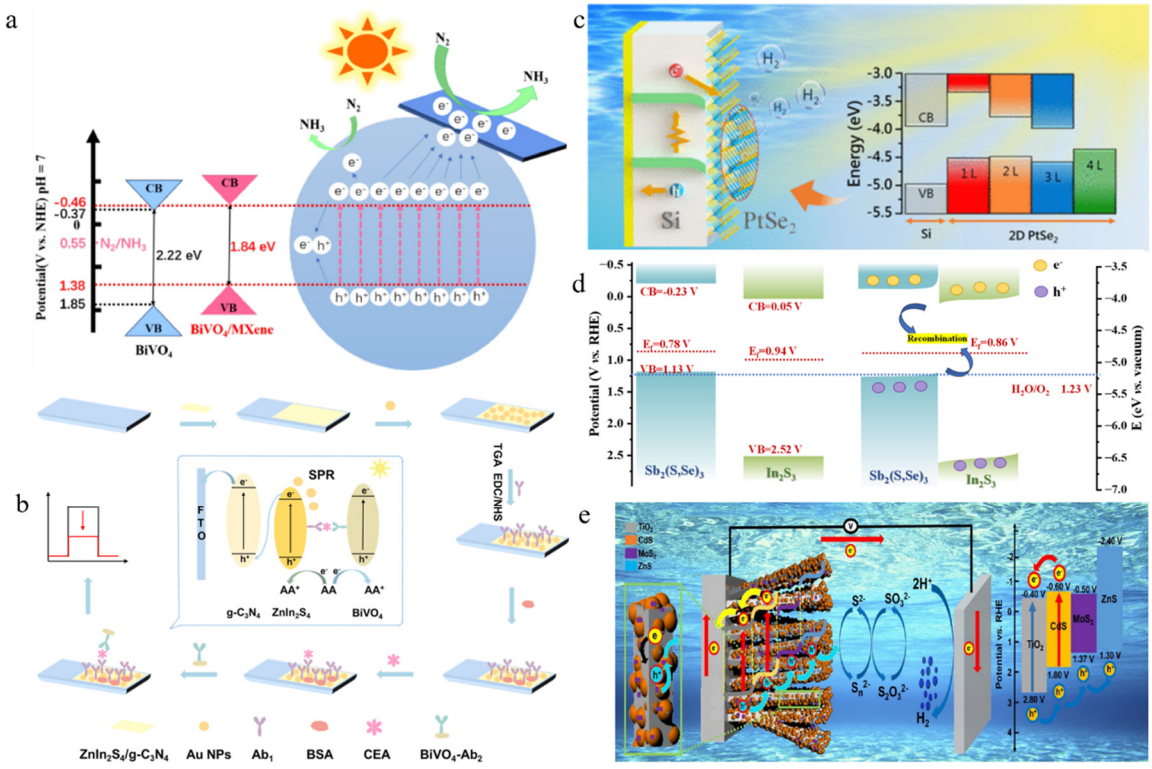

Figure 8. Fabrication and Applications of 2D (**a**) $BiVO_4$@MXene Heterojunction, reprinted with permission from Ref. [48]. Copyright 2022, Elsevier. (**b**) ZIS/CN Heterojunction, reprinted with permission from Ref. [80]. Copyright 2024, Elsevier. (**c**) $PtSe_2$/Si Heterojunction, reprinted with permission from Ref. [82]. Copyright 2021, American Chemical Society. (**d**) $Sb_2(S,Se)_3/In_2S_3$ Heterojunction, reprinted with permission from Ref. [81]. Copyright 2025, American Chemical Society. (**e**) TiO_2/CdS Heterojunction, reprinted with permission from Ref. [83]. Copyright 2019, Elsevier.

Table 3. Comparison of the enhancement of carrier utilization efficiency by heterojunction engineering.

	Heterojunction Composition	Reaction System	Electrolyte Composition	Applied Potential	Carrier Utilization Efficiency	Ref.
Heterojunction Engineering	$BiVO_4$/MXene Schottky junction	PEC N_2 reduction reaction	0.1 M K_2SO_4	−0.8 V_{RHE}	/	[48]
	$ZnIn_2S_4$/g-C_3N_4 Z-heterojunction	PEC immunosensing system	0.1 M PBS (pH = 7.4)	0.2 V_{RHE}	/	[80]
	$PtSe_2$/p-Si heterojunction	PEC water splitting	1 M $HClO_4$ (pH = 0)	0.29 V_{RHE}	/	[82]
	NR-$Sb_2(S,Se)_3/In_2S_3$ heterojunction	PEC water splitting	0.5 M Na_2SO_4	1.23 V_{RHE}	Charge injection efficiency: 70.45%	[81]
	TiO_2/CdS/MoS_2 heterojunction	PEC water splitting	0.35 M Na_2SO_3 + 0.25 M Na_2S (pH = 12)	0.9 V_{RHE}	IPCE: 45%	[83]
	Cu NPs/f-RGO/CF heterojunction	PEC CO_2 reduction	0.1 M $NaHCO_3$	2 V_{RHE}	/	[84]

2.4. Defect Engineering

Defect engineering, which involves the intentional application of defect-induced changes to optimize catalytic reaction processes, has been widely recognized as an effective strategy for enhancing PEC efficiency. The core principle of defect engineering in PEC lies in introducing specific defects to regulate the material's electronic structure and band alignment, thereby promoting the separation of photogenerated carriers and suppressing their recombination, while simultaneously constructing highly active sites. This approach can significantly broaden the light absorption range, improve charge transfer efficiency, and enhance the catalytic activity and selectivity for reactions such as water splitting and CO_2 reduction [85]. In practice, the design requires precise matching of defect types with target reactions. Defect concentration and variety are typically controlled through methods such as chemical reduction and plasma etching, with their optimization synergistically guided by theoretical calculations to align defects with desired photoelectrochemical performance. Table 4 summarizes representative application cases of defect engineering strategies, with detailed elaboration on common defect types, their limitations and advantages.

In the research on catalyst design and performance optimization, defect engineering has become a core regulatory strategy that significantly enhances the intrinsic catalytic activity of materials. At present, the main types of vacancy defects and their mechanisms have been systematically revealed. Based on differences in charge characteristics, vacancy defects can be classified into anion vacancies, cation vacancies, and mixed vacancies. In ionic crystals or compound semiconductors, negatively charged anions (such as O^{2-} [86], S^{2-} [87], Se^{2-} [88]) or positively charged cations (such as Co^{2+} [89], W^{x+} [90], Mo^{x+} [91]) depart from their original lattice sites, leading to the formation of positively or negatively charged vacancy defects at those positions. To maintain the electrical neutrality of the crystal, compensation mechanisms such as electron localization and changes in the valence states of anions and cations typically accompany this process, introducing shallow donor levels or forming acceptor levels. These defects can serve as active sites and regulate the material's band structure. Such vacancy structures demonstrate various potential applications in electrocatalysis, including HER, OER, and CO_2RR. They achieve this by reconstructing the atomic arrangement on the catalyst surface, modulating the electronic band structure, inducing the generation of active sites, and optimizing the adsorption behavior of intermediates.

Table 4. Comparison of the enhancement of carrier utilization efficiency in semiconductor materials by different defects.

	Defect Categories	Support Material	Reaction System	Electrolyte Composition	Applied Potential	Carrier Utilization Efficiency	Ref.
Defect Engineering	S vacancy	MoS_2	PEC water splitting	0.5 M H_2SO_4	−0.3 V_{RHE}	/	[92]
	C vacancy	g-C_3N_4	PEC cathodic protection	0.1 M Na_2S + 0.2 M NaOH	0 V_{RHE}	/	[93]
	Re vacancy	ReS_2	PEC water splitting	0.5 M H_2SO_4	0 V_{RHE}	/	[94]
	O vacancy	BiOCl	PEC water splitting	0.1 M Na_2S + Na_2SO_3 (1:1)	0.1 $V_{Ag/AgCl}$	/	[95]
	Bi vacancy	$BiVO_4/FeNiO_x$	PEC water splitting	0.2 M of Na_2SO_3 (pH = 9.5)	1.23 V_{RHE}	Charge separation efficiency = 100%	[96]
	O vacancy	Co_3O_4/TiO_2	Degradation of BPA and Cr(VI)	0.1 M Na_2SO_4	0.4 V_{SCE}	Charge separation efficiency = 26.23%	[97]

In the fields of photoelectrocatalysis, efficient separation of photogenerated carriers and material self-healing are crucial yet challenging. Many materials undergo degradation or failure during long-term reactions, leading to a decline in catalytic efficiency. To overcome this issue, the design of self-healing materials has emerged. Such materials can repair defects on their surfaces or within their structures under external conditions, thereby restoring their catalytic activity. Yang et al. proposed a strategy combining the quantum confinement effect and defect engineering to enhance the performance of Co/Bi composites in photocatalysis. Through this "kill two birds with one stone" approach, both the separation efficiency of photogenerated carriers and the material's self-healing capability were improved, effectively enhancing its long-term catalytic performance [98]. To further enhance proton transport capability, Ling et al. successfully developed a novel photocatalyst PEI/In_2S_3-Sv via a synergistic strategy of defect engineering and interfacial microenvironment modulation. This achieved efficient, sacrificial-agent-free H_2O_2 production in a visible-light pure water system, with a yield approximately 33.4 times higher than that of pristine In_2S_3 (Figure 9a,b). This successfully addressed two critical bottlenecks: insufficient oxygen activation efficiency and sluggish protonation kinetics [99]. Regarding PEC water activation and splitting, photogenerated holes in the valence band are strongly bound by atomic nuclei, resulting in intrinsic mobility much lower than that of electrons. This hole-electron mobility mismatch leads to rapid recombination of photogenerated carriers, severely limiting hydrogen production performance from water splitting. In light of this, Liu et al. proposed a "metal vacancy-regulated hole mobility" strategy to reshape carrier transport kinetics at the atomic scale via defects. By introducing metal vacancies to modulate the curvature of the valence band maximum, the effective mass of holes was reduced, thereby enhancing hole mobility (Figure 9c,d). After introducing V_M in WO_3, TiO_2, and Bi_2O_3, hole mobility increased by 430%, 350%, and 270%, respectively. Notably, Vw-WO_3 achieved a photocurrent density of 4.8 mA cm^{-2} (1.23 V_{RHE}) and maintained stability for 120 h. This strategy holds promise for providing a universal solution for the design of efficient photoelectrochemical energy conversion devices [85].

Defect engineering strategies involve the precise modulation of the electronic structure and surface properties of photoelectrocatalysts by introducing vacancies, dislocations, and other defects, significantly influencing crystal growth and the formation of active sites during the preparation process. However, its limitations lie in the difficulty of precisely controlling the type and concentration of defects. Excessive defects can easily become charge recombination centers, and some highly active defects are prone to corrosion during reactions, leading to a decline in catalyst stability. Future development will focus on the precise construction of atomic-scale defects, integrating in-

situ characterization techniques and machine learning to achieve refined defect control, developing defect-doping synergistic strategies, and simultaneously overcoming the bottlenecks in large-scale preparation technology, thereby promoting its industrial applications in areas such as solar hydrogen production and CO_2 reduction.

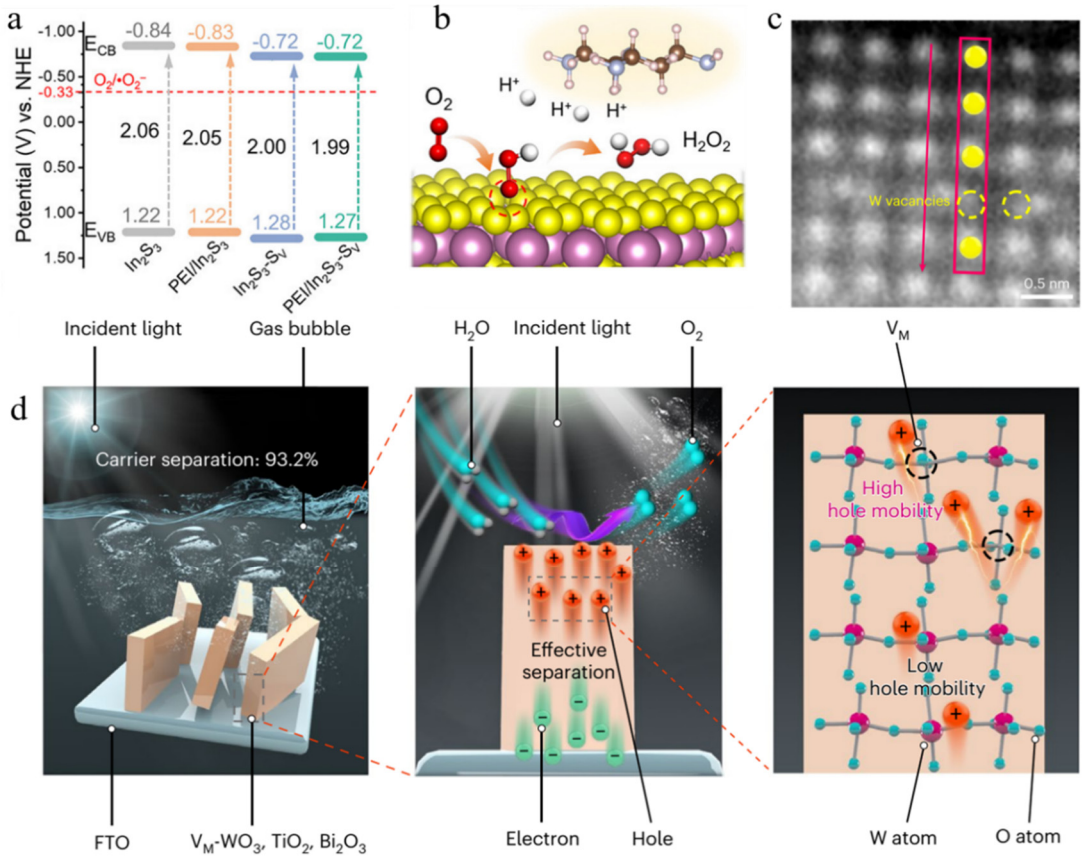

Figure 9. Fabrication and Applications of (**a**,**b**) S vacancy, reprinted with permission from Ref. [99]. Copyright 2025, Elsevier. (**c**,**d**) W vacancy, Reprinted with permission from Ref. [85]. Copyright 2025, Elsevier.

3. Common 2D PEC Materials

Since Geim's team successfully isolated monolayer graphene in 2004, 2D materials have garnered extensive attention due to their unique layered structures and distinctive physicochemical properties. Compared to bulk materials, 2D materials offer several advantages—including an exceptionally large specific surface area, a tunable electronic structure and short charge-transport distances that align well with the performance requirements for photoelectrodes in PEC systems. In recent years, various 2D materials, such as BiOX, GO, and MXenes etc., have been widely applied in the PEC field, greatly advancing PEC technology. Below is a systematic overview of the structure, modification strategies, properties, and applications of common 2D materials.

3.1. Metal Halide Oxides

Metal oxyhalides suitable for photoelectrocatalysis, represented by bismuth oxyhalides BiOX (X=Cl, Br, I), are a class of compounds composed of bismuth, oxygen, and halogen elements. They possess a unique 2D layered structure formed by the alternating stacking of $[Bi_2O_2]^{2+}$ layers and double X^- ion layers [100], the layered structure provides ample space for the polarization of corresponding atoms and orbitals, and the induced dipole moment facilitates the separation of photogenerated charges. Furthermore, as materials belonging to the indirect bandgap semiconductor category, the photoexcited electrons in BiOX must pass through certain k-space layers to reach the valence band, which inherently suppresses the recombination of photogenerated electrons and holes. Due to their distinctive layered structure and tunable band characteristics, BiOX materials demonstrate application potential in fields such as PEC sensing, environmental remediation, and energy conversion [98]. BiOX exhibits a broad light absorption range, capable of absorbing ultraviolet and part of visible light, enabling the conversion of solar energy into chemical energy. This efficient utilization of light energy holds significant importance for addressing energy challenges. BiOX itself is non-toxic. During the photocatalytic degradation of organic pollutants, it can convert

pollutants into harmless substances, thereby reducing environmental pollution, making it a green material for environmental purification. With appropriate bandgaps and a unique electronic band structure, BiOX can generate photogenerated charge carriers under light irradiation, and exhibits high separation efficiency of these electrons and holes, which helps to improve the efficiency of PEC reactions.

In solar-driven PEC water splitting, BiOX (BiOBr and BiOI) solid solutions demonstrate outstanding performance. For PEC hydrogen generation and overall PEC water splitting, the optimal solid solutions achieved a hydrogen evolution rate of 16.32 μmol g^{-1} h^{-1} and a photocurrent density of 1.5 mA cm^{-2}, respectively. This enhanced performance is attributed to higher electron density, shorter charge carrier transport distances, and a larger specific surface area (Figure 10a) [101]. Furthermore, the use of organic solvents containing hydroxyl groups (OH) in the preparation of BiOI results in OH enriched BiOI. The fundamental physical mechanism lies in the surface hydroxyl groups, which bond with the surface atoms of BiOI to alter the local electronic density distribution, thereby enabling effective modulation of the valence band energy levels. Furthermore, the hydroxyl-modified surface exhibits an enhanced affinity for adsorbing water molecules, facilitating the formation of surface OH. As key reactive species, these hydroxyl radicals can directly participate in photocatalytic oxidation reactions, further promoting the efficient transfer of photogenerated holes to organic pollutants. This OH-enriched BiOI exhibits a more positive surface maximum valence band (VBM), which means its photogenerated holes possess an enhanced oxidation capability, thereby demonstrating outstanding performance in PEC water splitting (Figure 10b) [102]. Lu et al. successfully prepared TiO_{2-x}/BiOCl heterojunction and investigated their photoelectrocatalytic activity in a three-electrode system. The composite materials were deposited on FTO substrates to form photoanodes (Figure 10c). The study revealed that the composite with a Bi/Ti molar ratio of 0.3 (labeled TB-0.3) exhibited superior charge separation and transport efficiency compared to other electrodes (TB-0.1 and TB-0.6). The increased photocurrent density observed for this material indicates a strong capability to promote the formation and transfer of electron-hole pairs while effectively suppressing their recombination (Figure 10d) [103].

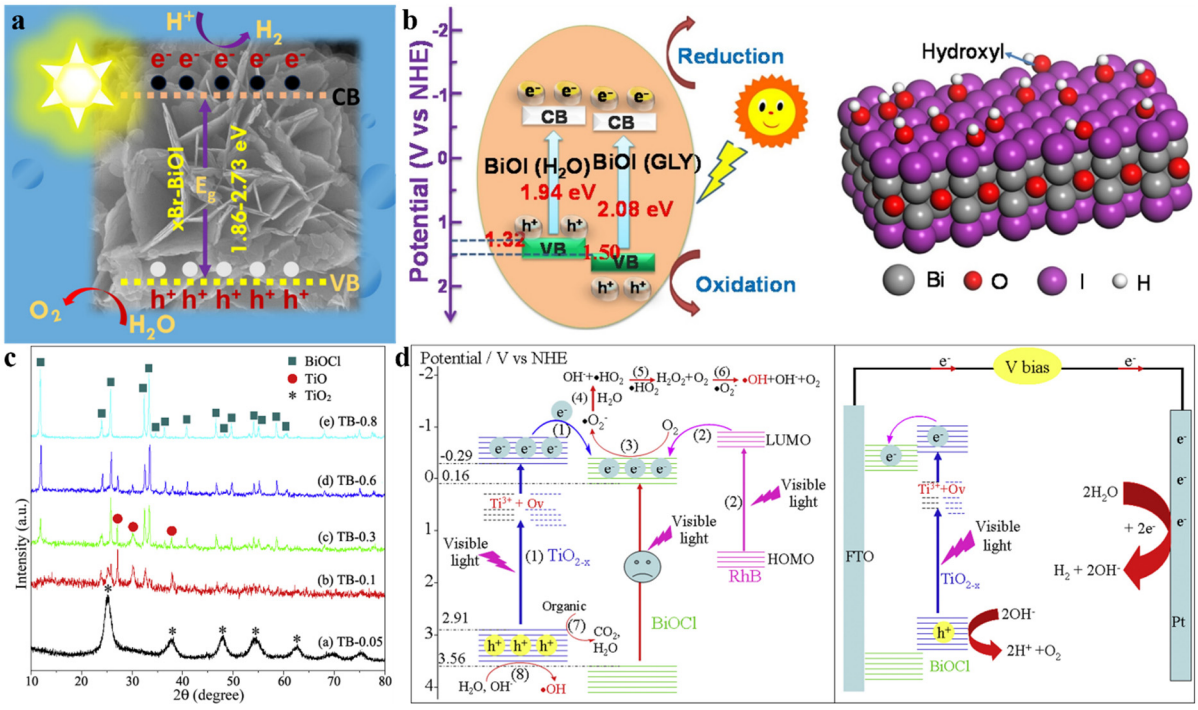

Figure 10. Fabrication and Applications of BiOX-Based 2D Materials (**a**) BiOX solid solutions, reprinted with permission from Ref. [101]. Copyright 2025, American Chemical Society. (**b**) OH-enriched BiOI, reprinted with permission from Ref. [102]. Copyright 2020, Elsevier. (**c**,**d**) TiO_{2-x}/BiOCl, Reprinted with permission from Ref. [103]. Copyright 2016, Elsevier.

The PEC conversion efficiency of BiOX materials is closely related to the generation, migration, and redox capability of their photogenerated carriers. Undoubtedly, promoting the efficient separation and rapid transport of carriers, increasing the utilization of incident light, and extending the response range to visible light are key to enhancing the PEC performance of BiOX. The wide application of BiOX materials is primarily attributed to their unique electronic, mechanical, and optical properties, combined with a layered structure that improves carrier transport and separation. However, for practical applications, relying solely on single-component BiOX to achieve

industrial-scale use remains unrealistic, as its PEC performance is ultimately limited by its intrinsic drawbacks. Future development trends toward BiOX-based composite materials formed through interface control strategies, such as heterojunction construction, elemental doping, and dye sensitization.

3.2. Mxene

MXene is a novel class of 2D materials composed of metal carbides or nitrides. MXenes are generally represented by the chemical formula $M_{n+1}X_nT_m$, where M denotes a transition metal, X represents carbon or nitrogen, and T stands for surface functional groups such as hydroxyl (-OH), halogen (-F, -Cl), and others. Typical examples include $Ti_3C_2T_x$, Nb_2CT_x, and Mo_2CT_x. Benefiting from high electrical conductivity, tunable surface chemistry, and excellent interfacial compatibility, MXenes have emerged as a functional core component in photoelectrocatalytic systems. Mxenes possess relatively strong light absorption capabilities and can work synergistically with light-absorbing semiconductors to effectively address key challenges in photocatalytic reactions, such as slow charge transfer, severe interfacial recombination, and insufficient reactant adsorption. As a result, MXene is widely used in applications such as water splitting and CO_2 reduction [104,105].

Zhang et al. developed a PEC photodetector based on a 2D $BiVO_4$/MXene Schottky junction, which demonstrated superior performance. The performance benefits originate from the built-in electric field formed at the $BiVO_4$/MXene Schottky junction interface, which not only facilitates the transfer of photogenerated electron-hole pairs but also suppresses interfacial charge recombination (Figure 11a,b). Furthermore, the 2D MXene nanosheets characterized by high metallic conductivity, possesses abundant surface functional groups, thereby providing an efficient electron transport channel [106]. The importance of functionally integrated sensors is becoming increasingly prominent across various applications, particularly in the field of intelligent wearables. However, optimizing the synergy between electrostatic and optical signals within PEC systems remains a key challenge. This study constructed a hierarchical ZnO/Bi_2O_3/BiOCl/BP/MXene ($Ti_3C_2T_x$) heterostructure, developing a PEC sensor specifically designed for electrostatic coupling and the detection of surface electromyographic (sEMG) signals with conducting directly on human skin. By sequentially integrating 2D black phosphorus and $Ti_3C_2T_x$ materials, the structural defects of the three-dimensional ZnO/Bi_2O_3/BiOCl framework were precisely repaired, effectively increasing the electrode contact area. The selectivity stems from the charge transfer characteristics engineered by defect engineering and the heterojunction interface effects. By introducing controllable defect sites into the heterojunction, these defect sites act as active centers with preferential adsorption affinity for the target molecule. The synergistic effect of the environmental electrostatic field and illumination further strengthened carrier transport, markedly improving the sensitivity for electrostatic field detection (Figure 11c) [107].

Based on the critical role of the aforementioned heterojunction engineering strategies in heterointerface regulation, the universal value of charge transport mediators in suppressing interfacial recombination has been further elucidated. Ye et al. inserted MXene nanosheets as a hole transport layer between the semiconductor and the co-catalyst, MXene nanosheets serve as an efficient hole transport mediator to enhance photoelectrochemical water oxidation. With their metal-level high hole mobility, MXene inserted between α-Fe_2O_3 and the cocatalyst creates a rapid hole transport channel. The built-in electric field at the MXene/α-Fe_2O_3 interface promotes directional hole migration and suppresses charge recombination. Meanwhile, the outer oxygen evolution cocatalyst protects MXene from oxidation, ensuring long-term stability. This hole transport layer strategy ultimately achieves significantly enhanced photocurrent density and onset potential. (Figure 11d,e). This work not only increased the photocurrent density of an α-Fe_2O_3 photoanode from 0.84 to 3.20 mA cm^{-2} with the onset potential negatively shifted by approximately 250 mV, but also verified the universal adaptability of this strategy to various systems such as $BiVO_4$, WO_3, and ZnO. The proposal of this "hole transport mediator" concept provides a new paradigm for addressing the interfacial recombination bottleneck in PEC water oxidation, marking a paradigm shift in interface engineering from passive defect remediation to active charge regulation [108]. In a separate study, Jing et al. constructed a 2D heterojunction of TiO_2/Ti_3CN MXene via a facile hydrothermal oxidation method and employed it as a photocathode for PEC CO_2 reduction (Figure 11f). It is noteworthy that MXene has evolved from a charge transport channel into a multifunctional mediator possessing both catalytic activity and capabilities for defect engineering. This work not only achieved the spatial integration of electron trapping centers (Ti^{3+}) and CO_2 activation sites but also eliminated the interfacial contact bottleneck inherent in traditional physical mixing through an in-situ growth strategy. In the constructed Pd@TiO_2/Ti_3CN || SCE || $BiVO_4$ PEC system, CO_2 reduction products included formic acid, methanol, and C_2 species (ethanol), with a total generation rate reaching 45.6 μM cm^{-2} h^{-1} (Figure 11g). This study provides a key experimental paradigm for understanding the dual role of defect-state species in PEC CO_2RR—simultaneously suppressing recombination and stabilizing intermediates (Figure 11h). Furthermore, DFT calculations indicated that the TiO_2/Ti_3CN heterojunction can spontaneously activate CO_2

and stabilize key reaction intermediates, thereby promoting HCOOH formation. This research highlights the significant potential of titanium carbonitride MXenes in the field of green energy conversion [109].

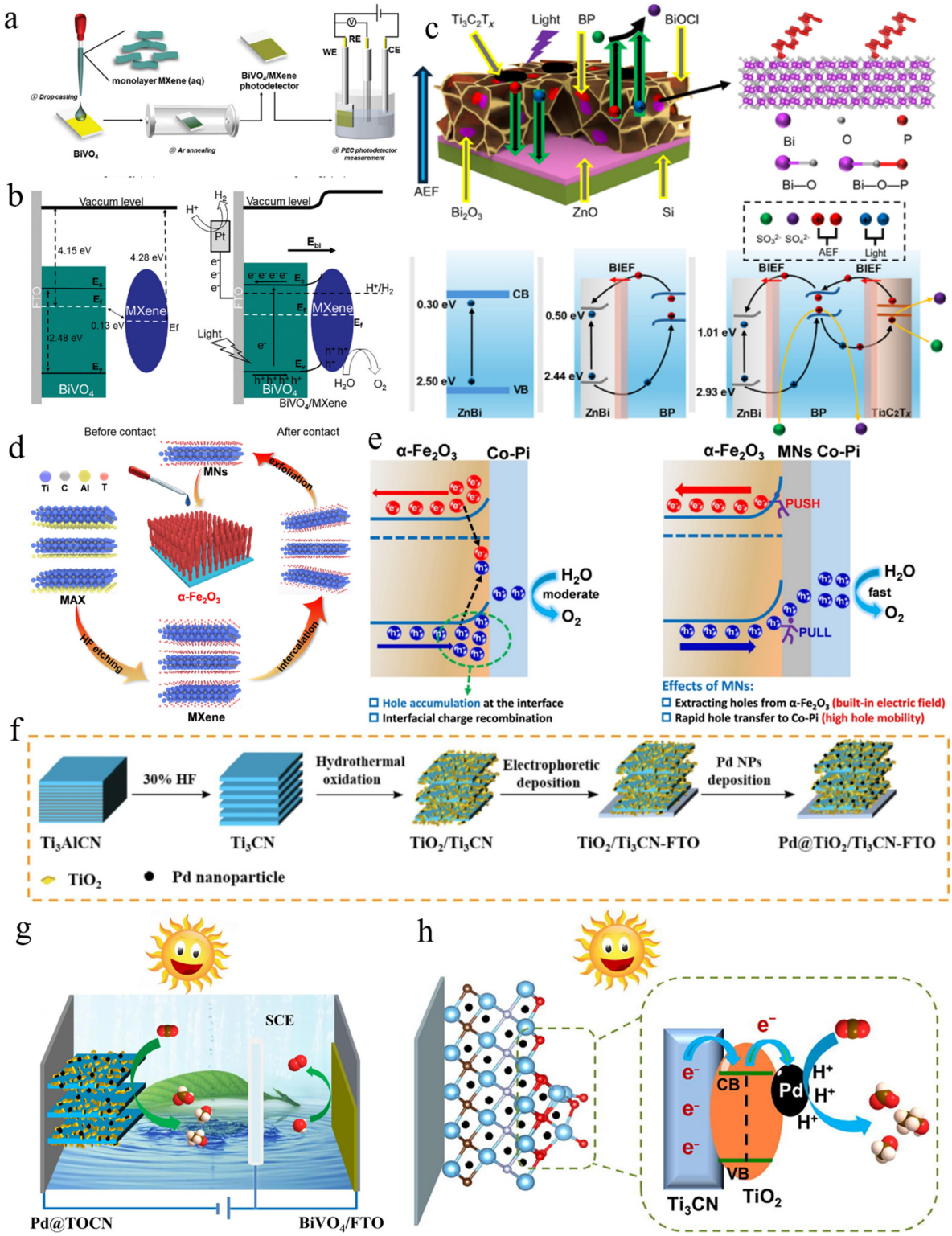

Figure 11. Synthesis and Applications of MXene-Based 2D Materials: (**a**,**b**) $BiVO_4$/MXene, reprinted with permission from Ref. [106]. Copyright 2024, John Wiley and Sons. (**c**) B/Bi/$Ti_3C_2T_x$/BP [107], (**d**,**e**) MNs/α-Fe_2O_3, reprinted with permission from Ref. [108]. Copyright 2021, Elsevier. (**f**–**h**) TiO_2/Ti_3CN, reprinted with permission from Ref. [109]. Copyright 2023, Elsevier.

MXene demonstrates unique advantages in the field of PEC due to its high conductivity, tunable structure, and strong synergistic effects. Particularly within heterojunction systems, it can significantly enhance charge separation efficiency and reaction selectivity, and has been widely applied in scenarios such as water splitting,

CO_2 reduction, and pollutant degradation. However, issues such as weak light absorption, easy stacking, insufficient stability, and limitations in synthesis constrain its practical application potential. By compositing with light-responsive materials, structural modification, and optimization of green synthesis processes, MXene-based catalysts are expected to overcome existing bottlenecks and become key materials bridging clean energy conversion and environmental remediation.

Notably, in research on the selective synthesis of C_1 and C_2 products via PEC CO_2 reduction, Young Soo Kang's group utilized different 2D materials to obtain various hydrocarbons. By demonstrating how precise engineering of 2D material interfaces can accurately regulate proton transport, intermediate lifetime, and multi-electron transfer processes in CO_2 reduction reactions, thereby achieving selective synthesis of different hydrocarbons. First, by coating a Nafion layer on a TiO_2 dark cathode, they fabricated a layer-by-layer N_f-TiO_2 photoelectrode that significantly increased the proton concentration at the cathode surface. This shortened the lifetime of the key $CO_2^{-}\cdot$ radical intermediate, suppressed its dimerization pathway, and shifted the product selectivity from a methanol/ethanol mixture to highly selective methanol production (Figure 12a). Subsequently, they expanded the research to the synergy between oxygen vacancy activation and charge separation, by constructing an rGO-grafted NiO-CeO_2 p-n heterojunction. In this system, the oxygen vacancies in CeO_2 effectively adsorbed and activated CO_2 molecules, while the introduction of NiO/rGO greatly promoted charge separation and electron enrichment onto the rGO. The accumulated electrons facilitated efficient multi-electron transfer via rGO, enabling the highly selective reduction of activated CO_2 to formaldehyde (Figure 12b). Furthermore, they further integrated and dynamically regulated the aforementioned factors in 2022. They functionalized rGO on a ZnO@ZnTe core-shell structure (Figure 12c). When both the anode and cathode were illuminated simultaneously, the rGO layer itself was photoexcited, generating additional electrons and providing enhanced multi-electron shuttling capability. This prolonged the lifetime of the formyl (CHO·) intermediate, allowing sufficient time for C-C coupling and thereby switching the product selectivity to ethanol (Figure 12d).

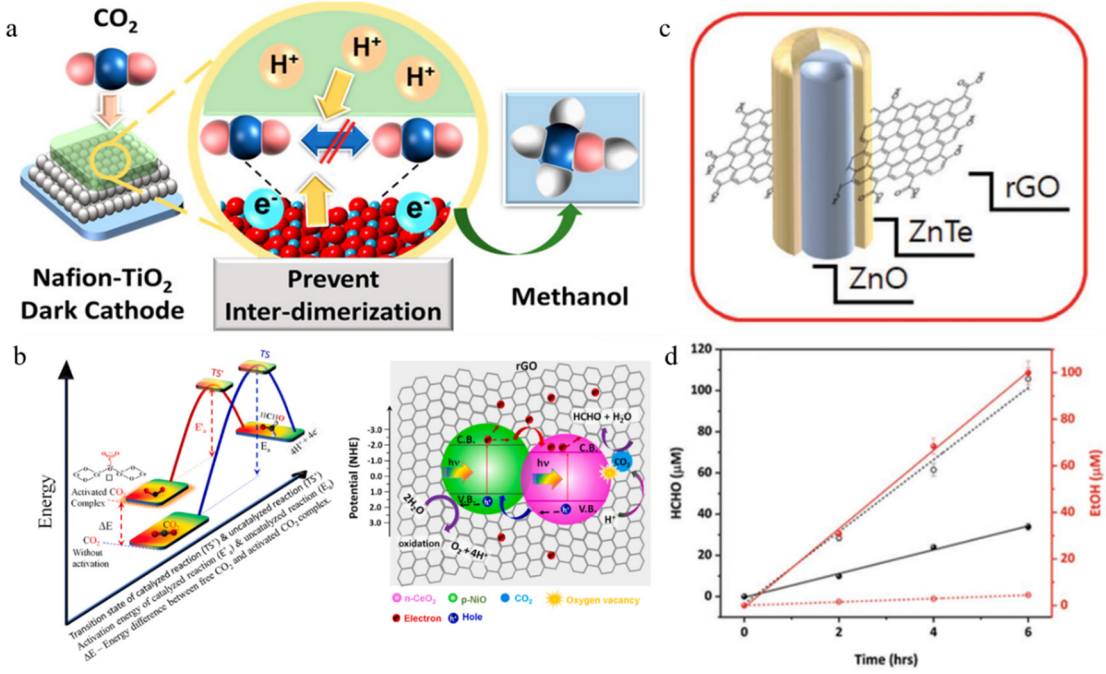

Figure 12. Hydrocarbons selectively synthesized via CO_2RR using different 2D structured photoelectrodes (**a**) layer-by-layer Nf-TiO_2, reprinted/adapted with permission from Ref. [110]. Copyright 2019, American Chemical Society. (**b**) NiO/CeO_2/rGO, reprinted/adapted with permission from Ref. [111]. Copyright 2021, Elsevier. (**c,d**) ZnO@ZnTe@rGO, reprinted/adapted with permission from Ref. [112]. Copyright 2025, John Wiley and Sons.

3.3. g-C_3N_4

Polymeric graphitic carbon nitride (g-C_3N_4) is a distinctive allotrope of covalent carbon nitride, characterized by a layered stacking structure. Within this structure, each planar layer consists of triazine units interconnected by amino groups, forming an extensive, graphite-like π-conjugated plane that facilitates significant interlayer electron conductivity [113]. Owing to its highly condensed and conjugated architecture, g-C_3N_4 exhibits remarkable stability in neutral, strongly acidic, and alkaline environments. It possesses a suitable valence band (VB), conduction band (CB), and a bandgap of 2.7 eV, making it well-suited for photocatalytic hydrogen evolution [114].

The weak van der Waals forces between layers allow the exfoliation of bulk g-C_3N_4 into 2D g-C_3N_4 nanosheets, which demonstrate enhanced performance in photocatalytic water splitting [113,115]. In addition to the increased specific surface area, the bandgap of g-C_3N_4 widens as the nanosheets are thinned down, accompanied by shifts of the CB and VB toward more negative and positive levels, respectively. These electronic modifications further contribute to the superior performance in water splitting applications.

Solid-phase synthesis strategies demonstrate unique scalability and stability advantages in interface engineering. Wang et al. extended this concept to nonbarrier and p quantum dots onto ultrathin g-C_3N_4 surfaces, constructing an efficient 0D/2D photocatalytic system (Figure 13a). The material design, featuring highly dispersed Ni_2P quantum dots anchored to g-C_3N_4 via Ni-N coordination bonds, ensures intimate interfacial contact and establishes efficient charge transfer channels. This configuration promotes the directional migration of photogenerated electrons, effectively curbing carrier recombination. Leveraging the quantum confinement effect, the Ni_2P dots facilitate rapid charge transport and serve as active centers to boost surface reaction kinetics. Moreover, the enhanced visible light response upon Ni_2P incorporation works in concert with these charge dynamics to synergistically elevate the overall photoelectric conversion efficiency. This work not only achieved a hydrogen evolution rate of 1503 μmol h^{-1} g^{-1}, far exceeding that of Pt/g-C_3N_4 with equivalent loading (560 μmol h^{-1} g^{-1}), but also enhanced the photocurrent response to 11 times that of pure g-C_3N_4, providing key design guidelines for developing low-cost, non-precious metal co-catalysts [116]. To further expand the functional boundaries of g-C_3N_4, Zhu et al. transformed it from a single carrier into a key component with dual functions of photosensitization and structural guidance by constructing a g-C_3N_4@ZnO core-shell structure. This core-shell design fully leverages the band alignment and interfacial coupling effects between g-C_3N_4 and ZnO, achieving a dual synergistic enhancement mechanism (Figure 13b). g-C_3N_4 evolves from a 2D substrate for dispersing co-catalysts into an active shell coating ZnO nanoparticles. When the g-C_3N_4@ZnO core-shell composite is employed as a photoanode, the dual synergistic effect of the unique core-shell structure and electro-oxidation-assisted photocatalysis enables excellent PEC performance under visible light. This significantly surpasses the performance of single-component materials, fully highlighting the dual role of g-C_3N_4 as both a structural director and a photosensitizer [117].

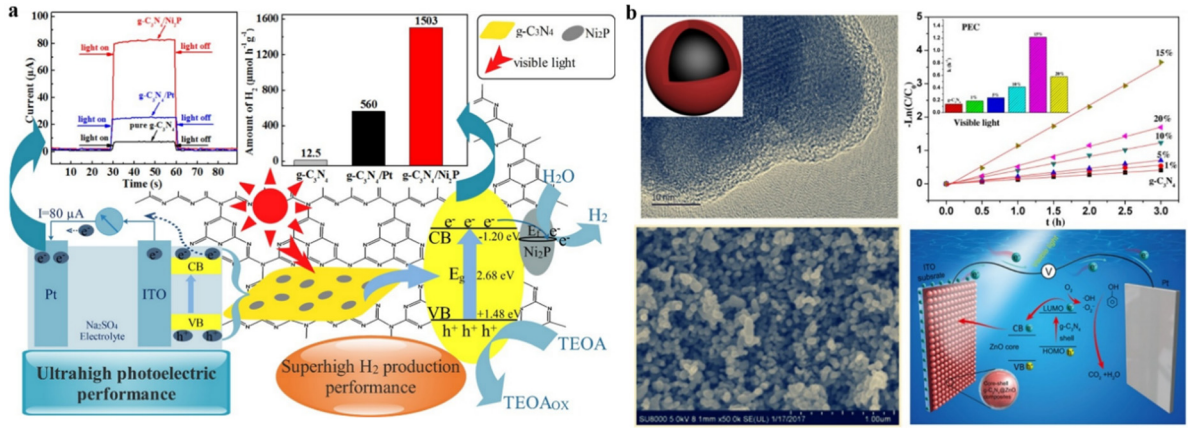

Figure 13. Synthesis and Applications of g-C_3N_4-Based 2D Materials: (**a**) Ni_2P/g-C_3N_4, reprinted/adapted with permission from Ref. [116]. Copyright 2023, Elsevier. and (**b**) g-C_3N_4@ZnO, reprinted/adapted with permission from Ref. [117]. Copyright 2017, Elsevier.

The core function of g-C_3N_4 in PEC lies in its 2D structure, which provides an extensive contact interface and abundant active sites. It drives efficient interfacial charge separation and suppresses carrier recombination through well-matched band structures, while serving dual roles as both a visible-light photosensitizer and a structural director. Future development will focus on the precise construction of ultrathin, porous, and three-dimensional hierarchical nanostructures to maximize surface effects; designing diverse heterojunction systems such as 0D/2D, 2D/2D, and core-shell architectures to achieve multi-fold synergistic enhancement; combining theoretical calculations and machine learning to optimize band engineering and interface matching; and advancing large-scale preparation techniques and device integration to address long-term stability bottlenecks. These efforts aim to accelerate its transition from laboratory research to industrial-scale PEC applications.

3.4. LDHs

LDHs are a class of layered double hydroxides with the general formula $[M^{2+}_{1-x}M^{3+}_{x}(OH)_2]^{x+}(A^{n-})_{x/n}\cdot mH_2O$, where M^{2+} represents divalent metal cations (e.g., Mg^{2+}, Ni^{2+}, Co^{2+}, Zn^{2+}, Cu^{2+}, Ca^{2+}), M^{3+} denotes trivalent cations (e.g., Al^{3+}, In^{3+}, Cr^{3+}, Fe^{3+}, Mn^{3+}, Co^{3+}, Ga^{3+}), A stands for exchangeable interlayer anions (e.g., $NO3^{-}$, CO_3^{2-}), y represents the $M^{3+}/(M^{2+}+M^{3+})$ ratio typically ranging from 0.17 to 0.33, and n is the charge number of the interlayer anion. Structurally, LDHs consist of octahedral MO_6 units where a transition metal atom is centered at the octahedron with six oxygen atoms at the vertices. The edges of these MO_6 octahedra connect to adjacent metal ions, forming an infinite 2D layered framework [118,119]. The core advantages of LDHs lie in their ease of preparation, low raw material cost, good thermal stability, and large specific surface area, which have enabled their widespread application across various fields—particularly in photo/electrocatalysis [120]. More importantly, by varying the metal ions within the LDH structure, a rich family of isostructural analogues can be obtained, allowing the design and synthesis of LDHs with tailored metal and anion compositions to meet specific requirements. However, most LDHs possess a wide bandgap (i.e., Mg or Zn or Al-based LDH), making them difficult to activate under visible light [121,122]. Consequently, in the field of PEC sensors, LDHs (i.e., NiFe-LDH) are often utilized as photosensitizers to enhance light absorption and facilitate the separation of photogenerated electron-hole pairs [123,124]. Nevertheless, pristine LDHs suffer from several limitations, including slow charge carrier mobility, high electron-hole recombination rates, low electrical conductivity, and a tendency to agglomerate, which restrict their practical applicability. To address these challenges, strategies such as composite formation, cocatalyst integration, semiconductor coupling, and ternary heterostructure engineering have been explored, opening new possibilities for LDHs in photocatalytic, electrocatalytic, and photoelectrochemical applications.

Regulating interfacial charge transfer pathways by constructing heterojunctions is an effective strategy for enhancing material performance. Particularly for layered materials such as NiFe-LDH, coupling with suitable semiconductor materials to form Z-scheme or p-n heterojunctions can effectively suppress electron-hole recombination. The study by An et al. provides a representative example: they composited p-type MoS_2 with n-type NiFe-LDH and confirmed the key role of the formed Z-scheme heterojunction in promoting directional separation of photogenerated charges and improving photocurrent conversion efficiency (Figure 14a). Furthermore, this work achieved a one-step in-situ construction of the heterojunction, thereby obtaining a binder-free monolithic photoanode. This synthetic strategy not only simplifies the process but also ensures intimate contact between the two 2D materials through electrostatic self-assembly, laying the foundation for efficient interfacial charge transport [125]. Although the MoS_2/NiFe LDH heterojunction effectively enhances the separation efficiency of photogenerated charges via the constructed Z-scheme structure, its long-term stability under strong oxidation potentials and electrolyte environments still faces challenges. To significantly enhance the durability of photoanodes while maintaining high activity, research strategies are gradually shifting toward introducing stable components with high chemical inertness and excellent conductivity. In this regard, Jang et al. successfully synthesized Au-doped NiFe LDH (Au-NiFe LDH) via a two-step electrodeposition method. The incorporated Au atoms effectively fill nickel or iron vacancies, thereby stabilizing the overall structure. Study demonstrates that the synergy between Au and NiFe-LDH significantly enhances photoanode performance with enhanced photocurrent density and over 50 h stability, setting a new record for buried junction-free silicon-based photoanodes. The improvement in performance is mainly attributed to the enhancement of charge kinetics through aluminum doping. The introduction of aluminum optimizes the band structure of the material and accelerates hole extraction and transport; meanwhile, the doping process effectively passivates surface/interface defect states. These two factors work synergistically to significantly reduce charge recombination losses, thereby improving the photoelectric conversion efficiency (Figure 14b) [126]. Furthermore, Zheng et al. provided an energy-saving and cost-effective pathway for oxidizing 5-hydroxymethylfurfural (HMF) to produce the high-value-added product 2,5-furandicarboxylic acid (FDCA). On a NiFe-LDH/$BiVO_4$ photoanode, the solar-driven TEMPO-mediated HMF indirect-oxidation achieved remarkable efficiency: the FDCA yield increased from 1.7%/2.5% for bare $BiVO_4$ to 100%/100% for the NiFe-LDH/$BiVO_4$ at 0.7 V_{RHE} (Figure 14c), demonstrating a substantial enhancement in PEC catalytic efficiency and practicality. Carrier behavior dynamics studies revealed a larger surface potential difference (1.5-fold) in NiFe LDH/$BiVO_4$, validating effective charge separation and transfer, which can supply more holes for HMF oxidation (Figure 14d). Secondly, density functional theory (DFT) calculations reveal that TEMPO molecules preferentially adsorb onto the electrode surface over HMF molecules. This selective adsorption enables TEMPO to function as a redox mediator, where it is first oxidized by photogenerated holes to form $TEMPO^{+}$, which subsequently chemically oxidizes HMF. This mediated pathway establishes a reaction route that is thermodynamically and kinetically more favorable than direct water oxidation. This work indicates that solar-driven biomass upgrading can serve as a viable anode reaction to replace the sluggish water oxidation process in solar fuel production [127].

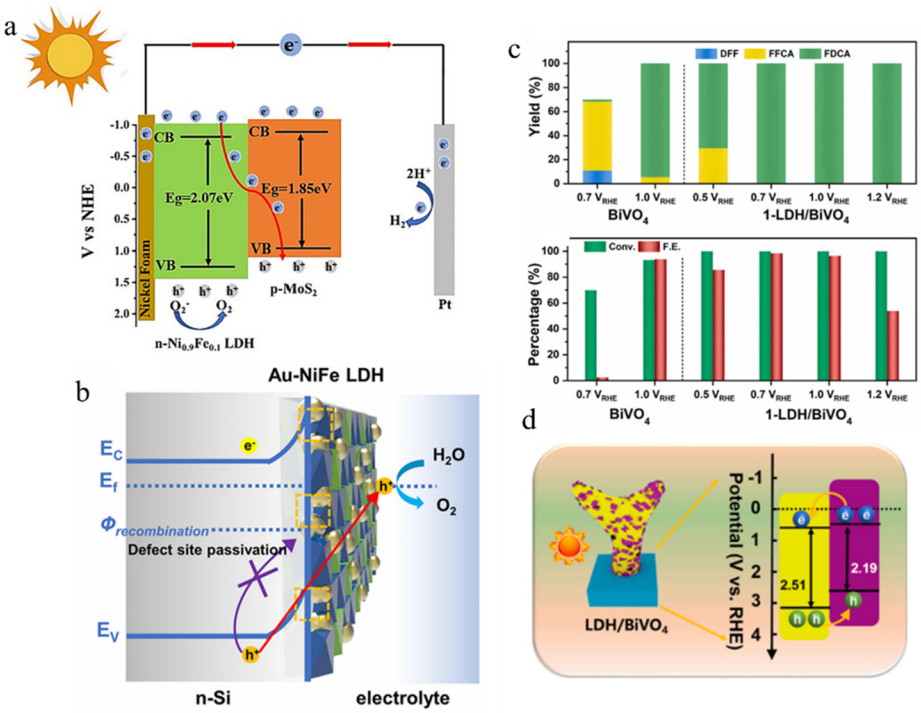

Figure 14. Preparation and Applications of 2D LDH-Composed Materials: (**a**) MoS_2/NiFe-LDH, reprinted/adapted with permission from Ref. [125]. Copyright 2024, Elsevier. (**b**) Au-NiFe LDH, reprinted/adapted with permission from Ref. [126]. Copyright 2023, Royal Society of Chemistry. (**c**,**d**) NiFe-LDH/$BiVO_4$, reprinted/adapted with permission from Ref. [127]. Copyright 2023, Elsevier.

Although the above strategies are effective, there remains room for improvement in the intrinsic properties of binary LDH laminates, such as their electronic structure, active site density, and stability. To optimize the fundamental performance of catalysts at a more foundational level, research focus has shifted to the design of ternary LDHs. By introducing a third metal cation (e.g., Al^{3+}) into the classical NiFe binary laminates, the local coordination environment, charge distribution, and electronic interactions among metal ions within the laminates can be precisely regulated. Cui et al. elucidated the mechanism behind the performance enhancement achieved by constructing an amorphous ternary NiFeAl-LDH on the $BiVO_4$ surface. The structurally disordered amorphous LDH strengthened the interaction with $BiVO_4$, inducing the formation of a distorted octahedral coordination geometry. This led to a reconstruction of the Ni^{3+} e_g/t_{2g} valence electron orbitals from a degenerate to a non-degenerate state and prompted a spin-state transition from high-spin to low-spin (Figure 15a). This study established a clear causal relationship between amorphization and spin-state regulation [128,129].

The aforementioned studies, by tuning the composition and structure of NiFe-based LDHs, aim to improve the efficiency of the energy-intensive half-reaction of water oxidation. However, from a systemic energetics perspective, utilizing photogenerated holes to oxidize organics that are more challenging to oxidize yet hold higher economic value—such as biomass platform molecules—not only provides a more efficient driving force for the hydrogen evolution reaction but also enables the simultaneous production of value-added chemicals. This represents a more atom- and energy-economical strategy of "killing two birds with one stone." In this direction, Hao et al. recently reported a pioneering work: using a metal halide perovskite as the photoanode combined with a CoNiFe layered double hydroxide (LDH) co-catalyst, they successfully constructed an "unassisted" PEC system. Without requiring any external bias, this system efficiently couples water reduction for hydrogen production with the selective oxidation of glucose into high-value products, achieving a stable photocurrent density of 10.1 mA cm^{-2}. A techno-economic feasibility assessment highlights the commercial potential of the PEC H_2-GOR technology, paving a new pathway toward efficient and economical solar-driven co-production of fuels and chemicals [130]. In a separate study, Shi et al. uniformly anchored 2D ternary CoNiFe-LDH nanosheets onto 1D Ta_3N_5 nanotube arrays to create a novel integrated photoanode. Acting as electron collectors, the CoNiFe-LDHs accelerate electron extraction from photoexcited Ta_3N_5 to the surface water oxidation reaction (WOR), thereby promoting electron-hole pair separation and ultimately significantly enhancing photoelectrochemical water splitting performance. Furthermore, CoNiFe-LDHs were more effective in improving PEC performance than the three sets of binary metal-LDHs. By further replacing the WOR with the glycerol oxidation reaction (GOR), the composite photoelectrode achieved a tenfold increase in solar energy conversion efficiency, reaching 0.56%, with nearly

100% FE for the simultaneous production of formate and hydrogen. Importantly, the stability of Ta_3N_5 was greatly enhanced due to the CoNiFe-LDH loading and the synergistic effect of the anodic GOR (Figure 15b). The significantly enhanced PEC performance is primarily attributed to increased surface active sites, promoted electron extraction and utilization, and particularly improved charge separation efficiency [131].

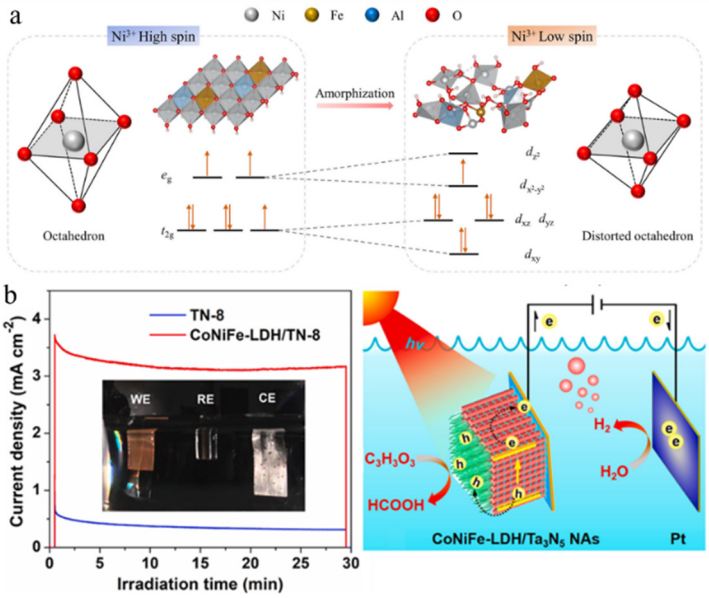

Figure 15. Preparation and Applications of LDHs-Based 2D Materials (**a**) NiFeAl-LDH/$BiVO_4$, reprinted/adapted with permission from Ref. [128]. Copyright 2025, John Wiley and Sons. (**b**) CoNiFe-LDH/Ta_3N_5, reprinted/adapted with permission from Ref. [132]. Copyright 2021, Elsevier.

4. Applications of 2D Nanomaterials in PEC Sensors

4.1. Systematic Classification Framework for 2D Nanomaterial-Based PEC Sensors

In PEC sensing, a distinct research paradigm integrates optical excitation with electrochemical detection using semiconductor materials for signal transduction. The separation between excitation and detection enables low background noise and high gain, offering benefits such as high sensitivity, low detection limits, room-temperature operation, low power consumption, and miniaturization. Based on signal-response relationships, PEC modes are classified as signal-off, signal-on, or photocurrent polarity-switching. While 2D nanomaterials have been widely explored in PEC sensing due to their advantages over conventional materials, they still face intrinsic limitations. To improve selectivity and light utilization, further modification, functionalization, or the design of advanced nanocomposites is often required. This chapter systematically reviews the progress of PEC sensors based on 2D semiconductor nanomaterials, aiming to provide a comprehensive understanding of this emerging field. Table 5 summarizes representative 2D nanomaterials and their applications in PEC sensing for comparative insight.

Table 5. Performance comparison of PEC sensors with different transduction mechanisms.

Transduction Mechanism Category	Specific Physical Mechanism	2D Material	Target/Limit of Detection	Applicable Complex Environment/Matrix	Ref.
Signal-off	Energy transfer and DNA signal amplification	Zn MOFs, Pt@Cu_2O CNs	Acetamiprid/20.2 fM	Vegetables	[133]
	Charge transfer, coordination chelation	BiOI/TiO_2	Chlorpyrifos/0.24 pg mL^{-1}	Agricultural by-products, Environmental water samples	[134]
Signal-on	Charge transfer	Ti_3C_2-Cl-BOC/BOC	Ciprofloxacin/121.21 pM	Milk, tap water	[135]
	Charge transfer	OVs-Bi/BiOB$r_{0.5}I_{0.5}$	Oxytetracycline/1.45 pM	Milk	[136]
	Integrated "Recognition-Blocking-Enhancement"	Cu-HHTP@Zn-TCPP	Sulfide/0.62 μM	Animal-derived foods (eggs, pork, shrimp)	[137]
Photocurrent Polarity Switching	Colorimetric/PEC dual-mode synergy	Bi/Bi_2MoO_6	γH_2AX (DNA damage biomarker)/70.8 fg/mL	Per- and polyfluoroalkyl substances	[138]
	Charge transfer	AgI/AgNCs/Au/Bi_2WO_6	miRNA-21/0.085 fM	Cell extracts, tissue samples	[139]

4.1.1. Signal-Off Mode

Signal-off PEC sensing is the most commonly used mode, where changes in target analyte concentration alter either the surface properties of the photoactive material [140,141] or the concentration of electron donors/acceptors [142] thereby modulating the photocurrent response. Steric hindrance effects are widely employed as a signal amplification strategy in signal-off PEC immunoassays. Enzymatic precipitation, an effective and straightforward approach, generates insoluble precipitates on the electrode surface that impede interfacial electron transfer, leading to a significant decrease in photocurrent. A novel cathodic PEC sensor based on g-C_3N_4 coupled with a zirconium-based porphyrin metal-organic framework (PCN-222) was developed for ultrasensitive detection of kanamycin (KAM). Using PCN-222@g-C_3N_4 as the photoactive platform, a label-free detection strategy achieved ultrasensitive KAM detection within 5–6 min, with a linear range of 1–1000 nM and a detection limit of 0.127 nM (Figure 16a) [143]. Compared to conventional methods such as RP-HPLC-UV and LC/MS for KAM analysis, which require at least 20–30 min of injection time and offer detection limits of 78,000 and 5160 nM, respectively [144,145], the PEC sensor demonstrates substantially superior efficiency and detection limits (Table 6).

Furthermore, Fu et al. employed a glassy carbon electrode modified with deposited Au (depAu) and BiOI/BiOBr heterojunctions as both the photoactive sensing interface and the substrate for capture antibody loading. Using gold nanoclusters encapsulated within polyethyleneimine-copper complexes (Ab_2-Au@PEI-Cu) as signal quenchers for the detection antibody, the photocurrent decreased with increasing concentrations of target carcinoembryonic antigen (CEA) introduced via sandwich-type immunoreaction. This proposed intelligent PEC immunoassay platform exhibited a wide linear detection range (1.0 fg mL^{-1} to 2.0 ng mL^{-1}), an exceptionally low detection limit of 0.11 fg mL^{-1}, and satisfactory selectivity and stability (Figure 16b). Moreover, this PEC sensing strategy can be readily extended to the analysis of other tumor markers, offering new perspectives for early disease diagnosis utilizing bismuth oxyhalide-based materials as photoactive components [146].

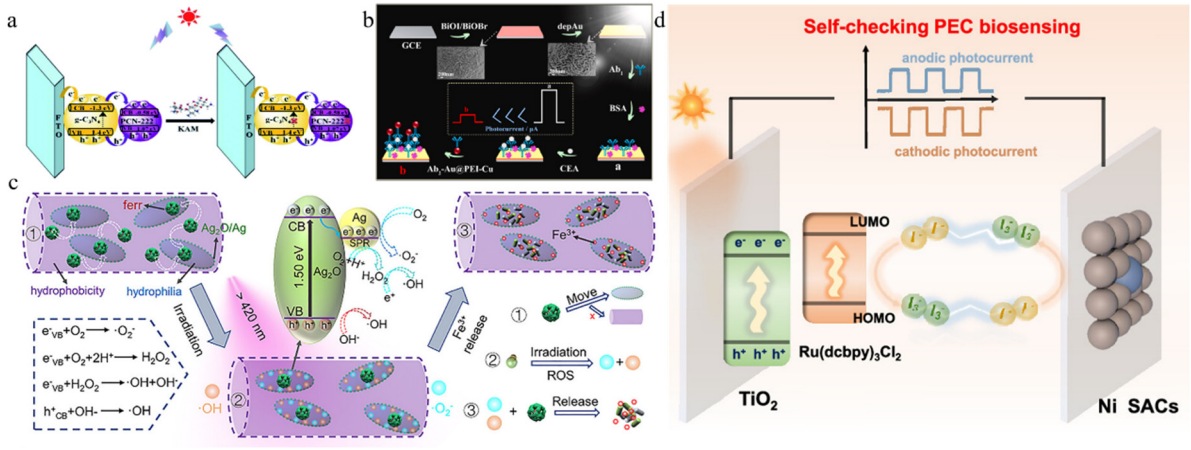

Figure 16. Fabrication and Applications of 2D Nanomaterial-Based PEC Photodetectors with Different Transduction Mechanisms: (**a**,**b**) Signal-off [143,146], (**c**) Signal-on [147] and (**d**) Photocurrent Polarity Switching [148]. (**a**) Reprinted/adapted with permission from Ref. [143]. Copyright 2021, copyright Royal Society of Chemistry. (**b**) Reprinted/adapted with permission from Ref. [146]. Copyright 2023, copyright Elsevier. (**c**) Reprinted/adapted with permission from Ref. [147]. Copyright 2025, copyright Wiley-VCH. (**d**) Reprinted/adapted with permission from Ref. [148]. Copyright 2023, American Chemical Society.

4.1.2. Signal-On Mode

Signal-on photoelectrochemical sensing offers enhanced sensitivity and accuracy by mitigating interference from background signals. In this mode, signal amplification is achieved through target recognition and the involvement of photoactive materials, resulting in a positive correlation between photocurrent and analyte concentration. Electron donors or acceptors are key components, and strategies based on the generation or consumption of photogenerated carriers are commonly employed. For example, using ferritin as a model target, researchers developed a nanoreactor with integrated capture, dissociation, and signal amplification functions embedded within electrospun nanofibers. Under illumination, the Ag_2O/Ag heterojunction generates reactive oxygen species that disrupt ferritin, releasing Fe^{3+} ions. These ions act as electron mediators, bridging conductive gaps within the nanofibers and significantly enhancing the photocurrent. This strategy enables highly sensitive ferritin detection with a wide linear range (10^{-8}–10^{2} mg mL^{-1}) and an ultra-low detection limit of 5 pg mL^{-1}, outperforming most conventional protein assays (Figure 16c) [147].

4.1.3. Photocurrent Polarity-Switching Mode

In practical PEC sensing, complex samples often contain interferents that can unpredictably alter photocurrent signals. Conventional signal-off and signal-on modes, relying on unidirectional changes, are susceptible to false-positive or false-negative results. Photocurrent polarity-switching offers an effective solution: upon target recognition, the photocurrent polarity reverses, negating interference from coexisting substances and thereby enhancing detection accuracy, reliability, and anti-interference capability. Polarity switching can be achieved by modulating the incident wavelength, adjusting the applied bias potential [149] or introduction of target analytes [150], with bias potential modulation being the most common. For example, a self-validating PEC biosensor generating reversible photocurrent polarity under low bias potentials was developed. In this system, nickel single-atom catalysts (Ni SACs) promote the cyclic regeneration of the I^-/I_3^- redox couple, amplifying the photocurrent signal (Figure 16d). This sensor enables sensitive detection of acetylcholinesterase (AChE) while eliminating false signals through correlation analysis between anodic photocurrent, target concentration, and cathodic photocurrent, thereby achieving self-calibration and enhanced accuracy [148].

4.2. Applications of PEC Sensors in Complex Environment and Matrices

Evaluating PEC sensors in complex matrices (e.g., milk, soil, wastewater) holds greater practical significance than relying solely on idealized buffer conditions. For instance, Zhang et al. developed a PEC sensor based on a Cu-HHTP@Zn-TCPP MOF-on-MOF architecture for detecting H_2S released during spoilage of animal-derived foods. Electron transfer from Zn-TCPP to Cu-HTTP quenches the photocurrent; upon sulfide exposure, coordination with copper nodes forms CuS, inhibiting electron transfer and restoring the signal. This "signal-on" strategy achieves a linear range of 0.1–500 μM and a detection limit of 0.62 μM. Integrated with a smartphone and miniature electrochemical analyzer, the portable platform enabled sensitive H_2S detection in eggs, pork, and shrimp (Figure 17a) [137]. In another example, an n-n heterojunction was fabricated using BiOI and TiO_2 for organophosphorus pesticide detection. The synergistic effect between BiOI and TiO_2 significantly enhanced the photoelectrochemical signal. In the presence of chlorpyrifos, chelation between chlorpyrifos and BiOI hindered interfacial charge migration, substantially decreasing the photocurrent response and enabling highly sensitive detection (Figure 17b) [134]. Antibiotics used as feed additives can leave harmful residues in animal products, posing risks to human health. To address this, a PEC sensor was developed for rapid detection of streptomycin (STR). It uses a $CdIn_2S_4/SnO_2$ electrode and platinum-copper nanoclusters (PtCu NCs) that mimic enzyme activity to enhance signals. The PtCu NCs, linked to complementary DNA, block the photocurrent. When STR binds to the aptamer, the PtCu NCs detach, reducing a precipitation reaction and increasing the photocurrent, enabling effective STR monitoring (Figure 17c) [151].

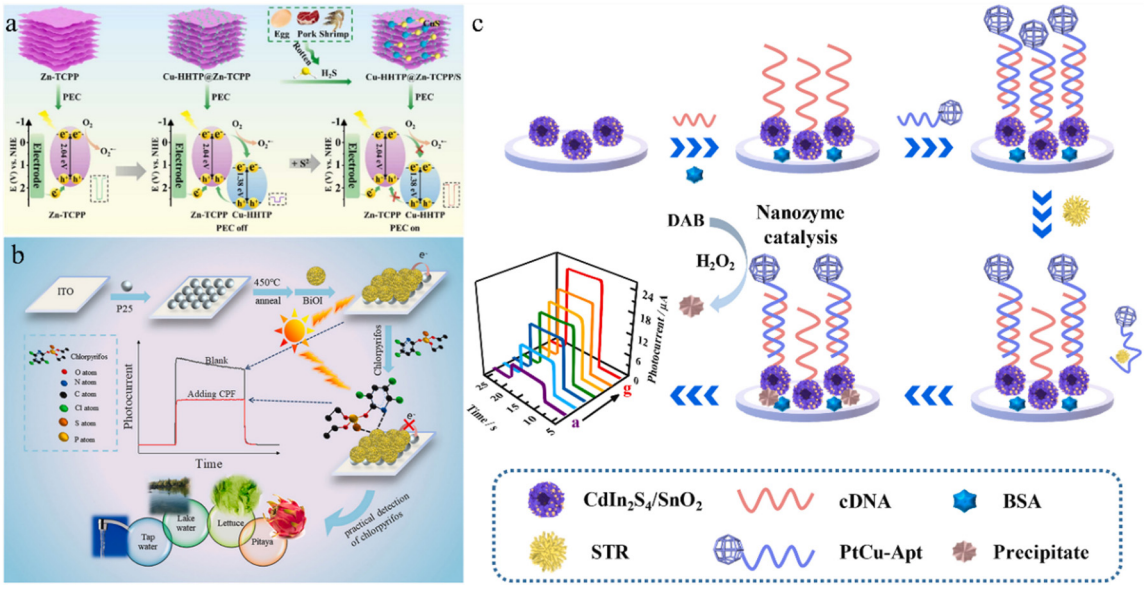

Figure 17. Applications of PEC sensors in Complex Environments or Matrices, (**a**) H_2S released during the spoilage of animal-derived foods, reprinted/adapted with permission from Ref. [137]. Copyright 2025, Elsevier. (**b**) Chlorpyrifos residues in agricultural crops, reprinted/adapted with permission from Ref. [134]. Copyright 2023, Elsevier. (**c**) Excessive antibiotics in animal-derived foods, Reprinted/adapted with permission from Ref. [151]. Copyright 2023, Elsevier.

For comparative purposes, Table 6 summarizes the detection ranges and limits of detection for the same target analyte using different analytical methods. It is evident that PEC sensors are not only adaptable to complex environmental matrices but also exhibit substantially higher detection accuracy.

Table 6. Detection ranges and LOD for the same target analyte using different detection methods in identical and different matrices.

Analyte	Detection Method	Matrix	Instrumentation	Linear Range	LOD	Ref.
Glucose	PEC-sensor	human blood serum (B-R buffer solution)	CHI1030C Electrochemical system	0.5–0.5 × 10^6 nM	0.17 nM	[61]
	PEC-sensor	human blood serum (0.1 M KOH)	CHI660D Electrochemical system	5 × 10^2–3 × 10^7 nM	10 nM	[152]
	RP-HPLC	human blood serum	HPLC-UV	2.7 × 10^3–8.3 × 10^6 nM	3390 nM	[60]
	LC-IDMS	human blood serum	LC-IDMS	3.7 × 10^6–6.25 × 10^6 nM	44 nM	[153]
H_2S	PEC-sensor	PBS/human blood serum	Photocurrent measurement	1 × 10^3–5 × 10^6 nM	58 nM	[154]
	HPLC-MS/MS	human blood serum	AB SCIEX Triple Quad 4500+	7.8 × 10^2–1 × 10^5 nM	230 nM	[155]
	HS-GC-FPD	human blood serum	Agilent 7890B	2.9 × 10^3–1.2 × 10^5 nM	1468 nM	[156]
H_2O_2	PEC-sensor	N_2-saturated Tris-HCl buffer	Electrochemical system	1 × 10^4–7 × 10^6 nM	1050 nM	[157]
	HPLC-DAD	food samples	Agilent 1260 Infinity	1.4 × 10^4–2.9 × 10^6 nM	8823 nM	[158]
	GC-MS	milk and coffee	Agilent 7890/5975 N	1.4 × 10^2–1.4 × 10^6 nM	58.8 nM	[159]
Kanamycin	PEC-sensor	0.1 M Na_2SO_4 buffer	Electrochemical system	1 × 10^0–2.3 × 10^2 nM	0.2 nM	[160]
	RP-HPLC-UV	Kanamycin sulfate	HPLC system	5.1 × 10^5–4.0 × 10^6 nM	78,000 nM	[144]
	LC/MS	Luria-Bertani broth	UHPLC/Q-Exactive MS	2.1 × 10^4–4.1 × 10^5 nM	5160 nM	[145]
	ELISA	Milk and Honey	LC-MS/MS triple quadruple MS	6.1 × 10^{-1}–6.1 × 10^1 nM	0.14 nM	[161]
	ELISA	Milk	ELx800, BioTek	1.0 × 10^{-1}–6.5 × 10^2 nM	0.02 nM	[162]
Chlorpyrifos	PEC	0.1 M PBS buffer	Electrochemical system	8.5 × 10^{-2}–2.8 × 10^2 nM	0.028 nM	[163]
	GC	cinnamon and green pepper	Agilent 7890A GC	7.1 × 10^{-1}–7.1 × 10^1 nM	0.1 nM	[164]

In comparing enzyme-free and enzyme-based aptasensors, stability metrics—including storage stability, cycling stability, temperature tolerance, and applicability in complex matrices were evaluated (Table 7). Enzyme-free systems demonstrate exceptional long-term stability under ambient conditions. For example, mesoporous $BiVO_4$ films retain 98% of their photoactivity after 6 months of storage at 25 °C and show no significant degradation after 90 cycles. This stability arises from the high crystallinity and thermodynamic stability of inorganic nanomaterials, which resist denaturation, pH-induced inactivation, or conformational changes that commonly affect enzyme proteins during storage [165]. In contrast, enzyme-based systems exhibit condition-dependent stability. The GDH enzyme sensor retained only 81.37% of its activity after 20 days of storage. Although the RC-LH1 photoprotein bioelectrode achieves over 2 years of storage stability under strict refrigeration (4 °C), its sensitivity to temperature limits practical application under ambient conditions. Furthermore, the reusability of enzyme-based systems is substantially lower than that of enzyme-free systems [166,167].

Table 7. Performance comparison of enzyme-based and enzyme-free PEC aptasensors.

System Type	Material	Storage Conditions	Storage Stability	Cycling Stability	Ref.
Enzyme-Free System	Mesoporous $BiVO_4$ film	Ambient conditions (~25 °C)	Retains 98% photoactivity after 6 months	Retains 93% after 90 cycles/90 days	[165]
	TiO_2 nanorod array	/	Simple preparation, easy storage	Reusable with good stability	[168]
	AuNPs/$BiVO_4$	/	Good stability	Good reproducibility	[169]
Enzyme-Based System	GDH-TiO_2NFs-rGO	/	81.37% (after 20 days)	Reproducible after 7 uses	[166]
	RC-LH1 photoprotein bioelectrode	Dark/refrigerated (4° C)	2 years (operational stability after storage)	Continuous illumination for 33 days	[167]

4.3. Practical Deployment Limitations: Cost, Portability, and Usability

Despite their outstanding advantages, PEC sensors face several critical challenges in commercial application. Insufficient selectivity remains a key bottleneck, particularly in complex gaseous or liquid environments where cross-responses to multiple substances may occur. Performance is also highly sensitive to environmental humidity, as fluctuations can significantly affect photogenerated charge carrier behavior and the stability of analytical results.

Additionally, prolonged illumination and reactive oxygen species generated during reactions can lead to chemical degradation of photoactive materials, compromising long-term stability. From a manufacturing perspective, fabricating high-performance PEC sensors often involves complex synthesis and modification of nanomaterials, posing challenges for consistency and cost control in large-scale production.

Equipment requirements for sensors vary by transduction mechanism. (i) Optically transduced sensors (e.g., fluorescence, SERS) require laboratory-grade instruments such as fluorescence spectrometers (¥50,000–300,000/system) and Raman spectrometers (¥250,000–600,000/system), which are large, power-intensive, and unsuitable for on-site detection. For example, C_3N_4/MXene-AuNPs-based SERS PEC sensors rely on confocal Raman spectrometers, restricting their use to laboratory settings [170]. (ii) Electrochemically transduced PEC sensors utilize electrochemical workstations (¥25,000–100,000/system) that are compact and energy-efficient, making them well-suited for field deployment. A CdS-Au/ITO-based electrochemical PEC aptasensor with a portable workstation (3.5 kg) was successfully used for on-site E. coli detection in rivers [171]. (iii) Emerging formats such as paper-based PEC sensors [172] can integrate with portable readout devices like smartphone-based readers, further reducing equipment demands and enabling rapid testing in remote areas [137,173]. In contrast, conventional methods (e.g., LC-MS, HPLC) rely on large-scale laboratory equipment unsuitable for field use. Outdoor analysis is also challenged by operational complexity and anti-interference capabilities. PEC sensors feature straightforward workflows, requiring only sample addition, incubation, and signal acquisition—that can be mastered by non-specialists after minimal training. Conversely, optical sensors such as SERS involve complex procedures requiring specialized personnel for optical alignment and signal interpretation, limiting their widespread adoption.

At the application level, PEC sensors have shown significant promise, particularly in biomedicine, where several breakthrough studies highlight their potential in cancer therapy. Qiu et al. developed a smart near-infrared (NIR) light-controlled drug release system using black phosphorus nanosheets integrated into a biodegradable thermosensitive hydrogel. Leveraging the photothermal effect of black phosphorus under NIR irradiation, they achieved controlled drug release that eradicated subcutaneous breast cancer and melanoma, with the material degrading into non-toxic products post-treatment [174]. Building on this, Xie et al. combined black phosphorus-based photothermal therapy with aCD47-mediated immune checkpoint blockade. The photothermal ablation directly destroyed tumor cells while enhancing tumor immunogenicity, synergizing with aCD47 to activate innate and adaptive immunity, thereby inhibiting tumor progression and metastasis [175]. Additionally, Chen et al. addressed the challenge of tumor targeting by constructing a photothermal selenium-coated tellurium nanoheterojunction (TeSe). This heterojunction exhibited excellent stability and biosafety, enabling near-complete eradication of lung cancer and hepatocellular carcinoma under NIR irradiation while remodeling the tumor microenvironment and inducing cancer cell apoptosis [176]. These studies expand the application boundaries of 2D materials in biomedicine and provide valuable insights into material design and biocompatibility for photoelectric-based disease marker detection.

Despite their advantages, PEC sensors face several critical challenges in commercial application. Insufficient selectivity remains a major bottleneck, particularly in complex environments where cross-responses to multiple substances can occur. Performance is also highly sensitive to humidity fluctuations, which affect photogenerated charge carrier behavior and result stability. Additionally, prolonged illumination and reactive oxygen species generation may cause chemical degradation of photoactive materials, compromising long-term stability. From a manufacturing perspective, the complex synthesis and modification processes required for high-performance PEC sensors pose challenges for consistency and cost control in large-scale production. Looking ahead, future development will focus on visible-light-responsive materials, self-powered sensing systems, and integration with artificial intelligence for intelligent data interpretation and enhanced environmental adaptability.

5. PEC Cell Using 2D Nanomaterial

PEC technology, which couples the light absorption of semiconductor photoelectrodes with electrocatalytic reaction processes to achieve the direct conversion of solar energy into chemical energy, stands as a core technical pathway for addressing global energy crises and environmental challenges. As the central reaction unit of a PEC system, the design of the electrochemical cell directly determines the interfacial contact between the photoelectrode and the electrolyte, charge transport efficiency, mass transfer characteristics, and reaction stability, thereby influencing the overall photoelectrochemical conversion efficiency and scalability potential of the entire system. Currently, the predominant cell types in the PEC field include H-type cells, flow cells, and membrane electrode assembly (MEA) cells, each with distinct features in structural design, working principles, and application scenarios. Taking CO_2 RR as an example, Figure 18a–c illustrates the structural composition of these three types of electrolyzers [131], where the corresponding PEC electrolyzer requires the addition of an illuminated

quartz window to meet the efficient light absorption needs of the photoelectrode. This article will provide a systematic elaboration from the aspects of working principles, core advantages and disadvantages, typical application scenarios, latest developments, and future trends. Combined with the application demands of advanced photoelectrode systems such as 2D materials, it aims to offer comprehensive references for the structural optimization and industrial-scale advancement of PEC cells. Table 8 provides a detailed list of the electrolytic cells commonly used for 2D materials in PEC reactions, along with specific use cases for each.

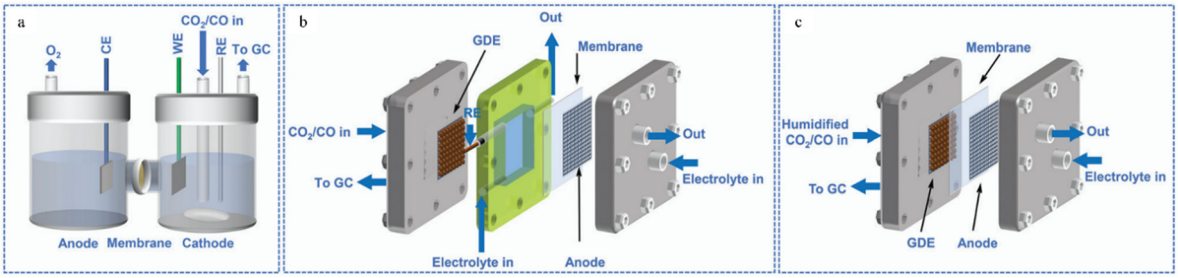

Figure 18. Schematic illustration of three types of electrocatalytic reactors, (**a**) H-cell, (**b**) Flow cell and (**c**) MEA. (**a**–**c**) Reprinted/adapted with permission from Ref. [131]. Copyright 2021, Royal Society of Chemistry.

Table 8. Elaboration on the specific applications of three types of electrolytic cells in photoelectrocatalysis.

Electrolyzer Type	Reaction System	Electrolyte Composition	Applied Potential	Photoelectrode	Ref.
H-Cell	PEC water oxidation to H_2O_2	0.5 M $NaHCO_3$ (pH = 8.27 ± 0.01) to generate H_2O_2; 0.5 M PBS (pH = 8.32 ± 0.02) to generate O_2	~0.4–2.0 V_{RHE}	Photoanode: $BiVO_4$	[177]
	PEC water splitting	1.0 M K_3BO_3(pH = 9.0) for both anode and cathode	1.23 V	Photoanode: BiVO/NiFe-LDH/ $Co_3Ge_2O_5(OH)_4$	[7]
	PEC urea oxidation reaction	0.33 M urea + 0.1 M Na_2HPO_4 + 0.1 M NaH_2PO_4 for both anode and cathode	0 V	Photoanode: $BiVO_4$/2.5%Bi:NiO/Co-Ci	[29]
	Chiral molecular sensing and analysis	0.05 M I_2, 0.5 M LiI, 0.1 M 4-tert-butylpyridine for both anode and cathode	0.5 V	Photoanode: N719/ PtNC/L-TCN	[178]
Flow Cell	PEC CO_2 capture and release	Anolyte: 0.4 M ($K_4[Fe(CN)_6]$) Catholyte: 0.06 M $C_{14}H_6O_8S_2^{2-}$ in 0.5 M KCl	0 V	Photoanode: F-SnO_2/$BiVO_4$ Cathode: graphite felt	[177]
	PEC Glycerol Oxidation and CO_2 Reduction Reaction	Anolyte: 1.0 M CsOH + 0.5 M Glycerol Cathode side: CO_2 flow of 25 cm^3 min^{-1}	1.0 $V_{Ag/AgCl}$	Photoanode: Ni NPs/Si	[179]
	PEC oxidation of methane	0.1 M Na_2SO_4 (PH 2) for both anode and cathode	0.75 V_{RHE}	Photoanode: TiO_2/$ZnWO_4$	[180]
	Solar photocharging reaction	Anolyte: 50 mM TEMPOL + 1.0 M NaCl Catholyte: 50 mM AQDS + 1.0 M NaCl	−0.07 V_{SHE}	Photoanode: a-Si/C	[35]
MEA Cell	PEC water splitting	All-solid-state polymer electrolyte membrane	1.23 V_{RHE}	Photoanode: TNTAs/Ti-web	[181]
	PEC oxidation of organics	0.2 M KOH with 10% ethanol for both anode and cathode	1.09 V_{OCV}	Photoanode: CdS-ZnS-TiO_2/SBA-15	[182]
	PEC water splitting	Anolyte: 0.1 M Na_2S Catholyte: 0.1 M Na_2SO_4	/	Photoanode: TNA-CdS	[183]
	PEC water splitting	0.5 M H_3BO_3 adjusted by 1 M KOH (pH 9.5) for both anode and cathode	1.2 V	Photoanode: Mo/$BiVO_4$/$NiFeO_x$	[184]

5.1. H-Type Electrochemical Cell

The H-type cell is the most classic and fundamental electrochemical cell in the PEC field, composed of two isolated reaction chambers (anodic and cathodic compartments), an ion exchange membrane (or salt bridge), a light-transparent window, and sealing components. The two chambers are respectively equipped with a photoelectrode (e.g., TiO_2, BiOX, LDHs, $SrTiO_3$ [185] based 2D composite materials) and a counter electrode (e.g., a Pt sheet or a carbon nanotube array). An ion exchange membrane, commonly a Nafion proton exchange membrane, an anion exchange membrane, or a porous ceramic membrane, is used to enable ion conduction and separate H_2/O_2 products, thereby avoiding cross-contamination and safety hazards [186]. The electrolyte system can be flexibly chosen from aqueous solutions (e.g., 0.5 M Na_2SO_4 [187–189], 1 M KOH [190–192]), non-aqueous solutions (e.g., acetonitrile-water [193], dichloromethane-water mixed systems [192]) or ionic liquids [193], to accommodate the stability requirements of different photoelectrode materials. The ion exchange membrane allows directional migration of electrolyte ions (such as H^+, SO_4^{2-}, OH^-) to maintain electrical neutrality in both chambers and ensure the continuous

progression of the reaction. A salt bridge is primarily employed in low-ionic-strength electrolyte systems, through whose gel matrix electrolyte ions migrate to achieve charge balance and migrate the resistance to ion conduction.

The core advantages of the H-type cell are reflected in its simple structure, low cost, and operational flexibility. Its fabrication requires no complex machining or specialized sealing techniques, as the reaction chambers can be made from common glassware. The ion exchange membrane and electrodes are readily replaceable, enabling rapid adaptation to the screening of diverse photoelectrode materials, electrolyte systems, and reaction conditions (e.g., pH, temperature). Moreover, its dual-compartment separation design effectively prevents contact between oxidation and reduction products, avoiding undesirable reverse reactions. It also facilitates independent control and in-situ characterization of the reactions at both electrodes, providing an ideal platform for mechanistic investigation. The limitations primarily stem from intrinsic structural constraints, leading to issues such as low mass transfer efficiency and significant charge loss. First, in static or low-flow electrolyte systems, reaction products tend to adsorb and accumulate on the electrode surface, while reactants struggle to diffuse rapidly to active sites, resulting in pronounced concentration polarization. Second, the permeability, ion selectivity, and long-term stability of ion exchange membranes are often insufficient, and salt bridges suffer from slow ion conduction rates; both factors increase interfacial charge transfer resistance and reduce charge separation efficiency. Third, the sealing capability is limited, making electrolyte leakage during long-term operation a common issue, which compromises measurement accuracy and reproducibility.

Currently, H-type electrolytic cells are primarily suitable for laboratory-scale fundamental research, serving in scenarios such as activity screening and modification effect evaluation of new photoelectrode materials, investigation of PEC reaction mechanisms, optimization of electrolyte systems, and determination of kinetic parameters. For example, an H-type electrolyzer was successfully employed in a PEC system to facilitate the splitting of hydrogen sulfide into hydrogen and sulfur (Figure 19) [194]. This design allows the half-reactions to proceed in separate compartments, thereby minimizing cross-contamination and improving reactant/product management. Additionally, Guan et al. optimized carrier behavior kinetics by introducing NiFe-LDH and $Co_3Ge_2O_5(OH)_4$ on $BiVO_4$, and the H-type cell enabled rapid comparison of the effects of different cocatalyst loadings on photoelectric conversion efficiency [7]. Simultaneously, in the study on the mechanism of PEC water oxidation to generate H_2O_2, Li et al. revealed the kinetic essence of electrolyte regulation on the selectivity of water oxidation at the photoanode by independently adjusting the electrolyte composition in the anode chamber of an H-type electrolytic cell [177]. To address the core limitations of H-type electrolytic cells, researchers have achieved performance enhancement strategies via auxiliary functions: in terms of mass transfer enhancement, approaches introducing magnetic stirring [195,196], ultrasonic assistance [197,198], applying pressure to promote gas molecule dissolution [199] and nanobubble injection into the electrolyte to enhance diffusion have been employed.

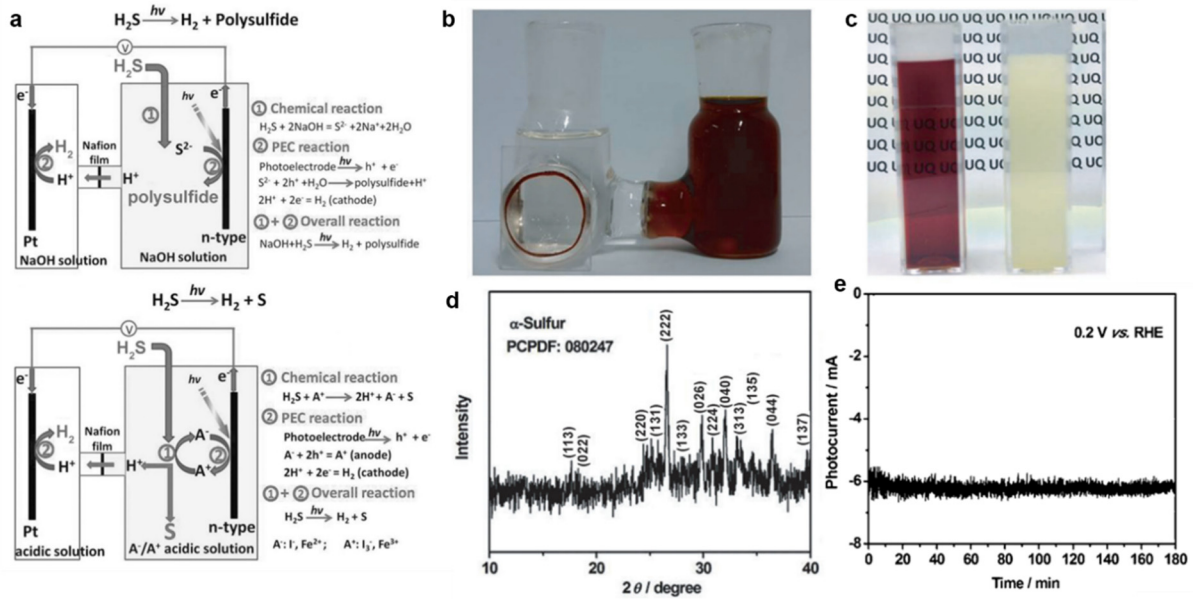

Figure 19. Diagram of the Application of Model H Electrolyzer in Practical PEC H_2S Decomposition for Hydrogen Production, (**a**) Mechanism of the PEC H_2S Decomposition, (**b**,**c**) Photographs of the H-type Electrolyzer setup, (**d**) XRD pattern of the Obtained α-sulfur and (**e**) Chronoamperometry Curve [194]. (**a**–**e**) Reprinted/adapted with permission from Ref. [194]. Copyright 2014, John Wiley and Sons.

5.2. Flow Electrolytic Cell

Flow-type electrolytic cells are designed based on the concept of enhanced mass transfer, optimizing material transport at the electrode surface and interfacial reaction kinetics by constructing a continuously flowing electrolyte system. Their core structure includes a reaction chamber (typically made of quartz, PTFE (polytetrafluoroethylene), or stainless steel), a light-transmitting window (quartz glass or transparent polymer film), an electrode fixation device, inlet/outlet ports, and a fluid driving system (such as a peristaltic pump or high-pressure injection pump). The electrolyte continuously flows through the reaction chamber at a certain flow rate (typically 1–50 mL/min) via the fluid driving system [200,201], ensuring full contact with the photoelectrode surface: fresh electrolyte is continuously supplied to active sites, while reaction products are rapidly carried away by the fluid, significantly mitigating concentration polarization. Some flow-type electrolytic cells optimize flow path design (such as S-shaped flow channels, spiral flow channels [202]) to achieve product separation and increase the number of electrodes to shorten the mass transfer distance [203]. Furthermore, some designs integrate temperature control systems and pressure regulation devices, allowing experiments to be conducted under a wide range of temperature and pressure conditions (e.g., 25–80 °C, 20–50 bar) [204–206], thereby further enhancing reaction activity.

The core advantages of flow electrolytic cells include their high mass transfer efficiency, excellent stability, and good scalability. The continuously flowing electrolyte system effectively addresses issues prevalent in H-type cells, such as product accumulation and pronounced concentration polarization, while also offering substantially superior structural compactness. Furthermore, by adjusting parameters such as fluid flow rate, pressure, and temperature, reaction conditions can be flexibly controlled to meet the application requirements of different types of photoelectrode materials. This design also facilitates long-term stability testing, enabling continuous operation for over 1000 h [207]. However, flow electrolytic cells also present certain limitations. First, their structural complexity and cost are higher than those of H-type cells, as they require additional components such as a fluid driving system, sealing devices, and specialized flow channel machining. Maintaining stable fluid flow during operation also leads to increased energy consumption, the fluid shear stress poses a challenge to electrode stability, excessively high flow rates may cause the delamination of 2D thin-film photoelectrodes from their substrates, particularly affecting materials with weaker mechanical strength, such as those derived from MOFs/COFs [208,209]. Besides, improper flow channel design can easily lead to uneven fluid distribution, creating local mass transfer dead zones that compromise overall performance.

Flow electrolytic cells are suitable for pilot-scale research on PEC hydrogen production, long-term stability testing of photoelectrodes, and mechanistic investigation into the coupling of mass transfer and reaction process. For example, Anáky et al. designed a membrane-isolated continuous-flow PEC reactor that achieved paired reactions of CO_2 reduction and glycerol oxidation (Figure 20a). Under 10-sun concentrated illumination, the photocurrent density exceeded 110 mA cm^{-2}. The membrane separation design effectively isolated the cathodic and anodic reactions, suppressed side reactions, and thereby maintained system stability at high current densities [179]. Furthermore, these systems hold broad application prospects in the development of continuous PEC hydrogen production devices and the evaluation of scaled-up photoelectrode fabrication. For instance, Abdi et al. designed and constructed a high-pressure flow-type PEC water splitting experimental setup. This study operated a dual-photoelectrode electrolysis cell comprising a series-connected $BiVO_4$ photoanode and a $Pt/GaInP_2$ photocathode at a high pressure of 20 bar, achieving a solar-to-hydrogen conversion efficiency exceeding 20% (Figure 20b) [210]. Shan et al. utilized a scaled-up photoelectrode (25 cm^2) to generate a photocurrent of 398 mA under simulated sunlight, with an external quantum efficiency of 33.7% (Figure 20c). Compared to a standard-sized photoelectrode (1.0 cm^2), the efficiency loss was less than 1% [211]. Furthermore, a self-powered PEC tandem device featuring an S-shaped flow channel was designed for toluene PEC oxidation (Figure 20d). In this system, toluene and water are pre-mixed and then pumped into the reactor. Through the two-phase interface formed between the flowing reactants and the catalyst surface, long-term continuous conversion of toluene is achieved (Figure 20e) [212].

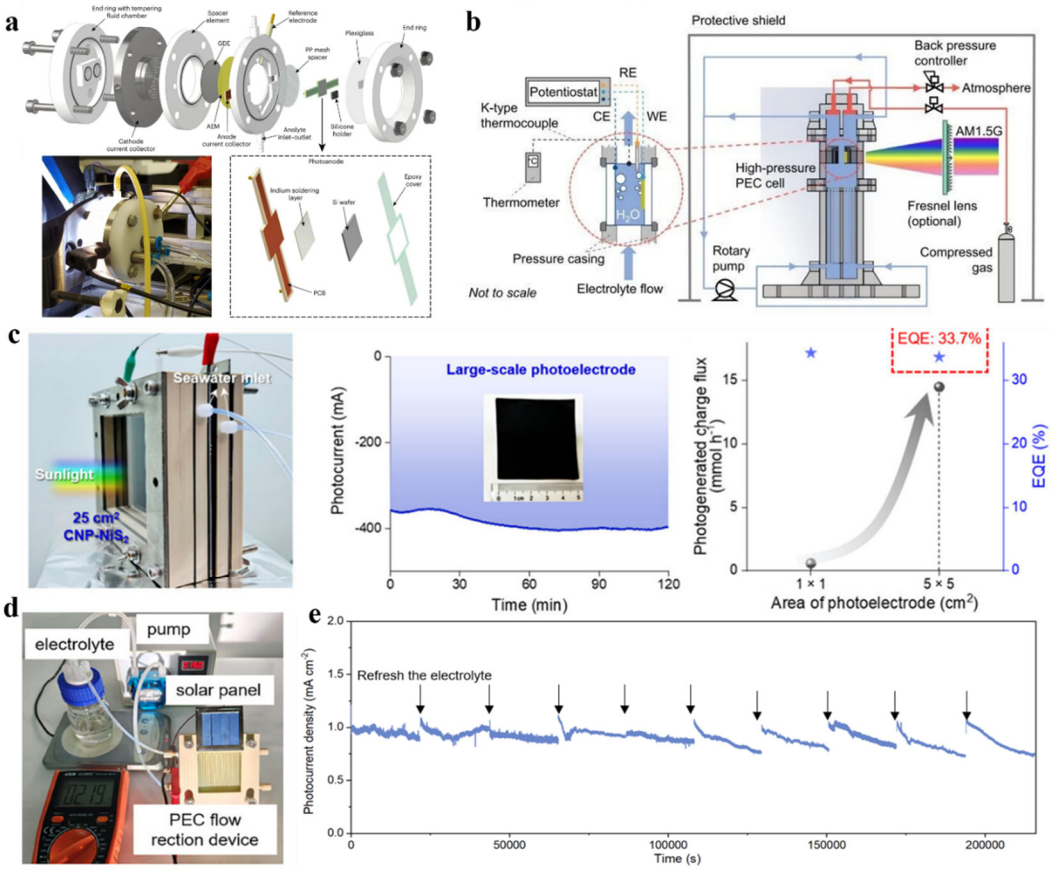

Figure 20. Different Designs and Applications of Flow PEC Electrolyzer, (**a**) Membrane-separated Continuous-flow PEC Electrolyzer [179]. (**b**) Dual-photoelectrode Continuous PEC Electrolyzer [210]. (**c**) Large-scale PEC Electrolyzer, reprinted/adapted with permission from Ref. [211]. Copyright 2025, American Chemical Society. (**d**,**e**) Flow Electrolyzer for Toluene PEC Oxidation, reprinted/adapted with permission from Ref. [212]. Copyright 2025, John Wiley and Sons.

5.3. Membrane Electrode Assembly Cell

The Membrane Electrode Assembly (MEA) cell represents the most highly integrated type of PEC electrolyzer. Its structural design draws on the core concept of proton exchange membrane fuel cells (PEMFCs), featuring a sandwiched, integrated "photoanode-PEM-cathode" structure composed of a photoanode, a proton exchange membrane (PEM), a cathode, and sealing components. The photoanode and cathode are coated onto opposite sides of the PEM, forming an intimate contact interface. This design eliminates the need for separate reaction chambers and large volumes of liquid electrolyte, as the PEM itself serves the dual functions of electrolyte and product separation [213].

The electrolyte system typically consists of a solid or quasi-solid proton-conducting medium. For instance, the sulfonic acid groups within a Nafion membrane provide proton transport channels. Some studies employ novel proton exchange membranes such as sulfonated polyimide or MOF composite membranes to enhance high-temperature stability and proton conductivity. Under illumination, photogenerated holes at the photoanode oxidize water to produce O_2 and H^+. The H^+ ions migrate rapidly through the sulfonic acid groups in the PEM to the cathode surface, where they combine with photogenerated electrons to form H_2. Some MEA cells use an anion exchange membrane (AEM) instead of a PEM to accommodate photoelectrode materials stable under alkaline conditions. In this configuration, H^+ forms OH^- via hydration for directional migration, further expanding the range of material choices [214,215].

The membrane electrode assembly (MEA) cell boasts prominent advantages across three core aspects: high integration, high efficiency, and high stability. First, its compact structure facilitates scalable stacking and assembly, laying the groundwork for large-scale application. Second, the proton exchange membrane offers high ionic conductivity, significantly reducing interfacial charge transfer resistance. Third, it eliminates the need for large volumes of liquid electrolyte, thereby reducing electrolyte consumption and waste-liquid disposal issues. Furthermore, the excellent hermetic sealing performance and intimate contact between electrodes and membrane effectively suppress the detachment of active components and electrode corrosion, thus ensuring long-term stable

operation of the cell. The main drawbacks focus on the complex fabrication process, high cost, and stringent material compatibility requirements: (I) The preparation of membrane-electrode assemblies demands strict control over process parameters; steps such as coating, calcination, and hot-pressing of the photoanode and cathode onto the proton exchange membrane require precise management—otherwise, poor interfacial contact may occur, increasing charge-transfer resistance. (II) Proton exchange membranes (e.g., Nafion) are relatively expensive, and the performance of novel membrane materials still needs improvement. (III) The light-utilization efficiency of the photoanode is constrained by the MEA structure; if the photoanode coating is too thick, it can impair both light-absorption and mass-transfer efficiency [216,217]. (IV) The stability of the proton exchange membrane is significantly affected by reaction conditions. under high-current or strongly oxidative environments, catalysts are prone to detachment [218].

The MEA cell is the type of of electrolyzer closest to industrial application and is suitable for large-scale 2D (photo)electrocatalytic material applications. To reduce the system energy consumption and complexity of photoelectrochemical water splitting, developing integrated systems that operate without an external power supply is a key direction. An early pioneering work, drawing on fuel cell configuration, was conducted by Seger et al. They constructed a TiO_2/Nafion/Pt membrane electrode assembly (Figure 21a), which successfully achieved continuous light-driven hydrogen production without applying any external bias, providing an important conceptual foundation for subsequent designs of bias-free PEC cells [219]. Similarly, Domen et al. constructed a PEC cell comprising a Pt/C-based membrane electrode assembly and a $SrTiO_3$ photoanode for the efficient conversion of toluene and water into methylcyclohexane. This MEA system, operating without external bias for the hydrogenation of pure toluene, achieved 83% Faradaic efficiency and 18% incident photon-to-current conversion efficiency, successfully demonstrating a pathway for producing high-concentration methylcyclohexane as a hydrogen carrier [220]. Regarding toluene mineralization via PEC, Zhang et al. designed a Janus-type photoelectrode based on titanium foam and constructed a membrane electrode assembly for efficient treatment of gaseous pollutants. This electrode employs a unique double-sided structure: one side serves as the light-absorbing and photocatalytic surface, while the other is dedicated to electrocatalytic reactions. This Janus design drives photogenerated electrons and holes to migrate in opposite directions under an internal electric field, achieving efficient spatial charge separation, thereby enabling the direct and efficient mineralization of gaseous toluene within the MEA (Figure 21b). Benefiting from this photoelectric synergistic mechanism, the photoelectrochemical system's degradation efficiency for toluene was enhanced by 4.6 times and 8.5 times compared to individual photocatalysis and electrocatalysis processes, respectively [214]. Toward high-efficiency hydrogen generation, Amal et al. constructed a compact, liquid-electrolyte-free electrolyzer by integrating a $BiVO_4$ photoanode with a MEA, which utilizes the MEA architecture to markedly reduce ohmic losses and enable in-situ hydrogen separation (Figure 21c). Moreover, through optimization of the electrode–membrane interface and mass transport pathways, the work addresses key challenges in charge separation and transport for $BiVO_4$ in constrained reaction environments, offering a novel strategy for continuous and efficient photoelectrochemical synthesis (Figure 21d) [184].

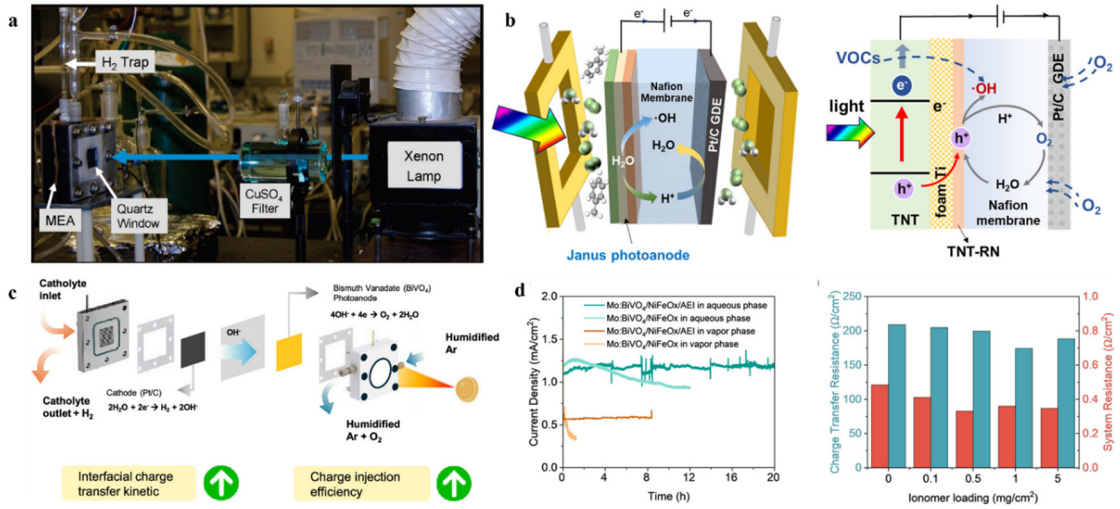

Figure 21. Different Designs and Applications of MEA cell in PEC Reactions, (**a**) TiO_2 photoanode || Pt cathode [219]. Reprinted/adapted with permission from Ref. [219]. Copyright 2009, American Chemical Society. (**b**) Janus photoanode || Pt/C cathode. Reprinted/adapted with permission from Ref. [214]. Copyright 2025, American Chemical Society. (**c,d**) Mo/$BiVO_4$/$NiFeO_x$ photoanode || Pt/C cathode. Reprinted/adapted with permission from Ref. [184]. Copyright 2025, American Chemical Society.

The MEA cell is the type H-type, flow-type, and MEA electrolytic cells act as the core reaction modules for PEC technology, tailored to the distinct demands of fundamental research, pilot-scale trials, and industrial applications, respectively. The H-type electrolyzer, endowed with intrinsic operational flexibility, stands as an ideal platform for material screening and reaction mechanism investigations. The flow-type electrolytic cells strike a favorable balance between reaction efficiency and system stability by boosting mass transfer kinetics at the electrode-electrolyte interface. In the meantime, the MEA electrolytic cells spearheads the industrialization development of PEC technology by virtue of its high integration and exceptional energy conversion efficiency. Looking ahead, driven by sustained technological breakthroughs in 2D materials, advanced membrane materials, and intelligent control systems, PEC electrolytic cells are set to realize pivotal advancements in structural optimization, cost reduction, and large-scale deployment. Such progress will furnish the hydrogen energy industry with core technological support and further underpin the achievement of energy transition and the advancement of dual carbon goals.

6. Integration Progress of PEC Technology with Emerging Technologies

6.1. AI-Assisted Catalytic Reactions

Artificial intelligence (AI), encompassing machine learning, deep learning, natural language processing and computer vision, aims to achieve intelligent decision-making and behavior akin to humans. In the field of PEC, AI technology facilitates real-time monitoring, dynamic optimization and intelligent regulation of catalytic processes through tools such as intelligent decision-making systems and digital twin models.

In the development, screening, and design of photoelectrocatalysts, AI-powered generative models provide innovative approaches for designing novel catalysts. Moving beyond traditional methods that rely on known elements and structures, models like Generative Adversarial Networks (GANs) can autonomously propose new catalyst architectures and predict their performance. For instance, Li et al. innovatively developed a deep learning model optimized based on the MatterGen framework, combined with DFT calculations, to accurately screen efficient metal oxide catalysts within a bandgap range of 1.1–1.4 eV. Their workflow for screening X-Ti-O series catalysts identified target candidates from 1206 generated materials, thereby providing precisely targeted options for subsequent experimental validation [207]. Liu et al. focused on the long-standing industry pain point of chlorine production relying on precious metal electrodes. Addressing the major scientific challenge of low activity, poor stability, and the lack of a theoretical basis for the design of non-precious metal CER catalysts, they constructed an AI design framework combining DFT and machine learning. This framework enabled rapid screening of hundreds of thousands of multi-element combinations, breaking through the bottleneck of traditional empirical catalyst development. It successfully identified Cu as the core active site and the critical role of high-entropy structures in optimizing electronic structure, adsorption energy barriers, and lattice stability. Based on theoretical predictions, the authors successfully synthesized a ten-element high-entropy MSb_2O_6, revealing that the high entropy leads to lattice distortion enhancement, with performance comprehensively surpassing most non-precious and even precious metal catalysts [221]. Regarding reaction system optimization, AI's real-time regulation capability enables the dynamic optimization of photoelectrochemical reactions. Based on real-time data (such as temperature, pressure, reactant concentration, photocurrent, etc.) collected by sensors, AI systems can simulate the reaction process via digital twin models and dynamically adjust reaction parameters (such as applied bias, light intensity, electrolyte flow rate, etc.) to ensure the reaction consistently operates under optimal conditions. Abolhasani et al., by integrating AI and automation technology, designed an intelligentized laboratory (Fast-Cat) that enables rapid, efficient, and automated catalytic reactions. It can not only operate high-temperature, high-pressure, and gas-liquid reactions completely autonomously and continuously but also analyze the output of each reaction and determine the influence of different variables on each experimental result without human intervention. It can provide more information in just 5 days than traditional methods can in 6 months, offering new possibilities for chemical research and industrial production [222].

6.2. Carbon Footprint Assessment

In the development of catalysts and the design of reaction systems, carbon footprint assessment provides a basis for the green design of catalysts. Traditional catalytic processes have primarily focused on catalytic performance, often overlooking carbon emissions during preparation. By integrating carbon footprint technology, it is possible to evaluate carbon emissions in catalyst development and reaction system design, thereby selecting low-emission raw materials and processes. For example, Zhu et al. proposed a cascade electrolysis strategy that couples CO_2 electroreduction with the electrocarboxylation of in-situ generated C_2H_4, achieving the synthesis of succinic acid (SA; $C_4H_6O_4$) using CO_2 as the sole carbon source. The study found that the FeNi foam catalyst significantly enhances C_2H_4 adsorption capacity through Fe-Ni synergy, and the conversion of adsorbed C_2H_4 to

*C_2H_4COO is the rate-determining step. This strategy avoids gas separation processes, reduces production costs, and achieves a negative carbon emission of −0.174 kg CO_2/kg SA [223]. Zhu et al. proposed a novel catalytic cycle based on the reversible conversion of γ-butyrolactone (GBL) and 1,4-butanediol (BDO), utilizing a Cu/Al_2O_3 catalyst to directly enable efficient separation, purification, storage, and transportation of crude hydrogen. This system can selectively capture and release hydrogen at 170 °C, exhibits high tolerance to impurities like CO, requires no precious metals or high-cost separation equipment, breaks through the technical bottlenecks of existing Liquid Organic Hydrogen Carrier (LOHC) and hydrogen purification technologies, and opens a new path for the large-scale utilization of industrial by-product and crude hydrogen. Carbon footprint assessment indicates that using green electricity can reduce the system's carbon emissions to 0.19 kg CO_2-eq/kg H_2, demonstrating significant green and low-carbon potential [214]. Carbon footprint assessment is not merely a post-hoc environmental reporting tool but serves as a forward-looking green design guide. It prompts researchers to consider "low-carbon" as a core design objective alongside "high efficiency" and "high selectivity" from the initial conception of a new catalytic system. By optimizing carbon efficiency across the entire chain—from catalyst molecular design to reaction system integration—catalysis science is providing the key technological core for achieving substantial emission reduction and sustainable development goals in the chemical industry.

6.3. In-Situ Resource Utilization (ISRU) Technology in Space

In-Situ Resource Utilization (ISRU) technology has been considered as a pivotal approach to produce fuels and chemicals for human space exploration beyond earth [224]. Recently, the PEC technology has been accessed for water-splitting on moon and carbon dioxide reduction reactions (CO_2RR) on Mars to produce hydrogen (H_2), oxygen (O_2) and a variety of carbon-based fuels such as methane (CH_4), which can serve as rocket propulsions (e.g., LO_X/LH_2 or LO_X/LCH_4) for deep space explore missions. Ideal solar-to-hydrogen (STH) conversion efficiency ~38.1% on Moon as well as solar-to-chemical (STC, product CH_4) ~9.54% on Mar are evaluated [225]. To improve the adaptability to extraterrestrial environments of the PEC technology, water-splitting devices have been demonstrated in simulated microgravity [226] and low temperature environments [227]. Moreover, PEC driven CO_2 reduction experiments have been carried out in extraterrestrial artificial photosynthetic (EAP) system on China Space Station (https://www.cmse.gov.cn/xwzx/202601/t20260108_57194.html, accessed on 8 January 2026). Although remarkable improvements have been made through both terrestrial research and extraterrestrial tests, further studies are required to focus on modifying catalysts and devices to adapt to the harsh extraterrestrial environments, optimizing mass transport to overcome the limitations of reduced gravity, and evaluating the actual solar-chemical production rates in large-scale systems.

In the development of photoelectrocatalysis, AI is driving a shift in research methodology from the traditional "trial-and-error-driven" approach toward "rational design", significantly accelerating the discovery and optimization processes through data mining and predictive modeling. Simultaneously, the introduction of carbon footprint assessment has transformed "greenness" from a qualitative concept into a quantifiable and optimizable core performance metric, promoting the systematic advancement of PEC research toward full life-cycle sustainability. The deep integration of these two types of technologies is collectively reshaping the research trajectory in the PEC field, shifting the focus from the pursuit of singular performance to systematic design and evaluation that balances efficiency, stability, and environmental impact.

7. Conclusions and Perspectives

In conclusion, photoelectrochemical (PEC) technology serves as a bridge connecting solar energy to chemical energy, demonstrating immense potential in addressing energy crises and environmental issues. This review has summarized the common layered semiconductor materials involved in this field—including metal oxides, chalcogenides (S/Se), C/N compounds, and LDHs—along with their classifications. Presently, many popular 2D materials, such as MXenes, face challenges due to their metallic nature, which prevents them from functioning effectively as primary charge generators. Consequently, they are typically employed as co-catalysts in PEC systems, primarily responsible for charge separation and transfer. Furthermore, semiconducting 2D materials—like TMDs, g-C_3N_4, and LDHs—can also be limited by unfavorable band positions, poor charge carrier mobility, and instability caused by photocorrosion or harsh electrochemical environments. In practice, multiple strategies have been applied to address these issues, including heterojunction engineering, elemental doping, defect engineering, and morphology control. As evidenced in the literature, significant efforts have been devoted to developing PEC materials with tailored properties using these approaches. In principle, all these strategies aim to tune the band structure of the catalytic system to suit specific reactions. Phenomena such as band structure formation, impurity states, defect states, and band alignment—resulting from the dimensions and thickness of 2D

materials—have been proven effective in numerous published studies. Simultaneously, some of the described strategies help increase surface active sites, thereby synergistically contributing to band structure tuning and enhancing PEC efficiency. The core objectives of these strategies are consistent: broadening the light absorption range, promoting the separation and transport of photogenerated charge carriers, and accelerating surface reaction kinetics. Moreover, we have explored the diverse applications of PEC in solar energy conversion—from classical water splitting for hydrogen production and CO_2 reduction to emerging organic synthesis and nitrogen fixation reactions—reflecting a technological shift from mere "energy storage" toward "value-added" chemical production.

The following section details various challenges and opportunities facing 2D materials in PEC reactions. Extensive experimental and theoretical studies have been conducted to enhance the PEC activity of 2D materials. Numerous 2D materials have already been applied in PEC processes such as water splitting and organic pollutant degradation. However, several fundamental aspects still need to be addressed to achieve optimal activity in target reactions. The large-scale practical application of PEC technology still faces challenges related to efficiency, stability, and cost. Future research should focus more on the following directions:

(I) Expanding Reaction Scope and Developing New Materials: Significant progress has been made using 2D materials in various PEC reactions such as the nitrogen reduction reaction (NRR), CO_2 reduction reaction (CO_2RR), oxygen reduction reaction (ORR), inorganic pollutant reduction, and alcohol oxidation. These reactions are garnering increasing attention, and a wider variety of 2D materials should be explored to identify suitable catalysts. This necessitates the development of novel, stable, and earth-abundant 2D semiconductor materials. While traditional optimization strategies and applications have made progress, they still face numerous bottlenecks. The integration of emerging technologies such as AI, machine learning, automation, and carbon footprint assessment with PEC offers novel solutions to overcome these challenges. Furthermore, attention must be paid to cost control and the scalable application of these integrated technologies to promote the widespread use of PEC in clean energy production, environmental management, and other fields, thereby providing core technical support for achieving carbon peaking and carbon neutrality goals.

(II) Enriching Material Library and Precise Structure Control: Considering that many materials with 2D structures have not yet been thoroughly investigated or applied in PEC, it is promising to expand the types of 2D materials used in this field. This can be achieved through synergistic multi-strategy approaches—such as constructing supported catalysts incorporating both defects and heterojunctions—for precise structural control. Realizing this goal will require the development of more synthesis methods;

(III) Deepening Mechanistic Understanding via Advanced Characterization and Theory: Utilizing advanced *in-situ* characterization techniques, combined with theoretical tools like density functional theory (DFT) calculations and molecular dynamics (MD) simulations, will provide deeper insights into the charge transfer processes and reaction mechanisms at the interfaces of 2D photocatalytic materials. This will help elucidate their dynamic evolution and underlying microscopic mechanisms;

(IV) Enhancing Efficiency and Device Durability: The long-term durability of PEC systems faces dual challenges. Current solar conversion efficiencies remain modest (typically 1–10%), and the fraction of light energy utilized in the PEC process itself is only ~10%, while the energy conversion efficiency can often exceed 50% upon electrocatalysis [228]. Commercialization urgently requires breakthroughs in efficiency. While 2D semiconductors like g-C_3N_4 and TMDs are ideal materials for H_2 production due to their broad spectral absorption and multiple exciton generation effects, their durability in electrochemical environments is significantly lower than in purely photocatalytic systems. Therefore, designing PEC reaction devices resistant to electrochemical corrosion is a critical issue that must be resolved. It is believed that with ongoing interdisciplinary integration and continuous innovation, PEC technology will play a vital role in the future green energy and chemical industries.

Two-dimensional materials show great potential in PEC, yet their practical application is limited by challenges in efficiency, stability, and cost. Future efforts should focus on expanding material libraries, deepening mechanistic insights through advanced characterization, and enhancing device durability. Integrating emerging technologies such as AI and automation with PEC systems will be key to advancing sustainable energy and environmental solutions.

Author Contributions

P.X.: Conceptualization, Methodology, Original Draft Writing & Editing; H.N., Y.H., Q.S. and Y.L. (Yang Li): Literature Review & Chart and Table Design & Data Verification; Y.S., X.-J.B., Y.-K.P., T.B., Y.L. (Yanli Liang) and D.F.: Writing—Review & Editing; C.Z.: Writing—Review & Supervision, Conceptual Advice; Y.Z.: Supervision, Funding Acquisition, Writing—Review & Editing. All authors have read and agreed to the published version of the manuscript.

Funding

This research was supported by the National Natural Science Foundation of China (22288102, 22438007), the China Space Station engineering aerospace technology test field project (2024HJS002) and the Joint Fund for Corporate Innovation and Development of the National Natural Science Foundation of China (U22B2071).

Conflicts of Interest

The authors declare no conflict of interest.

Use of AI and AI-Assisted Technologies

This manuscript was completed with the assistance of DeepSeek for partial literature research and enhancement of language readability. After using this tool, the authors have carefully reviewed and edited the content as needed and take full responsibility for the published material.

References

1. Chen, J.S.; Guan, C.; Gui, Y.; et al. Rational Design of Self-Supported Ni_3S_2 Nanosheets Array for Advanced Asymmetric Supercapacitor with a Superior Energy Density. *ACS Appl. Mater. Interfaces* **2017**, *9*, 496–504. https://doi.org/10.1021/acsami.6b14746.
2. Cho, K.G.; Kim, H.S.; Jang, S.S.; et al. Optimizing Electrochemically Active Surfaces of Carbonaceous Electrodes for Ionogel Based Supercapacitors. *Adv. Funct. Mater.* **2020**, *30*, 2002053. https://doi.org/10.1002/adfm.202002053.
3. Ren, J.; Shen, M.; Li, Z.; et al. Towards high-performance all-solid-state asymmetric supercapacitors: A hierarchical doughnut-like Ni_3S_2@PPy core−shell heterostructure on nickel foam electrode and density functional theory calculations. *J. Power Sources* **2021**, *501*, 230003. https://doi.org/10.1016/j.jpowsour.2021.230003.
4. Zhang, A.; Cai, Y.; Guo, L.; et al. Recent Progress in CO_2 Conversion: An Overview of Catalytic Strategies for Sustainable Fuel and Chemical Synthesis. *SmartMat* **2026**, *6*, e70058. https://doi.org/10.1002/smm2.70058.
5. Wang, S.N.; Zhang, R.; Ding, R.J.; et al. Intramolecular-locking modification enables efficient asymmetric donor-acceptor-donor′ type ultraviolet emitters for high-performance OLEDs with reduced efficiency roll-off and high color purity. *Chem. Sci.* **2025**, *16*, 5518–5527. https://doi.org/10.1039/d4sc08473j.
6. Feng, C.; Liu, Z.; Ju, H.X.; et al. Understanding the in-situ transformation of Cu_xO interlayers to increase the water splitting efficiency in NiO/n-Si photoanodes. *Nat. Commun.* **2024**, *15*, 6436. https://doi.org/10.1038/s41467-024-50893-x.
7. Chi, J.S.; Wei, Z.D.; Guo, W.Q.; et al. Enhanced Photoelectrochemical Water Splitting on $BiVO_4$ Photoanode via Efficient Hole Transport Layers of NiFe-LDH. *Acs Catal.* **2025**, *15*, 11293–11306. https://doi.org/10.1021/acscatal.5c02714.
8. Wan, W.R.; Meng, F.H.; Chen, S.; et al. Triazine-COF@Silicon nanowire mimicking plant leaf to enhance photoelectrocatalytic CO_2 reduction to C_{2+} chemicals. *Green Energy Environ.* **2025**, *10*, 422–432. https://doi.org/10.1016/j.gee.2024.04.007.
9. Zhao, Z.F.; Shen, X.Y.; Luo, X.Y.; et al. Electric Field Redistribution Triggered Surface Adsorption and Mass Transfer to Boost Electrocatalytic Glycerol Upgrading Coupled with Hydrogen Evolution. *Adv. Energy Mater.* **2024**, *14*, 2400851. https://doi.org/10.1002/aenm.202400851.
10. Luo, L.; Chen, W.S.; Xu, S.M.; et al. Selective Photoelectrocatalytic Glycerol Oxidation to Dihydroxyacetone via Enhanced Middle Hydroxyl Adsorption over a Bi_2O_3-Incorporated Catalyst. *J. Am. Chem. Soc.* **2022**, *144*, 7720–7730. https://doi.org/10.1021/jacs.2c00465.
11. An, Y.; Lei, T.; Jiang, W.Y.; et al. Research progress on photocatalytic, electrocatalytic and photoelectrocatalytic selective oxidation of 5-hydroxymethylfurfural. *Green Chem.* **2024**, *26*, 10739–10773. https://doi.org/10.1039/d4gc03597f.
12. Tang, D.B.; Liu, J.G.; Zhang, X.H.; et al. Sacrifice and valorization of biomass to realize energy exploitation and transformation in a photoelectrochemical way. *Green Chem.* **2023**, *25*, 7843–7862. https://doi.org/10.1039/d3gc01934a.
13. Singh, N.; Jabbour, G.; Schwingenschlögl, U. Optical and photocatalytic properties of two-dimensional MoS_2. *Eur. Phys. J. B* **2012**, *85*, 392. https://doi.org/10.1140/epjb/e2012-30449-7.
14. Li, Q.; Li, X.; Wageh, S.; et al. CdS/Graphene Nanocomposite Photocatalysts. *Adv. Energy Mater.* **2015**, *5*, 1500010. https://doi.org/10.1002/aenm.201500010.
15. Li, Y.G.; Li, Y.L.; Sa, B.S.; et al. Review of two-dimensional materials for photocatalytic water splitting from a theoretical perspective. *Catal. Sci. Technol.* **2017**, *7*, 545–559. https://doi.org/10.1039/c6cy02178f.
16. Kumar, P.; Boukherroub, R.; Shankar, K. Sunlight-driven water-splitting using two-dimensional carbon based semiconductors. *J. Mater. Chem. A* **2018**, *6*, 12876–12931. https://doi.org/10.1039/c8ta02061b.
17. Nayak, S.; Parida, K. Advancement of LDH-carbonaceous coupled structure towards promising water splitting and supercapacitor applications. *Adv. Colloid. Interfac.* **2025**, *346*, 103677. https://doi.org/10.1016/j.cis.2025.103677.
18. Liu, Z.H.; Chen, X.Y.; Zhao, Y.; et al. Constructing MO/TMDs heterostructures: Photoelectrochemical activity and

charge transfer mechanism investigation. *Chem. Eng. J.* **2025**, *511*, 161981. https://doi.org/10.1016/j.cej.2025.161981.
19. Fernández-Escamilla, H.N.; Paez-Ornelas, J.I.; Gutiérrez-Lazos, C.D.; et al. Bismuth and oxygen vacancies induce (2 × 1) reconstructions in bismuth oxyhalide (BiOX, X=Cl, Br, I) (001) surfaces. *Appl. Surf. Sci.* **2023**, *618*, 156583. https://doi.org/10.1016/j.apsusc.2023.156583.
20. Lim, K.R.G.; Shekhirev, M.; Wyatt, B.C.; et al. Fundamentals of MXene synthesis. *Nat. Synth.* **2022**, *1*, 601–614. https://doi.org/10.1038/s44160-022-00104-6.
21. Low, J.; Cheng, B.; Yu, J.; et al. Carbon-based two-dimensional layered materials for photocatalytic CO_2 reduction to solar fuels. *Energy Storage Mater.* **2016**, *3*, 24–35. https://doi.org/10.1016/j.ensm.2015.12.003.
22. Jain, C.; Kushwaha, R.; Rase, D.; et al. Tailoring COFs: Transforming Nonconducting 2D Layered COF into a Conducting Quasi-3D Architecture via Interlayer Knitting with Polypyrrole. *J. Am. Chem. Soc.* **2023**, *146*, 487–499. https://doi.org/10.1021/jacs.3c09937.
23. Zhu, X.Q.; Ke, T.; Zhou, J.Y.; et al. Vertex Strategy in Layered 2D MOFs: Simultaneous Improvement of Thermodynamics and Kinetics for Record C_2H_2/CO_2 Separation Performance. *J. Am. Chem. Soc.* **2023**, *145*, 9254–9263. https://doi.org/10.1021/jacs.3c01784.
24. Jie, K.C.; Zhou, Y.J.; Li, E.R.; et al. Nonporous Adaptive Crystals of Pillararenes. *Acc. Chem. Res.* **2018**, *51*, 2064–2072. https://doi.org/10.1021/acs.accounts.8b00255.
25. Marandi, M.; Torabi, N.; Farahani, F.A. Facile fabrication of well-performing CdS/CdSe quantum dot sensitized solar cells through a fast and effective formation of the CdSe nanocrystalline layer. *Sol. Energy* **2020**, *207*, 32–39. https://doi.org/10.1016/j.solener.2020.06.041.
26. Wang, Z.Y.; Xu, P.H.; Wang, W.J.; et al. Free radical-mediated glycerol selective upgrading to dihydroxyacetone over Au/$BiVO_4$ photoanodes at low bias. *Chem. Eng. J.* **2025**, *522*, 167841. https://doi.org/10.1016/j.cej.2025.167841.
27. Park, J.-H.; Kim, K.; Lee, J.; et al. Bias-Free Highly Efficient and Stable Dye-Sensitized Photoelectrochemical Cells via Cascade Charge Transfer. *Adv. Funct. Mater.* **2025**, e22757. https://doi.org/10.1002/adfm.202422757.
28. Zhu, Y.; Li, X.; Wen, Z.; et al. Highly Efficient Photoelectrochemical Alkene Epoxidation on a Dye-Sensitized Photoanode. *J. Am. Chem. Soc.* **2024**, *146*, 21903–21912. https://doi.org/10.1021/jacs.4c06461.
29. Luo, X.; Tan, X.; Guo, X.; et al. $BiVO_4$/Bi:NiO/Co–Ci photoanode and $BiVO_4$–Cu_3BiS_3 tandem cell for unbiased solar hydrogen evolution and simultaneous urea oxidation. *J. Mater. Chem. A* **2025**, *13*, 41780–41787. https://doi.org/10.1039/D5TA07828H.
30. Bachmeier, A.; Hall, S.; Ragsdale, S.W.; et al. Selective Visible-Light-Driven CO_2 Reduction on a p-Type Dye-Sensitized NiO Photocathode. *J. Am. Chem. Soc.* **2014**, *136*, 13518–13521. https://doi.org/10.1021/ja506998b.
31. Click, K.A.; Beauchamp, D.R.; Huang, Z.; et al. Membrane-Inspired Acidically Stable Dye-Sensitized Photocathode for Solar Fuel Production. *J. Am. Chem. Soc.* **2016**, *138*, 1174–1179. https://doi.org/10.1021/jacs.5b07723.
32. Sherman, B.D.; Sheridan, M.V.; Wee, K.-R.; et al. A Dye-Sensitized Photoelectrochemical Tandem Cell for Light Driven Hydrogen Production from Water. *J. Am. Chem. Soc.* **2016**, *138*, 16745–16753. https://doi.org/10.1021/jacs.6b10699.
33. Chen, C.; Chen, A.; Shao, S.; et al. Photoanode/electrolyte interface modification in solar PEC cells sensitized with $Cd_{0.8}Zn_{0.2}S$ quantum dots for efficient dye degradation. *Appl. Surf. Sci.* **2025**, *698*, 163123. https://doi.org/10.1016/j.apsusc.2025.163123.
34. Tang, Y.Q.; Wang, R.R.; Yang, Y.; et al. Highly Enhanced Photoelectrochemical Water Oxidation Efficiency Based on Triadic Quantum Dot/Layered Double Hydroxide/$BiVO_4$ Photoanodes. *ACS Appl. Mater. Interfaces* **2016**, *8*, 19446–19455. https://doi.org/10.1021/acsami.6b04937.
35. Zhou, W.; Liu, M.; Cao, Y.; et al. Breaking the photoelectrochemical activity-battery voltage trade-off for efficient photocharging of TEMPO/quinone redox flow battery. *Chem. Eng. J.* **2025**, *507*, 160162. https://doi.org/10.1016/j.cej.2025.160162.
36. Liang, M.J.; Zhang, J.C.; Ramalingam, K.; et al. Stable and efficient self-sustained photoelectrochemical desalination based on CdS QDs/$BiVO_4$ heterostructure. *Chem. Eng. J.* **2022**, *429*, 132168. https://doi.org/10.1016/j.cej.2021.132168.
37. Zhou, G.; Zhao, T.; Wang, O.; et al. Bi_2Se_3, Bi_2Te_3 quantum dots-sensitized rutile TiO_2 nanorod arrays for enhanced solar photoelectrocatalysis in azo dye degradation. *J. Phys. Energy* **2021**, *3*, 014003. https://doi.org/10.1088/2515-7655/abc52c.
38. Yang, H.; Peng, Y.; Jiang, L.; et al. Carbon quantum dots sensitized Bi_2O_3 photoanode with enhanced photoelectrocatalytic properties. *Chem. Phys. Lett.* **2020**, *739*, 137025. https://doi.org/10.1016/j.cplett.2019.137025.
39. Wang, Z.; Gao, Y.; Lu, Y.; et al. $BiV_{1-x}O_y$/Noble Metal Nanoparticle Domains with Reverse Charge Transfer Improves Photoelectrochemical Glycerol to Dihydroxyacetone Conversion. *J. Am. Chem. Soc.* **2025**, *147*, 40136–40145. https://doi.org/10.1021/jacs.5c06621.
40. Wang, Q.; Zheng, Q.; Jin, R.; et al. Photoelectrocatalytic removal of organic dyes and Cr(VI) ions using Ag_3PO_4 nanoparticles sensitized TiO_2 nanotube arrays. *Mater. Chem. Phys.* **2017**, *199*, 209–215. https://doi.org/10.1016/j.matchemphys.2017.06.051.
41. Chen, X.; Li, X.; Peng, Y.; et al. Tailoring Carrier Dynamics of $BiVO_4$ Photoanode via Dual Incorporation of Au and $Co(OH)_x$ Cooperative Modification for Photoelectrochemical Water Splitting. *Adv. Funct. Mater.* **2025**, *35*, 2416091. https://doi.org/10.1002/adfm.202416091.
42. Liu, Y.; Sui, P.-F.; Wang, Y.-C.; et al. Evoking plasmon electronic and thermal effects via Au nanoparticles for efficient photoelectrochemical water oxidation. *Appl. Catal. B Environ.* **2025**, *374*, 125391. https://doi.org/10.1016/j.apcatb.2025.125391.

43. Xiao, T.T.; Diao, P. Quantifying Localized Surface Plasmon Resonance Induced Enhancement on Metal@Cu_2O Composites for Photoelectrochemical Water Splitting. *Adv. Mater.* **2025**, *37*, 2501069. https://doi.org/10.1002/adma.202501069.
44. Dagnaw, F.W.; Harrath, K.; Zheng, T.; et al. Cationic covalent framework microenvironment steering CuPt alloy toward record-breaking photoelectrochemical ethane synthesis from CO_2. *J. Energy Chem.* **2026**, *112*, 339–349. https://doi.org/10.1016/j.jechem.2025.08.062.
45. Wu, H.; Moncusí, L.M.; Li, J.; et al. Co-Sensitized Solar Cell Achieves 13.7% Efficiency with Bis-Hexylthiophene Dyes. *Adv. Sci.* **2025**, *12*, e09116. https://doi.org/10.1002/advs.202509116.
46. Zhang, J.; Shen, K.D.; Xu, C.; et al. Dual-channeled organic-inorganic hybrid architecture: Leveraging a unique photosensitive semiconductor for enhanced photocatalytic hydrogen evolution. *Appl. Catal. B Environ.* **2025**, *366*, 125025. https://doi.org/10.1016/j.apcatb.2025.125025.
47. Shang, J.; Zhao, F.W.; Zhu, T.; et al. Photocatalytic degradation of rhodamine B by dye-sensitized TiO_2 under visible-light irradiation. *Sci. China Chem.* **2011**, *54*, 167–172. https://doi.org/10.1007/s11426-010-4168-8.
48. Zhang, D.; Yang, S.; Fang, X.; et al. In situ localization of $BiVO_4$ onto two-dimensional MXene promoting photoelectrochemical nitrogen reduction to ammonia. *Chin. Chem. Lett.* **2022**, *33*, 4669–4674. https://doi.org/10.1016/j.cclet.2022.02.001.
49. Lee, E.K.; Baruah, R.K.; Leem, J.W.; et al. Fractal Web Design of a Hemispherical Photodetector Array with Organic-Dye-Sensitized Graphene Hybrid Composites. *Adv. Mater.* **2020**, *32*, 2004456. https://doi.org/10.1002/adma.202004456.
50. Zhao, Y.Y.; Wang, D.; Sun, G.T.; et al. Rhodamine B sensitization promoting TiO_2/$CdIn_2S_4$ S-scheme photocatalytic H_2O_2-production activity and its charge transfer mechanism. *Chem. Eng. J.* **2025**, *518*, 164759. https://doi.org/10.1016/j.cej.2025.164759.
51. Wang, P.; Zong, L.L.; Guan, Z.J.; et al. PtNi Alloy Cocatalyst Modification of Eosin Y-Sensitized g-C_3N_4/GO Hybrid for Efficient Visible-Light Photocatalytic Hydrogen Evolution. *Nanoscale Res. Lett.* **2018**, *13*, 33. https://doi.org/10.1186/s11671-018-2448-y.
52. Yu, F.T.; Wang, Z.Q.; Zhang, S.C.; et al. N-Annulated perylene-based organic dyes sensitized graphitic carbon nitride to form an amide bond for efficient photocatalytic hydrogen production under visible-light irradiation. *Appl. Catal. B Environ.* **2018**, *237*, 32–42. https://doi.org/10.1016/j.apcatb.2018.05.045.
53. Sun, B.; Ouellette, O.; de Arquer, F.P.G.; et al. Multibandgap quantum dot ensembles for solar-matched infrared energy harvesting. *Nat. Commun.* **2018**, *9*, 4003. https://doi.org/10.1038/s41467-018-06342-7.
54. Shi, L.; Daniele, B.; Li, F.; et al. MOF-Templated Metal Oxides Sensitized with Quantum Dots Heterojunction for Efficient Solar Fuels Generation. *ECS Meet. Abstr.* **2020**, *MA2020-01*, 1350. https://doi.org/10.1149/ma2020-01231350mtgabs.
55. Li, Y.Y.; Wu, S.; Zheng, J.W.; et al. 2D photocatalysts with tuneable supports for enhanced photocatalytic water splitting. *Mater. Today* **2020**, *41*, 34–43. https://doi.org/10.1016/j.mattod.2020.05.018.
56. Sahu, A.; Garg, A.; Dixit, A. A review on quantum dot sensitized solar cells: Past, present and future towards carrier multiplication with a possibility for higher efficiency. *Sol. Energy.* **2020**, *203*, 210–239. https://doi.org/10.1016/j.solener.2020.04.044.
57. Liu, J.; Cao, S.; Xu, H.; et al. Designing Hybrid Electrodes for Fiber Quantum Dot-Sensitized Solar Cells with Record 11.05% Efficiency. *Adv. Funct. Mater.* **2025**, *36*, e23627. https://doi.org/10.1002/adfm.202523627.
58. Xu, M.; Lin, L.; Jin, G.; et al. Two-in-one: Portable piezoelectric and plasmonic exciton effect-based co-enhanced photoelectrochemical biosensor for point-of-care testing of low-abundance cancer markers. *Biosens. Bioelectron.* **2022**, *211*, 114413. https://doi.org/10.1016/j.bios.2022.114413.
59. Tian, Y.; Cui, Q.Q.; Xu, L.L.; et al. Alloyed AuPt nanoframes loaded on h-BN nanosheets as an ingenious ultrasensitive near-infrared photoelectrochemical biosensor for accurate monitoring glucose in human tears. *Biosens. Bioelectron.* **2021**, *192*, 113490. https://doi.org/10.1016/j.bios.2021.113490.
60. Chen, Y.L.; Yao, Q.; Zhang, L.J.; et al. HPLC for simultaneous quantification of free mannose and glucose concentrations in serum: Use in detection of ovarian cancer. *Front. Chem.* **2023**, *11*, 1289211. https://doi.org/10.3389/fchem.2023.1289211.
61. Li, M.X.; Wang, H.Y.; Wang, X.X.; et al. Ti_3C_2/Cu_2O heterostructure based signal-off photoelectrochemical sensor for high sensitivity detection of glucose. *Biosens. Bioelectron.* **2019**, *142*, 111535. https://doi.org/10.1016/j.bios.2019.111535.
62. Datta, D.; Mondal, R.; Maji, R.C.; et al. Anisotropic Au nanobypyramids with molybdenum disulfide for plasmon-enhanced electrocatalysis, biosensing and energy production. *Nanoscale Horiz.* **2025**, *10*, 3453–3468. https://doi.org/10.1039/d5nh00491h.
63. Li, S.Q.; Li, Z.X.; Yue, J.N.; et al. Photocatalytic CO_2 Reduction by Near-Infrared-Light (1200 nm) Irradiation and a Ruthenium-Intercalated NiAl-Layered Double Hydroxide. *Angew. Chem. Int. Ed.* **2024**, *63*, e20240763. https://doi.org/10.1002/anie.202407638.
64. Long, D.; Qian, G.L.; Ma, S.H.; et al. Two-dimensional photocatalysts for photoreduction of CO_2. *Renew. Sustain. Energy Rev.* **2026**, *226*, 116222. https://doi.org/10.1016/j.rser.2025.116222.
65. Suryawanshi, M.P.; Ghorpade, U.V.; Shin, S.W.; et al. Facile, Room Temperature, Electroless Deposited (Fe_{1-x},Mn_x)OOH Nanosheets as Advanced Catalysts: The Role of Mn Incorporation. *Small* **2018**, *14*, 1801226. https://doi.org/10.1002/smll.201801226.

66. Tran, T.T.T.; Trinh, V.Y.; Seo, J. Two-dimensional perovskite $SrNbO_2N$ with Zr doping for accelerating photoelectrochemical water splitting. *J. Mater. Sci. Technol.* **2023**, *142*, 176–184. https://doi.org/10.1016/j.jmst.2022.09.034.
67. Li, W.Z.; Liu, Y.; Wang, Z.Y.; et al. Fabrication of C and N co-doped CdS semiconductor photocatalysts derived from a novel Cd-MOF for enhancing photocatalytic performance. *J. Environ. Chem. Eng.* **2024**, *12*, 114204. https://doi.org/10.1016/j.jece.2024.114204.
68. Zhang, M.X.; Luo, W.; Gu, S.H.; et al. Photoelectrochemical catalytic CO_2 reduction enhanced by In-doped GaN and combined with vibration energy harvester driving CO_2 reduction. *Appl. Catal. A Gen.* **2024**, *683*, 119859. https://doi.org/10.1016/j.apcata.2024.119859.
69. Li, S.; Zhang, G.; Meng, D.; et al. Photoelectrocatalytic activation of sulfate for sulfamethoxazole degradation and simultaneous H_2 production by bifunctional N,P co-doped black-blue TiO_2 nanotube array electrode. *Chem. Eng. J.* **2024**, *485*, 149828. https://doi.org/10.1016/j.cej.2024.149828.
70. Hu, C.L.; Wu, J.H.; Dong, C.Z.; et al. Enhancement of the photoelectrochemical water splitting performance of hematite photoanodes via uniform Ti and gradient Ge co-doping. *Inorg. Chem. Front.* **2025**, *12*, 5037–5045. https://doi.org/10.1039/d5qi00700c.
71. Gu, W.; Chen, W.; Wang, W.; et al. Highly Coupled Dynamically Modulated Electrocatalysts on Wafer-Scale InGaN/GaN Nanowires on Silicon for Successive Acidic Photoelectrochemical Water Oxidation. *Adv. Mater.* **2025**, *37*, 2501218. https://doi.org/10.1002/adma.202501218.
72. Li, C.; Song, J.W.; Ma, P.J.; et al. Ladder-Like Built-In Electric Field Enhances Self-Assembly, Carrier Separation and Ultra-Efficient Photocatalytic Oxygen Reduction. *Adv. Mater.* **2025**, *37*, 2502918. https://doi.org/10.1002/adma.202502918.
73. Ai, M.H.; Peng, Z.H.; Li, X.D.; et al. Piezoelectric-enhanced n-TiO_2/$BaTiO_3$/p-TiO_2 heterojunction for highly efficient photoelectrocatalysis. *Green Energy Environ.* **2024**, *9*, 1466–1476. https://doi.org/10.1016/j.gee.2023.12.001.
74. Sun, P.P.; Zhang, J.Y.; Song, Y.H.; et al. Built-in Electric Fields Enhancing Photocarrier Separation and H_2 Evolution. *Acta Phys.-Chim. Sin.* **2024**, *40*, 2311001. https://doi.org/10.3866/Pku.Whxb202311001.
75. Guo, H.; Wang, S.; Chen, X.; et al. Engineering a covalent organic framework-based type-II heterojunction for enhanced photocatalytic H_2O_2 synthesis. *Nat. Synth.* **2025**, *4*, 1610–1620. *https://doi.org*/10.1038/s44160-025-00880-x.
76. Han, Z.; Song, Y.; Jia, Y.; et al. Classification and Characterization Methods for Heterojunctions. *Adv. Mater. Interfaces* **2025**, *12*, 2500191. https://doi.org/10.1002/admi.202500191.
77. Meng, Z.; Zhang, J.J.; Long, H.Y.; et al. Kelvin Probe Force Microscopy Reveals Spatially Resolved Charge-Transfer Mechanism in CdS/BiOBr S-scheme Heterojunction Photocatalyst. *Angew. Chem. Int. Ed.* **2025**, *64*, e202505456. https://doi.org/10.1002/anie.202505456.
78. Zhu, H.D.; Ren, X.F.; Yang, X.X.; et al. Fe-based catalysts for nitrogen reduction toward ammonia electrosynthesis under ambient conditions. *SusMat* **2022**, *2*, 214–242. https://doi.org/10.1002/sus2.70.
79. Li, X.; Fan, W.Q.; Xu, D.B.; et al. Boosted Photoelectrochemical N_2 Reduction over Mo_2C In Situ Coated with Graphitized Carbon. *Langmuir* **2020**, *36*, 14802–14810. https://doi.org/10.1021/acs.langmuir.0c02770.
80. Bo, Y.R.; Li, L.R.; Miao, P.; et al. 2D Z-scheme $ZnIn_2S_4$/g-C_3N_4 heterojunction based on photoelectrochemical immunosensor with enhanced carrier separation for sensitive detection of CEA. *Biosens. Bioelectron.* **2024**, *247*, 115926. https://doi.org/10.1016/j.bios.2023.115926.
81. Tan, J.X.; Cheng, Y.F.; Li, Q.J.; et al. Construction of 1D/2D $Sb_2(S,Se)_3$/In_2S_3 S-Scheme Heterojunction Photoanodes toward Photoelectrochemical Water Splitting. *Langmuir* **2025**, *41*, 27444–27454. https://doi.org/10.1021/acs.langmuir.5c03796.
82. Chung, C.C.; Yeh, H.; Wu, P.H.; et al. Atomic-Layer Controlled Interfacial Band Engineering at Two-Dimensional Layered $PtSe_2$/Si Heterojunctions for Efficient Photoelectrochemical Hydrogen Production. *Acs Nano* **2021**, *15*, 4627–4635. https://doi.org/10.1021/acsnano.0c08970.
83. Bhat, S.S.M.; Pawar, S.A.; Potphode, D.; et al. Substantially enhanced photoelectrochemical performance of TiO_2 nanorods/CdS nanocrystals heterojunction photoanode decorated with MoS_2 nanosheets. *Appl. Catal. B Environ.* **2019**, *259*, 118102. https://doi.org/10.1016/j.apcatb.2019.118102.
84. Zhang, M.; Xuan, X.; Wang, W.; et al. Anode Photovoltage Compensation-Enabled Synergistic CO_2 Photoelectrocatalytic Reduction on a Flower-Like Graphene-Decorated Cu Foam Cathode. *Adv. Funct. Mater.* **2020**, *30*, 2005983. https://doi.org/10.1002/adfm.202005983.
85. Wang, J.; Liu, K.; Liao, W.R.; et al. Metal vacancies in semiconductor oxides enhance hole mobility for efficient photoelectrochemical water splitting. *Nat. Catal.* **2025**, *8*, 229–238. https://doi.org/10.1038/s41929-025-01300-1.
86. Kang, X.S.; Dong, G.H.; Dong, T.T. Oxygen Vacancy Defect Engineering of Heterophase Junction TiO_2: Interfacial/Surface Oxygen Vacancies Coadjust the Photocatalytic ROS Production. *ACS Appl. Energy Mater.* **2023**, *6*, 1025–1036. https://doi.org/10.1021/acsaem.2c03535.
87. Man, P.; Jiang, S.; Leung, K.H.; et al. Salt-Induced High-Density Vacancy-Rich 2D MoS_2 for Efficient Hydrogen Evolution. *Adv. Mater.* **2024**, *36*, 2304808. https://doi.org/10.1002/adma.202304808.
88. Liang, J.W.; Li, S.B.; Li, F.B.; et al. Defect engineering induces Mo-regulated Co_9Se_8/FeNiSe heterostructures with

selenium vacancy for enhanced electrocatalytic overall water splitting in alkaline. *J. Colloid. Interf. Sci.* **2024**, *655*, 296–306. https://doi.org/10.1016/j.jcis.2023.11.010.

89. Zhou, Y.Q.; Zhang, L.F.; Suo, H.L.; et al. Atomic Cobalt Vacancy-Cluster Enabling Optimized Electronic Structure for Efficient Water Splitting. *Adv. Funct. Mater.* **2021**, *31*, 2101797. https://doi.org/10.1002/adfm.202101797.
90. Wang, Y.H.; Hu, J.C.; Ge, T.; et al. Gradient Cationic Vacancies Enabling Inner-To-Outer Tandem Homojunctions: Strong Local Internal Electric Field and Reformed Basic Sites Boosting CO_2 Photoreduction. *Adv. Mater.* **2023**, *35*, 2302538. https://doi.org/10.1002/adma.202302538.
91. Jiang, X.L.; Ma, X.H.; Liu, Y.X.; et al. Cation vacancies creation propel pre-oxidation enhancing nickel hydroxide activity for highly efficient 5-hydroxymethylfurfural upgrading. *Appl. Catal. B Environ.* **2024**, *347*, 123785. https://doi.org/10.1016/j.apcatb.2024.123785.
92. Chen, C.-J.; Yeh, C.-Y.; Chen, C.-H.; et al. Molybdenum Tungsten Disulfide with a Large Number of Sulfur Vacancies and Electronic Unoccupied States on Silicon Micropillars for Solar Hydrogen Evolution. *ACS Appl. Mater. Interfaces* **2020**, *12*, 54671–54682. https://doi.org/10.1021/acsami.0c15905.
93. Zheng, H.; Jiang, S.; Liu, Y.; et al. Improved photocathodic protection performance of C-vacancy g-C_3N_4/GO/WO_3 for 304 stainless steel. *J. Phys. Chem. Solids* **2022**, *160*, 110270. https://doi.org/10.1016/j.jpcs.2021.110270.
94. Huang, W.T.; Zhou, Q.W.; Su, S.Q.; et al. Ion Beam Defect Engineering on ReS_2/Si Photocathode with Significantly Enhanced Hydrogen Evolution Reaction. *Adv. Mater. Interfaces* **2019**, *6*, 1801663. https://doi.org/10.1002/admi.201801663.
95. Lu, J.; Chen, Y.; Li, L.; et al. Facet engineering on the interface of BiOCl-PbS heterostructures for enhanced broad-spectrum photocatalytic H_2 production. *Chem. Eng. J.* **2019**, *362*, 1–11. https://doi.org/10.1016/j.cej.2018.12.130.
96. Liu, B.Y.; Wang, X.; Zhang, Y.J.; et al. Bismuth Vacancies Induced Lattice Strain in $BiVO_4$ Photoanodes Boosting Charge Separation For Water Oxidation. *Adv. Energy Mater.* **2025**, *15*, 2403835. https://doi.org/10.1002/aenm.202403835.
97. Hu, Y.; Jin, Y.Z.; Gao, Y.Q.; et al. Interface and Defect Engineering in 3D Co_3O_{4-Ov}/TiO_2 to Boost Simultaneous Removal of BPA and Cr(VI) upon Photoelectrocatalytic/Peroxymonosulfate (PEC/PMS) System. *Adv. Funct. Mater.* **2025**, *35*, 2414350. https://doi.org/10.1002/adfm.202414350.
98. Bai, H.; Yang, Y.X.; Huang, Y.; et al. Quantum confinement and defect engineering mediated "two birds with one stone" strategy for Co/Bi self-regeneration and effective photogenerated carrier separation. *Appl. Catal. B: Environ.* **2025**, *365*, 125001. https://doi.org/10.1016/j.apcatb.2024.125001.
99. Chu, D.D.; Xing, C.; Sun, D.Y.; et al. Defective In_2S_3 with Proton-Enriched Interface Enable Sacrificial-Agent-Free Visible-Light Photocatalytic H_2O_2 Production. *Adv. Funct. Mater.* **2025**, *36*, e16500. https://doi.org/10.1002/adfm.202516500.
100. Hou, J.H.; Zhang, T.T.; Jiang, T.; et al. Fast preparation of oxygen vacancy-rich 2D/2D bismuth oxyhalides-reduced graphene oxide composite with improved visible-light photocatalytic properties by solvent-free grinding. *J. Clean. Prod.* **2021**, *328*, 129651. https://doi.org/10.1016/j.jclepro.2021.129651.
101. Rana, M.M.; Alam, K.M.; Chaulagain, N.; et al. Tunable Absorption and Emission in Mixed Halide Bismuth Oxyhalides for Photoelectrochemical Water Splitting. *ACS Appl. Nano Mater.* **2024**, *7*, 6005–6019. https://doi.org/10.1021/acsanm.3c05925.
102. Wang, X.; Zhang, Y.; Zhou, C.; et al. Hydroxyl-regulated BiOI nanosheets with a highly positive valence band maximum for improved visible-light photocatalytic performance. *Appl. Catal. B Environ.* **2019**, *268*, 118390. https://doi.org/10.1016/j.apcatb.2019.118390.
103. Fu, R.R.; Zeng, X.Q.; Ma, L.; et al. Enhanced photocatalytic and photoelectrochemical activities of reduced TiO_{2-x}/BiOCl heterojunctions. *J. Power Sources* **2016**, *312*, 12–22. https://doi.org/10.1016/j.jpowsour.2016.02.038.
104. Kshetri, T.; Tran, D.T.; Le, H.T.; et al. Recent advances in MXene-based nanocomposites for electrochemical energy storage applications. *Prog. Mater. Sci.* **2021**, *117*, 100733. https://doi.org/10.1016/j.pmatsci.2020.100733.
105. Hussain, I.; Amna, R.; Kalidasan, B.; et al. MXenes for Various Applications: Recent Trends and Future Aspects. *SmartMat* **2025**, *6*, e70012. https://doi.org/10.1002/smm2.70012.
106. Zhou, S.Q.; Jiang, C.X.; Han, J.L.; et al. High-Performance Self-Powered PEC Photodetectors Based on 2D $BiVO_4$/MXene Schottky Junction. *Adv. Funct. Mater.* **2025**, *35*, 2416922. https://doi.org/10.1002/adfm.202416922.
107. Zeng, W.; Zhang, Y.; Wu, Z.Y.; et al. Hierarchically Converged Defect Engineering with 2-Dimensional Black Phosphorus/MXene Sequence for Sensitive Photoelectrochemical-Electrostatic Sensors. *Research* **2025**, *8*, 0966. https://doi.org/10.34133/research.0966.
108. Yang, G.L.; Li, S.J.; Wang, X.S.; et al. A universal strategy boosting photoelectrochemical water oxidation by utilizing MXene nanosheets as hole transfer mediators. *Appl. Catal. B Environ.* **2021**, *297*, 120268. https://doi.org/10.1016/j.apcatb.2021.120268.
109. Xu, Y.J.; Wang, F.; Lei, S.L.; et al. In situ grown two-dimensional TiO_2/Ti_3CN MXene heterojunction rich in Ti^{3+} species for highly efficient photoelectrocatalytic CO_2 reduction. *Chem. Eng. J.* **2023**, *452*, 139392. https://doi.org/10.1016/j.cej.2022.139392.
110. Kang, M.J.; Kim, C.W.; Pawar, A.U.; et al. Selective Alcohol on Dark Cathodes by Photoelectrochemical CO_2 Valorization and Their In Situ Characterization. *Acs Energy Lett.* **2019**, *4*, 1549–1555. https://doi.org/10.1021/acsenergylett.9b00927.
111. Park, H.R.; Pawar, A.U.; Pal, U.; et al. Enhanced solar photoreduction of CO_2 to liquid fuel over rGO grafted NiO-CeO_2

heterostructure nanocomposite. *Nano Energy* **2021**, *79*, 105483. https://doi.org/10.1016/j.nanoen.2020.105483.

112. Jung, M.; Kim, C.W.; Kim, S.Y.; et al. Boosting Photoelectrochemical Ethanol Evolution on Reduced Graphene Oxide Functionalized Photocathode. *Adv. Energy Mater.* **2022**, *12*, 2202160. https://doi.org/10.1002/aenm.202202160.
113. Niu, P.; Zhang, L.L.; Liu, G.; et al. Graphene-Like Carbon Nitride Nanosheets for Improved Photocatalytic Activities. *Adv. Funct. Mater.* **2012**, *22*, 4763–4770. https://doi.org/10.1002/adfm.201200922.
114. Wang, X.C.; Maeda, K.; Chen, X.F.; et al. Polymer Semiconductors for Artificial Photosynthesis: Hydrogen Evolution by Mesoporous Graphitic Carbon Nitride with Visible Light. *J. Am. Chem. Soc.* **2009**, *131*, 1680–1681. https://doi.org/10.1021/ja809307s.
115. Yang, S.B.; Gong, Y.J.; Zhang, J.S.; et al. Exfoliated Graphitic Carbon Nitride Nanosheets as Efficient Catalysts for Hydrogen Evolution Under Visible Light. *Adv. Mater.* **2013**, *25*, 2452–2456. https://doi.org/10.1002/adma.201204453.
116. Lu, Z.; Li, C.; Han, J.; et al. Construction 0D/2D heterojunction by highly dispersed Ni_2P QDs loaded on the ultrathin g-C_3N_4 surface towards superhigh photocatalytic and photoelectric performance. *Appl. Catal. B Environ.* **2018**, *237*, 919–926. https://doi.org/10.1016/j.apcatb.2018.06.062.
117. Wang, J.; Yang, Z.; Gao, X.X.; et al. Core-shell g-C_3N_4@ZnO composites as photoanodes with double synergistic effects for enhanced visible-light photoelectrocatalytic activities. *Appl. Catal. B Environ.* **2017**, *217*, 169–180. https://doi.org/10.1016/j.apcatb.2017.05.034.
118. Jerome, M.P.; Alahmad, F.A.; Salem, M.T.; et al. Layered double hydroxide (LDH) nanomaterials with engineering aspects for photocatalytic CO_2 conversion to energy efficient fuels: Fundamentals, recent advances, and challenges. *J. Environ. Chem. Eng.* **2022**, *10*, 108151. https://doi.org/10.1016/j.jece.2022.108151.
119. Silva, C.G.; Bouizi, Y.; Fornés, V.; et al. Layered Double Hydroxides as Highly Efficient Photocatalysts for Visible Light Oxygen Generation from Water. *J. Am. Chem. Soc.* **2009**, *131*, 13833–13839. https://doi.org/10.1021/ja905467v.
120. Mohapatra, L.; Parida, K. A review on the recent progress, challenges and perspective of layered double hydroxides as promising photocatalysts. *J. Mater. Chem. A* **2016**, *4*, 10744–10766. https://doi.org/10.1039/c6ta01668e.
121. Cho, D.K.; Jeon, C.W.; Park, I.K. Growth and optical band gap of CdAl-layered double hydroxide thin structures on rigid substrate. *J. Alloys Compd.* **2018**, *737*, 725–730. https://doi.org/10.1016/j.jallcom.2017.12.163.
122. Intachai, S.; Nakato, T.; Khaorapapong, N. ZnO decorated on low carbonate NiAl-layered double hydroxide as efficient photocatalyst for methyl orange degradation. *Appl. Clay Sci.* **2021**, *201*, 105927. https://doi.org/10.1016/j.clay.2020.105927.
123. Chen, Y.; Xu, L.; Dong, J.T.; et al. An enhanced photoelectrochemical ofloxacin aptasensor using NiFe layered double hydroxide/graphitic carbon nitride heterojunction. *Electrochim. Acta* **2021**, *368*, 137595. https://doi.org/10.1016/j.electacta.2020.137595.
124. Yang, S.M.; Deng, K.Q.; Zhang, J.; et al. Synergy effect of Ag plasmonic resonance and heterostructure construction enhanced visible-light photoelectrochemical sensing for quercetin. *Electrochim. Acta* **2021**, *371*, 137772. https://doi.org/10.1016/j.electacta.2021.137772.
125. Yang, X.H.; Sun, J.J.; Fu, H.T.; et al. MoS_2 modified NiFe LDH hierarchical structure as efficient photoanode towards photoelectrochemical water splitting. *Powder Technol.* **2024**, *431*, 119051. https://doi.org/10.1016/j.powtec.2023.119051.
126. Choi, S.; Lee, S.A.; Yang, J.W.; et al. Boosted charge transport through Au-modified NiFe layered double hydroxide on silicon for efficient photoelectrochemical water oxidation. *J. Mater. Chem. A* **2023**, *11*, 17503–17513. https://doi.org/10.1039/d3ta03075j.
127. Zheng, L.X.; Xu, P.H.; Zhao, Y.J.; et al. Solar-driven upgrading of 5-hydroxymethylfurfural on $BiVO_4$ photoanodes: Effect of TEMPO mediator and cocatalyst on reaction kinetics. *Appl. Catal. B Environ.* **2023**, *331*, 122679. https://doi.org/10.1016/j.apcatb.2023.122679.
128. Fang, G.Z.; Zhang, D.T.; Zhang, X.L.; et al. Balanced Spin-State Energy Level Splitting Boosts Photoelectrochemical Water Oxidation on Amorphous NiFeAl-LDH Engineered BiVO4. *Adv. Funct. Mater.* **2025**, *36*, e18870. https://doi.org/10.1002/adfm.202518870.
129. Ren, J.; Li, Z.X.; Wang, R.Y.; et al. Lattice distortion promotes dehydrogenation of layered double hydroxide for enhanced electrocatalytic oxidation activity. *AIChE J.* **2025**, *72*, e70104. https://doi.org/10.1002/aic.70104.
130. Zhou, S.J.; Liu, X.; Gunawan, M.; et al. Unassisted Photoelectrochemical Hydrogen Production Coupled with Selective Glucose Oxidation Using Metal Halide Perovskite Photoanodes. *Adv. Funct. Mater.* **2025**, *36*, 2505281. https://doi.org/10.1002/adfm.202505281.
131. Ma, W.C.; He, X.Y.; Wang, W.; et al. Electrocatalytic reduction of CO_2 and CO to multi-carbon compounds over Cu-based catalysts. *Chem. Soc. Rev.* **2021**, *50*, 12897–12914. https://doi.org/10.1039/d1cs00535a.
132. Wang, Q.; Ma, X.; Wu, P.; et al. CoNiFe-LDHs decorated Ta3N5 nanotube array photoanode for remarkably enhanced photoelectrochemical glycerol conversion coupled with hydrogen generation. *Nano Energy* **2021**, *89*, 106326. https://doi.org/10.1016/j.nanoen.2021.106326.
133. Yang, H.; Wang, H.; Wang, P.; et al. Energy-Transfer-Based Dual-Mode PEC-ECL Biosensor for Acetamiprid Analysis Sensitized by Two-Step DNA Circuit Amplification. *ACS Appl. Mater. Interfaces* **2025**, *17*, 3052–3061.

https://doi.org/10.1021/acsami.4c18752.

134. Lyu, R.; Lei, Y.; Zhang, C.; et al. An ultra-sensitive photoelectrochemical sensor for chlorpyrifos detection based on a novel BiOI/TiO2 n-n heterojunction. *Anal. Chim. Acta* **2023**, *1275*, 341579. https://doi.org/10.1016/j.aca.2023.341579.
135. Hu, C.-C.; Zhang, Q.-E.; Shi, S.-P.; et al. Ti_3C_2-Cl-$Bi_{12}O_{17}Cl_2$/$Bi_{12}O_{17}Cl_2$ Mott-Schottky heterojunction with mixed noncovalent/covalent type to boost ultra-sensitive photoelectrochemical sensing of ciprofloxacin. *Chem. Eng. J.* **2025**, *527*, 171533. https://doi.org/10.1016/j.cej.2025.171533.
136. Li, L.; Min, Z.; Lu, Z.; et al. Bi-doped $BiOBr_{0.5}I_{0.5}$ solid solution catalysts with synergistic effect of SPR and oxygen vacancies for enhanced photoelectrochemical sensing of oxytetracycline in food sample. *J. Food Compos. Anal.* **2025**, *148*, 108459. https://doi.org/10.1016/j.jfca.2025.108459.
137. Zhao, H.; Li, X.; Yu, K.; et al. A MOF-on-MOF based photoelectrochemical sensor for hydrogen sulfide detection in food quality assessment. *Sens. Actuator B-Chem.* **2025**, *433*, 137525. https://doi.org/10.1016/j.snb.2025.137525.
138. Zhang, B.; Jian, X.; An, Z.; et al. A colorimetric and photocurrent-polarity-switching photoelectrochemical dual-mode biosensor for the ultrasensitive detection of DNA damage biomarker and rapid screening of genotoxic chemicals. *Biosens. Bioelectron.* **2025**, *279*, 117396. https://doi.org/10.1016/j.bios.2025.117396.
139. Wu, C.; Hao, Z.; Deng, H.; et al. AgI Precipitation Induced Polarity Reversal with Formation of Z-Type Heterojunction for Photoelectrochemical Sensing. *Anal. Chem.* **2024**, *96*, 14759–14765. https://doi.org/10.1021/acs.analchem.4c01577.
140. Wang, J.; Guo, Q.; Li, Q.; et al. A "signal-off" type photoelectrochemical immunosensor for detecting carcinoembryonic antigen based on TiO_2 NRs/BiOI heterojunction and SiO2/PDA-Au inhibitor. *Microchem. J.* **2022**, *182*, 107888. https://doi.org/10.1016/j.microc.2022.107888.
141. Suo, Z.; Yu, T.; Xu, Y.; et al. Research progress of photoelectrochemical sensors in food detection. *Food Res. Int.* **2025**, *206*, 116071. https://doi.org/10.1016/j.foodres.2025.116071.
142. Liu, Y.-L.; Da, H.-M.; Chai, Y.-Q.; et al. Photoelectrochemical aptamer-based sensing of the vascular endothelial growth factor by adjusting the light harvesting efficiency of g-C3N4 via porous carbon spheres. *Microchim. Acta* **2019**, *186*, 275. https://doi.org/10.1007/s00604-019-3393-x.
143. Dong, W.; Li, Z.; Wen, W.; et al. PCN-222@g-C_3N_4 cathodic materials for "signal-off" photoelectrochemical sensing of kanamycin sulfate. *RSC Adv.* **2021**, *11*, 28320. https://doi.org/10.1039/d1ra04275k.
144. Blanchaert, B.; Jorge, E.P.; Jankovics, P.; et al. Assay of Kanamycin A by HPLC with Direct UV Detection. *Chromatographia* **2013**, *76*, 1505–1512. https://doi.org/10.1007/s10337-013-2440-8.
145. Perez, J.J.; Chen, C.Y. Rapid detection and quantification of aminoglycoside phosphorylation products using direct-infusion high-resolution and ultra-high-performance liquid chromatography/mass spectrometry. *Rapid Commun. Mass. Sp.* **2018**, *32*, 1822–1828. https://doi.org/10.1002/rcm.8241.
146. Guo, J.; Song, L.; Chen, M.; et al. Schottky-functionalized Z-scheme heterojunction: Improved photoelectric conversion efficiency and immunosensing. *Biosens. Bioelectron.* **2022**, *222*, 115000. https://doi.org/10.1016/j.bios.2022.115000.
147. Ding, K.; Zhong, R.; Zhang, Z.; et al. Photoelectrochemical Nanofiber Ferritin Sensor with Integrated "Migrating-Destructing-Detecting" Capability. *Adv. Funct. Mater.* **2025**, *36*, e18124. https://doi.org/10.1002/adfm.202518124.
148. Tan, R.; Qin, Y.; Liu, M.; et al. Nickel Single-Atom Catalyst-Mediated Efficient Redox Cycle Enables Self-Checking Photoelectrochemical Biosensing with Dual Photocurrent Readouts. *ACS Sens.* **2023**, *8*, 263–269. https://doi.org/10.1021/acssensors.2c02125.
149. Wu, S.; Deng, J.; Wang, X.; et al. Polarization photodetectors with configurable polarity transition enabled by programmable ferroelectric-doping patterns. *Nat. Commun.* **2024**, *15*, 8743. https://doi.org/10.1038/s41467-024-52877-3.
150. Geng, W.; Liu, H.; Yuan, X.; et al. 1D/3D MOF-919-Sc Networked Octahedron-Derived 2D/3D Sc_2O_3@CuO Layered Octahedron for Polarity-Switchable Photoelectrochemical Sensing. *Anal. Chem.* **2025**, *97*, 13984–13992. https://doi.org/10.1021/acs.analchem.5c02283.
151. Hu, R.; Ren, X.-X.; Song, P.; et al. Hollow cage-like PtCu nanozyme-regulated photo-activity of porous $CdIn_2S_4$/SnO_2 heterojunctions for ultrasensitive PEC sensing of streptomycin. *Biosens. Bioelectron.* **2023**, *236*, 115425. https://doi.org/10.1016/j.bios.2023.115425.
152. Wu, Z.G.; Zhao, J.L.; Yin, Z.K.; et al. Highly sensitive photoelectrochemical detection of glucose based on BiOBr/TiO_2 nanotube array p-n heterojunction nanocomposites. *Sens. Actuators B Chem.* **2020**, *312*, 127978. https://doi.org/10.1016/j.snb.2020.127978.
153. Shen, Y.; Quan, C.; Ma, K. Accurate Determination of Serum Glucose by Liquid Chromatography-Isotope Dilution Mass Spectrometry. *J. Chin. Mass Spectrom. Soc.* **2011**, *32*, 211–215.
154. Yu, S.Y.; Chen, X.; Huang, C.B.; et al. A Cu^{2+}-doped two-dimensional material-based heterojunction photoelectrode: Application for highly sensitive photoelectrochemical detection of hydrogen sulfide. *Rsc Adv.* **2019**, *9*, 28276–28283. https://doi.org/10.1039/c9ra05385a.
155. Li, C.; Chen, J.; Su, Y.; et al. Establishment of a method for the determination of hydrogen sulfide in human serum by liquid chromatography-tandem mass spectrometry and evaluation of its clinical application. *Acta Biochim. Biophys. Sin.*

2024, *56*, 494–498. https://doi.org/10.3724/abbs.2024007.

156. Zhang, Z.; Wu, X.; Wei, C.; et al. Determination of hydrogen sulfide in blood by trichloroacetic acid acidification HS-GC-FPD. *Chin. J. Forensic Med.* **2022**, *37*, 471–474+484. https://doi.org/10.13618/j.issn.1001-5728.2022.05.012.
157. Li, R.Y.; Zhang, Y.; Tu, W.W.; et al. Photoelectrochemical Bioanalysis Platform for Cells Monitoring Based on Dual Signal Amplification Using in Situ Generation of Electron Acceptor Coupled with Heterojunction. *Acs Appl. Mater. Inter.* **2017**, *9*, 22289–22297. https://doi.org/10.1021/acsami.7b06107.
158. Park, J.; Noh, H.; Suh, H.J.; et al. High-performance liquid chromatography using diode array detector and fluorescence detector for hydrogen peroxide analysis in processed fishery foods. *Food Sci. Biotechnol.* **2023**, *32*, 27–37. https://doi.org/10.1007/s10068-022-01165-1.
159. Shin, G.S.; Shin, H.S. Determination of hydrogen peroxide in milk and coffee by gas chromatography-mass spectrometry after 4-iodo-2,6-dimethylphenol derivatization. *J. Food Compos. Anal.* **2025**, *137*, 106872. https://doi.org/10.1016/j.jfca.2024.106872.
160. Li, R.Z.; Liu, Y.; Cheng, L.; et al. Photoelectrochemical Aptasensing of Kanamycin Using Visible Light-Activated Carbon Nitride and Graphene Oxide Nanocomposites. *Anal. Chem.* **2014**, *86*, 9372–9375. https://doi.org/10.1021/ac502616n.
161. Su, P.; Chen, X.N.; He, Z.J.; et al. Preparation of Polyclonal Antibody and Development of a Biotin-streptavidin-based ELISA Method for Detecting Kanamycin in Milk and Honey. *Chem. Res. Chin. Univ.* **2017**, *33*, 876–881. https://doi.org/10.1007/s40242-017-7168-9.
162. He, J.X.; Wang, Y.; Zhang, X.Y. Preparation of Artificial Antigen and Development of IgY-Based Indirect Competitive ELISA for the Detection of Kanamycin Residues. *Food Anal. Methods* **2016**, *9*, 744–751. https://doi.org/10.1007/s12161-015-0248-x.
163. Zhang, L.X.; Feng, L.P.; Zhuang, X.; et al. A visible-light-driven photoelectrochemical sensor for the sensitive and selective detection of chlorpyrifos via CoS_2 quantum dots/CdS nanowires nanocomposites with 0D/1D heterostructure. *Chem. Eng. J.* **2023**, *476*, 146770. https://doi.org/10.1016/j.cej.2023.146770.
164. Ma, J.K.; Huang, X.C.; Wei, S.L. Preparation and application of chlorpyrifos molecularly imprinted solid-phase microextraction probes for the residual determination of organophosphorous pesticides in fresh and dry foods. *J. Sep. Sci.* **2018**, *41*, 3152–3162. https://doi.org/10.1002/jssc.201800385.
165. Koshki, M.-S.; Baghayeri, M.; Salemi, S.; et al. A simple-structured enzyme-free photoelectrochemical sensor: Facile deposition of mesoporous BiVO4 thin film for selective ascorbic acid detection with outstanding long-term stability. *Food Chem.* **2025**, *489*, 145115. https://doi.org/10.1016/j.foodchem.2025.145115.
166. Wang, L.; Li, L.; Wang, N.; et al. GDH-TiO_2NFs-rGO photoelectrode: A novel photoelectric chemobiosensor for lipase activity detection. *Int. J. Biol. Macromol.* **2025**, *307*, 141708. https://doi.org/10.1016/j.ijbiomac.2025.141708.
167. Friebe, V.M.; Barszcz, A.J.; Jones, M.R.; et al. Sustaining Electron Transfer Pathways Extends Biohybrid Photoelectrode Stability to Years. *Angew. Chem. Int. Ed.* **2022**, *61*, e202201148. https://doi.org/10.1002/anie.202205845.
168. Su, A.; Lei, Q.; Tian, G.; et al. An Enzyme-free Glucose Sensing Device Based on TiO2 Nanorod Array Photoelectric Catalysis. *Chin. J. Struct. Chem.* **2023**, *42*, 100133. https://doi.org/10.1016/j.cjsc.2023.100133.
169. Chen, L.; Miao, L.; Chen, Y.; et al. An enzyme-free photoelectrochemical glucose sensor based on coupling $BiVO_4$ with gold nanoparticles. *Mater. Sci. Semicond. Process.* **2020**, *125*, 105632. https://doi.org/10.1016/j.mssp.2020.105632.
170. Liu, F.; Zhao, J.; Liu, X.; et al. PEC-SERS Dual-Mode Detection of Foodborne Pathogens Based on Binding-Induced DNA Walker and C_3N_4/MXene-Au NPs Accelerator. *Anal. Chem.* **2023**, *95*, 14297–14307. https://doi.org/10.1021/acs.analchem.3c02529.
171. Zheng, T.; Jiang, X.; Li, N.; et al. A portable, battery-powered photoelectrochemical aptasesor for field environment monitoring of *E. coli O157:H7*. *Sens. Actuators B Chem.* **2021**, *346*, 130520. https://doi.org/10.1016/j.snb.2021.130520.
172. Wang, G.; Li, L.; Zheng, H.; et al. Bifunctional Strategy toward Constructing Perovskite/Upconversion Lab-on-Paper Photoelectrochemical Device for Sensitive Detection of Malathion. *ACS Nano* **2023**, *17*, 13418–13429. https://doi.org/10.1021/acsnano.3c01692.
173. Lin, Q.; Yu, Z.; Lu, L.; et al. Smartphone-based photoelectrochemical immunoassay of prostate-specific antigen based on Co-doped Bi_2O_2S nanosheets. *Biosens. Bioelectron.* **2023**, *230*, 115260. https://doi.org/10.1016/j.bios.2023.115260.
174. Qiu, M.; Wang, D.; Liang, W.; et al. Novel concept of the smart NIR-light–controlled drug release of black phosphorus nanostructure for cancer therapy. *Proc. Natl. Acad. Sci. USA* **2018**, *115*, 501–506. https://doi.org/10.1073/pnas.1714421115.
175. Xie, Z.; Peng, M.; Lu, R.; et al. Black phosphorus-based photothermal therapy with aCD47-mediated immune checkpoint blockade for enhanced cancer immunotherapy. *Light Sci. Appl.* **2020**, *9*, 161. https://doi.org/10.1038/s41377-020-00388-3.
176. Chen, S.; Xing, C.; Huang, D.; et al. Eradication of tumor growth by delivering novel photothermal selenium-coated tellurium nanoheterojunctions. *Sci. Adv.* **2020**, *6*, eaay6825. https://doi.org/10.1126/sciadv.aay6825.
177. Abdinejad, M.; Elmahgary, M.G.; Bolongaro, V.; et al. Solar-Driven Carbon Dioxide Capture Using a Photoelectrochemical Redox Flow System. *Acs Energy Lett.* **2025**, *10*, 2952–2959. https://doi.org/10.1021/acsenergylett.5c00452.
178. Wang, S.; Zhu, J.-H.; Zheng, Y.; et al. Target-Induced Dye-Sensitized Solar Cell Design on Photoelectrochemical Anode

for Improved Enantiomer Discrimination. *Adv. Funct. Mater.* **2025**, e23978. https://doi.org/10.1002/adfm.202523978.
179. Balog, A.; Kecsenovity, E.; Samu, G.F.; et al. Paired photoelectrochemical conversion of CO_2/H_2O and glycerol at high rate. *Nat. Catal.* **2024**, *7*, 522–535. https://doi.org/10.1038/s41929-024-01134-3.
180. Meng, X.; Zhu, C.; Wang, X.; et al. Hierarchical triphase diffusion photoelectrodes for photoelectrochemical gas/liquid flow conversion. *Nat. Commun.* **2023**, *14*, 2643. https://doi.org/10.1038/s41467-023-38138-9.
181. Stoll, T.; Zafeiropoulos, G.; Tsampas, M.N. Solar fuel production in a novel polymeric electrolyte membrane photoelectrochemical (PEM-PEC) cell with a web of titania nanotube arrays as photoanode and gaseous reactants. *Int. J. Hydrog. Energy* **2016**, *41*, 17807–17817. https://doi.org/10.1016/j.ijhydene.2016.07.230.
182. Chen, M.; Chen, R.; Zhu, X.; et al. A membrane electrode assembled photoelectrochemical cell with a solar-responsive cadmium sulfide-zinc sulfide-titanium dioxide/mesoporous silica photoanode. *J. Power Sources* **2017**, *371*, 96–105. https://doi.org/10.1016/j.jpowsour.2017.10.049.
183. Zhang, Y.; Hu, H.; Kang, W.; et al. Enhancing hydrogen evolution by photoelectrocatalysis of water splitting over a CdS flowers-loaded TiO_2 nanotube array film on the Ti foil substrate. *Ceram. Int.* **2020**, *46*, 17606–17613. https://doi.org/10.1016/j.ceramint.2020.04.062.
184. Satriyatama, A.; Zhou, S.; Toe, C.Y.; et al. Optimizing Bismuth Vanadate Photoanode for Photoelectrochemical Water Splitting Membrane Electrode Assembly Electrolyzers. *Energy Fuels* **2025**, *39*, 18649–18659. https://doi.org/10.1021/acs.energyfuels.5c03698.
185. Hong, C.Y.; Zou, W.J.; Ran, P.X.; et al. Anomalous intense coherent secondary photoemission from a perovskite oxide. *Nature* **2023**, *617*, 493–498. https://doi.org/10.1038/s41586-023-05900-4.
186. Yan, J.; Yuan, X.; Liang, Z.; et al. A Stable Ultrathin Porous Membrane based on Rigid Polymer by Phase Separation for Flow Batteries. *Trans. Tianjin Univ.* **2025**, *31*, 320–329. https://doi.org/10.1007/s12209-025-00435-3.
187. Lu, R.; Du, K.; Liu, G.; et al. Preparation and Photoelectrochemical Properties of Multilayered WS_2 Coated Titanium Dioxide Nanocomposites. *ECS Meet. Abstr.* **2020**, *MA2015-01*, 902. https://doi.org/10.1149/ma2015-01/9/902.
188. Liu, D.; Liu, J.C.; Cai, W.Z.; et al. Selective photoelectrochemical oxidation of glycerol to high value-added dihydroxyacetone. *Nat. Commun.* **2019**, *10*, 1779. https://doi.org/10.1038/s41467-019-09788-5.
189. Du, D.F.; Han, Y.M.; Liu, P.X.; et al. Simultaneous Glycolate and Hydrogen Generation Enabled by Unassisted Photocathode-Anode Cells. *Adv. Energy Mater.* **2025**, *15*, e04721. https://doi.org/10.1002/aenm.202504721.
190. Mushtaq, M.; Sathyakam, U.P. Simulation and optimization of hematite-based photoelectrochemical cells for enhanced solar-to-hydrogen conversion efficiency. *J. Power Sources* **2025**, *642*, 236806. https://doi.org/10.1016/j.jpowsour.2025.236806.
191. Gao, B.; Mu, X.W.; Feng, J.Y.; et al. Proton-Coupled Electron Transfer in Photoelectrochemical Alcohol Oxidation Enhanced by Nickel-Based Cocatalysts. *Angew. Chem. Int. Ed.* **2025**, *64*, e202413298. https://doi.org/10.1002/anie.202413298.
192. Chen, Z.; Zhu, Y.; Li, X.N.; et al. Photoelectrochemical Asymmetric Epoxidation of Alkenes with Water as an Oxygen Source in a Biphasic System. *J. Am. Chem. Soc.* **2025**, *147*, 30154–30162. https://doi.org/10.1021/jacs.5c08112.
193. Liu, Y.; Sun, J.H.; Huang, H.H.; et al. Improving CO_2 photoconversion with ionic liquid and Co single atoms. *Nat. Commun.* **2023**, *14*, 1457. https://doi.org/10.1038/s41467-023-36980-5.
194. Zong, X.; Han, J.F.; Seger, B.; et al. An Integrated Photoelectrochemical-Chemical Loop for Solar-Driven Overall Splitting of Hydrogen Sulfide. *Angew. Chem. Int. Ed.* **2014**, *53*, 4399–4403. https://doi.org/10.1002/anie.201400571.
195. Tian, Y.; Long, L.Z.; Wang, H.M.; et al. Efficient Photoelectrocatalytic Reduction of CO_2 to Selectively Produce Ethanol Using FeS_2/TiO_2 p–n Heterojunction Photoelectrodes. *ACS Appl. Mater. Interfaces* **2024**, *16*, 52299–52308. https://doi.org/10.1021/acsami.4c10453.
196. Mao, R.; Di, S.; Wang, Y.; et al. Photoelectrocatalytic degradation of Ag-cyanide complexes and synchronous recovery of metallic Ag driven by TiO_2 nanorods array photoanode combined with titanium cathode. *Chemosphere* **2020**, *242*, 125156. https://doi.org/10.1016/j.chemosphere.2019.125156.
197. Li, W.C.; Cheng, C.; Zhao, J.Q.; et al. Enhanced Azo Dye Removal through Sequential Ultrasound-Assisted-Treatment and Photocatalysis Using CdZnS. *Angew. Chem. Int. Ed.* **2025**, *64*, e202425508. https://doi.org/10.1002/anie.202425508.
198. Guo, S.H.; Su, J.; Luo, H.; et al. Boosting Photocatalytic Hydrogen Evolution Reaction by the Improved Mass Flow and Energy Flow Process Based on Ultrasound Waves. *Acs Catal.* **2023**, *13*, 296–307. https://doi.org/10.1021/acscatal.2c05365.
199. Li, J.C.; Kuang, Y.; Meng, Y.T.; et al. Electroreduction of CO_2 to formate on copper based electrocatalyst at high pressures with high energy conversion efficiency. *J. Am. Chem. Soc.* **2020**, *142*, 7276–7282. https://doi.org/10.1021/jacs.0c00122.
200. Wu, L.; Arenas, L.F.; Graves, J.E.; et al. Flow Cell Characterisation: Flow Visualisation, Pressure Drop and Mass Transport at 2D Electrodes in a Rectangular Channel. *J. Electrochem. Soc.* **2020**, *167*, 043505. https://doi.org/10.1149/1945-7111/ab7b49.
201. Peng, O.W.; Hu, Q.K.; Jin, M.T.; et al. Hydroxyl and nitrate co-upgrading to oxime via anode-cathode cascade electrolyzer. *Nat. Commun.* **2025**, *16*, 6145. https://doi.org/10.1038/s41467-025-61186-2.
202. Mu，Rui; Ma, X.; Weng, W.; et al. Simulation Study on the Effect of Spiral Flow Field Design on the Performance of PEM Electrolytic Cells. *Adv. New Renew. Enengy* **2023**, *11*, 295–302. https://doi.org/10.3969/j.issn.2095-560X.2023.04.001.

203. Zhao, R.C.; Xu, Y.Q.; Lv, Z.P.; et al. Structure Design of Electrolytic Cell: An Approach of Enhancing Mass Transfer. *J. Electrochem. Soc.* **2025**, *172*, 034512. https://doi.org/10.1149/1945-7111/adbfc7.
204. Haaring, R.; Lee, J.W.; Jeon, S.S.; et al. A Guide to the Design and Testing of a Lab-Scale Flow Cell CO_2 Electrolyzer with Gas-Diffusion Electrodes. *Chem. Mater.* **2025**, *37*, 3022−3039. https://doi.org/10.1021/acs.chemmater.4c03459.
205. Ham, C.T.; Shrestha, P.; Kober, L.; et al. The Role of Operating Temperature on Pore-Scale Gas Transport in Polymer Electrolyte Membrane Electrolyzers. *Adv. Sci.* **2025**, *12*, e07606. https://doi.org/10.1002/advs.202507606.
206. Wang, B.; Ni, M.; Zhang, S.; et al. Two-phase analytical modeling and intelligence parameter estimation of proton exchange membrane electrolyzer for hydrogen production. *Renew. Energy* **2023**, *211*, 202–213. https://doi.org/10.1016/j.renene.2023.04.090.
207. Yao, C.; Zhang, Q.J.; Lu, H.; et al. Deep Learning Guided Exploration of Transition Metal Oxide Catalysts in Acetylene Selective Hydrogenation. *J. Am. Chem. Soc.* **2026**, *148*, 790−800. https://doi.org/10.1021/jacs.5c16333.
208. Lang, F.F.; Zhang, L.L.; Li, Y.; et al. Retrieving the Stability and Practical Performance of Activation-Unstable Mesoporous Zr(IV)-MOF for Highly Efficient Self-Calibrating Acidity Sensing. *Angew. Chem. Int. Ed.* **2025**, *64*, e202422517. https://doi.org/10.1002/anie.202422517.
209. Hashemi, S.A.; Ghaffarkhah, A.; Isari, A.A.; et al. Advancing from MOFs and COFs to Functional Macroscopic Porous Constructs. *Adv. Mater.* **2025**, *37*, 2411617. https://doi.org/10.1002/adma.202411617.
210. Liang, F.; Kong, H.; Babu, D.S.; et al. Photoelectrochemical water splitting cells at elevated pressure using $BiVO_4$ and platinized III-V semiconductor photoelectrodes. *Nat. Commun.* **2025**, *16*, 11139. https://doi.org/10.1038/s41467-025-67294-3.
211. Gao, Y.F.; Sun, F.Q.; Fang, Y.J.; et al. Molecular Photoelectrodes with Enhanced Photogenerated Charge Transport for Efficient Solar Hydrogen Evolution. *J. Am. Chem. Soc.* **2025**, *147*, 7671–7681. https://doi.org/10.1021/jacs.4c17133.
212. Luo, L.; Zhu, Y.Q.; Chen, W.; et al. Photoelectrocatalytic Activation of C─H Bond in Toluene by Titanium Dioxide-Supported Subnanometric PtO_x Clusters. *Angew. Chem. Int. Ed.* **2025**, *64*, e202505544. https://doi.org/10.1002/anie.202505544.
213. Wang, X.; Zhao, S.; Guo, T.; et al. Designing Membrane Electrode Assembly for Electrochemical CO_2 Reduction: A Review. *Trans. Tianjin Univ.* **2024**, *30*, 117–129. https://doi.org/10.1007/s12209-024-00390-5.
214. Qian, W.; Zhang, H.; Chen, M.; et al. Designing Janus Photoelectrode for Efficient Photoelectrochemical VOC Mineralization at the Gas–Solid Interface. *ACS EST Eng.* **2025**, *5*, 3533−3543. https://doi.org/10.1021/acsestengg.5c00632.
215. Zhang, T.H.; Lin, S.A.; Liu, H.M.; et al. An Ionomer-Free Gapless Catalyst-Bridging Membrane Electrode Assembly for High-Performance Pure Water-Fed Anion Exchange Membrane Electrolyzer. *Adv. Mater.* **2025**, *38*, e09805. https://doi.org/10.1002/adma.202509805.
216. Chen, Y.; Kong, X.; Yang, C.S.; et al. A catalytic cycle that enables crude hydrogen separation, storage and transportation. *Nat. Energy* **2025**, *10*, 971–980. https://doi.org/10.1038/s41560-025-01806-9.
217. Ernst, M.F.; Meier, V.; Kornherr, M.; et al. Preparation and Performance Evaluation of Microporous Transport Layers for Proton Exchange Membrane (PEM) Water Electrolyzer Anodes. *J. Electrochem. Soc.* **2024**, *171*, 074511. https://doi.org/10.1149/1945-7111/ad63cf.
218. Wan, L.; Pang, M.B.; Le, J.F.; et al. Oriented intergrowth of the catalyst layer in membrane electrode assembly for alkaline water electrolysis. *Nat. Commun.* **2022**, *13*, 7956. https://doi.org/10.1038/s41467-022-35603-9.
219. Seger, B.; Kamat, P.V. Fuel Cell Geared in Reverse: Photocatalytic Hydrogen Production Using a TiO_2/Nafion/Pt Membrane Assembly with No Applied Bias. *J. Phys. Chem. C* **2009**, *113*, 18946–18952. https://doi.org/10.1021/jp907367k.
220. Kageshima, Y.; Minegishi, T.; Domen, K. Model Study for Photoelectrochemical Methylcyclohexane Production from Toluene and Water Using $SrTiO_3$ Photoanodes. *ECS Meet. Abstr.* **2020**, *MA2017-01* 1528. https://doi.org/10.1149/ma2017-01/32/1528.
221. Jin, T.; Chen, P.; Wang, J.T.; et al. Entropy-guided discovery of denary trirutile antimonates for electrocatalytic chlorine evolution. *Joule* **2025**, *9*, 102200. https://doi.org/10.1016/j.joule.2025.102200.
222. Bennett, J.A.; Orouji, N.; Khan, M.; et al. Autonomous reaction Pareto-front mapping with a self-driving catalysis laboratory. *Nat. Chem. Eng.* **2024**, *1*, 240–250. https://doi.org/10.1038/s44286-024-00033-5.
223. Gong, Z.J.; Zhang, W.; Chen, J.Y.; et al. Upcycling CO_2 into succinic acid ($C_4H_6O_4$) by cascading CO_2 electroreduction with electrocarboxylation. *Bioresour. Technol.* **2024**, *406*, 130956. https://doi.org/10.1016/j.biortech.2024.130956.
224. Yang, L.; Zhang, C.; Yu, X.; et al. Extraterrestrial artificial photosynthetic materials for in-situ resource utilization. *Natl. Sci. Rev.* **2021**, *8*, nwab104. https://doi.org/10.1093/nsr/nwab104.
225. Ross, B.; Haussener, S.; Brinkert, K. Assessment of the technological viability of photoelectrochemical devices for oxygen and fuel production on Moon and Mars. *Nat. Commun.* **2023**, *14*, 3141. https://doi.org/10.1038/s41467-023-38676-2.
226. Brinkert, K.; Richter, M.H.; Akay, Ö.; et al. Efficient solar hydrogen generation in microgravity environment. *Nat. Commun.* **2018**, *9*, 2527. https://doi.org/10.1038/s41467-018-04844-y.
227. Kölbach, M.; Rehfeld, K.; May, M.M. Efficiency gains for thermally coupled solar hydrogen production in extreme cold. *Energy Environ. Sci.* **2021**, *14*, 4410–4417. https://doi.org/10.1039/D1EE00650A.

228. Miao, R.K.; Fan, M.Y.; Wang, N.; et al. CO electrolysers with 51% energy efficiency towards C_{2+} using porous separators. *Nat. Energy* **2025**, *10*, 1197–1204. https://doi.org/10.1038/s41560-025-01846-1.